
UNIVERSITÀ DEGLI STUDI DI PADOVA

Dipartimento di Fisica e Astronomia “Galileo Galilei”

Master Degree in Astrophysics and Cosmology

Final dissertation

# Kinematics characterization of targets in the PLATO Input Catalogue

**Thesis supervisor**

Prof. Giampaolo Piotto

**Thesis co-supervisor**

Dr. Valerio Nascimbeni

**Candidate**

Gabriel Consolini

Academic Year 2023/2024

# Abstract

PLATO (PLanetary Transits and Oscillations of stars) is a mission of the European Space Agency (ESA) which will launch in 2026, with the ambitious goal of discovering a large number of Earth-like exoplanets orbiting around Sun-like stars. To achieve its objectives, PLATO will observe hundreds of thousands of FGK dwarfs and subgiants and M stars. The first observing field has been recently selected and contains about 180 000 targets.

The work which is presented in this master thesis is framed in the context of the PLATO mission and in particular in the necessary preliminary analysis of the targets, needed both for the optimization of the mission as well as for the interpretation of the mission results. In particular, in this work I performed a 6-D (positions and velocities in the Milky Way) kinematics investigation of the targets in the PLATO Input Catalogue (PIC), namely the catalogue containing the targets that will be observed. The main aim of this work is to place PIC targets in the context of the Milky Way, so that, when PLATO will start discovering exoplanets, it will be possible to study the relation between planets and the Galactic environment in which they formed. To perform such study, I cross-matched the PIC with catalogues containing the data from other surveys, such as Gaia DR3 and RAVE, in order to extract information about the positions, the proper motions and the metallicity of the targets. Analyzing these data, I was able to classify the targets in terms of the stellar components of our Galaxy: thin disk, thick disk and halo.

Furthermore, I showed and briefly discussed the stellar properties of the targets, such as radius, mass and effective temperature, in the context of each stellar component.

Finally, I cross-matched the PIC with other relevant catalogues, such as the TESS Objects of Interest catalogue, the VSX catalogue, which lists variable objects, and a recently-created Gaia-based open clusters catalogue in order to identify peculiar targets and evaluate how many and which targets belong to known open clusters.

# Acknowledgements

This work presents results from the European Space Agency (ESA) space mission Gaia. Gaia data are being processed by the Gaia Data Processing and Analysis Consortium (DPAC). Funding for the DPAC is provided by national institutions, in particular the institutions participating in the Gaia MultiLateral Agreement (MLA). The Gaia mission website is https://www.cosmos.esa.int/gaia. The Gaia archive website is https://archives.esac.esa.int/gaia. This work presents results from the ESA space mission PLATO. The PLATO payload, the PLATO Ground Segment and PLATO data processing are joint developments of ESA and the PLATO Mission Consortium (PMC). Funding for the PMC is provided at national levels, in particular by countries participating in the PLATO Multilateral Agreement. Members of the PLATO Consortium can be found at https://platomission.com/. The ESA PLATO mission website is https://www.cosmos.esa.int/plato. This research has made use of the SIMBAD database, operated at CDS, Strasbourg, France. This research has made use of the International Variable Star Index (VSX) database, operated at AAVSO, Cambridge, Massachusetts, USA.

I would like to thank Professor Giampaolo Piotto and Doctor Valerio Nascimbeni for offering me the opportunity to give my (very small) contribution to the amazing PLATO mission and for their support in the making of this thesis work. I would also like to thank the many people who have been close to me and have supported me throughout my whole life. I cannot name them all here, for they are many and this section would be longer that the main work, but they know who they are. I will, however, make an exception for two of them. Firstly, my mother Rebecca, who has always supported and pushed me along this path, even when things looked dire, and has never left my side. Secondly, my brother Lorenzo, who, even through disagreements, has made me grow as a man.

# Contents

# List of Figures

# List of Tables

# Chapter 1

# Introduction

Since the first detection of an exoplanet orbiting a Main-Sequence star in 1995 (Mayor and Queloz 1995), the field of exoplanetary astrophysics has seen an exponential growth, with more than 5 000 exoplanets already confirmed and multiple ground and space-based missions, both already active and planned, dedicated to the discovery of exoplanets. PLATO is one of such missions. It is an ESA mission, whose launch is planned for late 2026, which will provide invaluable and unprecedented information about exoplanets. Its main objective is the detection of proper Earth analogs, namely Earth-sized planets orbiting in the habitable zone around Sun-like stars. This ambitious goal will be obtained through the combination of several techniques: photometric observations of stars from space in order to detect transiting exoplanets, asteroseismic observations of stars in order to precisely derive stellar masses, radii and ages and finally radial-velocity observations from Earth to constrain the mass of the exoplanets. This means that PLATO will be able to provide the mean density and the age of the observed exoplanets, therefore providing a first characterization of their physical properties. PLATO will observe a sample of hundreds of thousands of FGK and M stars. Recently, the first field that will be observed, located in the southern ecliptic hemisphere, has been officially selected. It is clear that, before the start of the observations, it is necessary to characterize as much as possible the properties of the targets. This is the context in which this master thesis project finds its home. In particular, the work presented here aims at investigating the kinematics of the targets of the PLATO mission, in order to categorize them in terms of the stellar components of the Milky Way. Once the targets have been divided on the basis of the stellar components they belong to, each component is analyzed through the study of its metallicity distribution and other stellar properties distributions, such as mass, radius and effective temperature. Finally, the targets are cross-matched with other important catalogues to acquire relevant information, such as their variability and whether they belong to some known open cluster. This work is performed both for the already selected field, LOPS2, and a provisional field, LOPN1, which is located in the northern ecliptic hemisphere. As specified above, the

main objective of this project is the kinematic characterization of PLATO targets. This is possible thanks to the Gaia mission, another ESA mission, launched in 2013, which has allowed to measure the parallaxes (and therefore the distances) of an unprecedented number of stars, together with their positions and proper motions. This is just one of the many examples of the value that the sinergy of different space mission can provide.

This thesis is organized as follows. Chapter 1 is this introduction to the thesis. In Chapter 2 I present the PLATO mission, its observing strategy, its instruments, its scientific goals and its targets. In Chapter 3 I present the Gaia mission, its observing strategy, its instruments and its scientific goals. In Chapter 4 I provide a brief description of the stellar components of the Milky Way, namely the Galactic bulge, the Galactic disk and the Galactic halo. In Chapter 5 I show the kinematics investigation of PLATO targets, their classification in terms of the stellar component of the Galaxy that they belong to and the analysis of their metallicity distributions. In Chapter 6 I study the stellar properties of the various components. In Chapter 7 I cross-match the PLATO targets with other important catalogues in order to identify peculiar targets. Chapter 8 sums up the work performed in this thesis and provides some concluding remarks. In Appendix A I briefly discuss the two exoplanet detection methods upon which PLATO is based: the transit method and the radial velocity method. In Appendix B I present the trigonometric parallax method, which is a fundamental method to measure the distance of nearby stars and upon which the Gaia mission is based. Finally, in Appendix C I present the calculation of the uncertainties on T and V, quantities that will be later defined.

# Chapter 2

# The PLATO mission

In this chapter I describe the PLATO (PLAnetary Transit and Obscillations of stars) mission. In particular, I focus on the objectives of the mission, the instrumentation, the targets it will observe and the choice of the fields of view.

## 2.1 Overview of the mission

PLATO is the M3 mission of the the Cosmic Vision 2015-2025 program of the European Space Agency (ESA), whose launch is planned in 2026 (Rauer et al. 2024). Its main objective will be the detection of exoplanets by observing their transits in front of their stars. This technique has proven to be extremely efficient at detecting exoplanets, as proven by the CoRoT (Baglin et al. 2009), Kepler (Borucki et al. 2010) and TESS (Ricker et al. 2014) missions. The PLATO mission, however, will be different with respect to these previous missions, as it will provide a more complete picture. In particular, it will be able to provide precise planetary radii, masses and ages and therefore planetary mean densities. The main planet hunting target range will be $4 < M_V < 11$. This will allow for accurate asteroseismic studies as well as accurate planetary parameters determination. Stellar radii will be known from the measurements performed by the Gaia mission and from asteroseismic observations from PLATO itself, while stellar masses and ages will be derived from the PLATO asteroseismic studies. Exoplanets masses will be measured from the radial velocity (RV) follow-up spectroscopy. This combination of techniques will potentially constrain the planetary masses and radii to the level of 2% or even less. Stellar ages will be constrained up to 10% for solar-like stars. The targets, which are in the number of hundreds of thousands, are divided in samples and will include FGK and M stars.

PLATO will be able to provide another key improvement with respect to previous space and ground-based surveys: it will be able to consistently detect Earth-sized exoplanets with Earth-like orbits around Sun-like stars. This is the key goal of the mission.

There are also other additional goals, that will be better explored in subsection 2.12, regarding topics of planetary science as well as stellar astrophysics.

The mission is expected to last for at least 4 years, with the possibility of an extension up to 8 years in total.

### 2.1.1 Mission concept and instrument

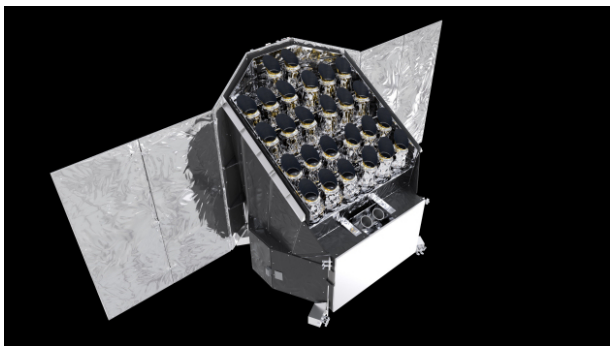

Figure 2.1: PLATO artist impression. Credits to ESA/ATG medialab.

PLATO consists of a spacecraft module and a payload module which will include the telescope and the cameras. It will be injected into a Lissajous Orbit around the L2 Lagrangian point, allowing for a nominal lifetime of 6 years, with the possibility of an extended science operation phase lasting up to 2 years. PLATO will measure a large number of terrestrial exoplanets orbiting bright stars. As a consequence, the payload module needs to provide a large field of view (FoV), so that the sparsely distributed bright stars can be observed in a single pointing, and to cover a large part of the sky during the step-and-stare mode. Furthermore, the payload module needs to provide the required photometric accuracy in order to detect Earth-sized exoplanets. Finally, it must provide a high photometric dynamic range, since the targets magnitudes can vary from 4 mag up to 16 mag. In order to achieve all these necessary requirements, a multi-telescope instrument is needed. In particular, the instrument consists of 26 telescopes: 24 so-called "normal" cameras and 2 "fast" cameras. Each telescope has a FoV of 1100 $deg^2$ and a pupil diameter of 120 mm. Each telescope has a focal plane array consisting of 4 CCDs. Normal cameras will be read-out in full frame mode with a cadence of 25 s and they will observe stars with magnitudes larger than 8 mag. They will work in a large bandpass, namely from 500 nm to 1050 nm. Fast cameras, instead, will be read-out in frame transfer mode, with a cadence of 2.5 s, and will be used to observe targets with magnitudes comprised within 4 mag and 8 mag. They will observe in particular bandpasses to perform stellar analysis. Normal cameras are divided in groups of 6. Cameras within these groups are aligned in terms of their pointing directions. The

groups are offset in their pointing directions by an angle of 9.2° with respect to the z axis of the payload. As a result, the field observed in a pointing has an area of the order of 2100 deg$^2$ (Ragazzoni et al. 2015). This strategy allows to optimize the dynamic photometric range of the instrument and to allow to observe a large number of targets with a given noise level, at the cost of having a sensitivity which varies across the field. A visualization of the pointing is presented in Fig 2.2.

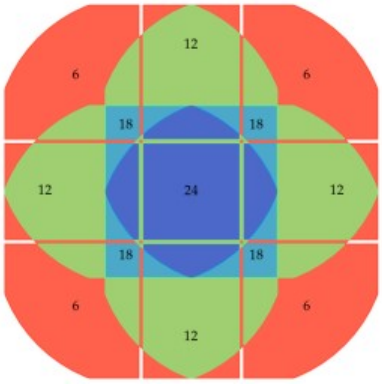


Figure 2.2: FoVs for the groups of cameras. The image is taken from Fig. 25 of Rauer et al. (2024).

Since the FoV is so large, the data volume is extremely large and therefore on-board processing is required. This processing results in light curves per star and per telescope. Light curves from individual telescopes will then be transferred to ground. A limited number of windows (with sizes of 6x6 pixels for normal cameras and 9x9 pixels for fast cameras) containing selected targets can be transferred to ground.

### 2.1.2 Observing strategy

The PLATO observing strategy consists in the combination of two approaches: long continuous pointings to detect terrestrial planets with distances from their stars up to the habitable zone and short pointings to detect planets with short periods and to study other scientific cases. In particular, the baseline observing strategy will employ Long-duration Observation Phases, consisting of continuous observations for two sky pointings, lasting between 2 and 3 years for the first pointing and 2 years for the second pointing, and Step-and-Stare Observation Phases, during which shorter observations of several sky fields will be performed for a total of 1 or 2 years. Sky fields during this phase will be observed for at least 2 and up to 5 months. This observing strategy has been envisioned in order to cover a large sky fraction and to increase the number of detected exoplanets with orbits up to the habitable zone.

To account for the telemetry limitations, the targets observed by the mission need to be pre-selected, generating the PLATO Input Catalogue (PIC). Given the importance of the topic, the selection process of the PIC needs an in-depth discussion, which is presented in Section 2.2.

A core feature of the PLATO mission is that it will provide the radius and the mass of the detected exoplanets, in order to determine their mean density. As it is well known, the mass of exoplanets can be determined using RV observations. Such observations require a large observational effort, so it is important to reduce the list of targets for such follow-up observations in order to not waste resources. This can be done following a multi-step approach. The first step is to identify false alarms. The transit detection method, despite its efficiency in detecting exoplanets, is known to suffer from a high false alarm rate. Light curves will therefore undergo several checks to guarantee a reliable probability that the signal is of planetary origin. It is also important to obtain high spatial resolution imaging of the planetary transit candidates to exclude contamination by background objects. This step is particularly important to identify smaller exoplanets, whose transits are shallower and require an increased observational effort for a RV follow-up. Once all these tests are done, RV observations can be performed. In this phase, both low-resolution and high-resolution spectrographs will be used. In particular, for the low-mass and longer orbit exoplanets (in a sense, the most interesting targets), high-precision spectrographs will be required. Since RV follow-ups are very time-consuming, it is clear that the observations of such targets will be prioritized, leaving other "less interesting" targets for future study.

The number of small-sized planets orbiting in the habitable zone of solar-like stars that PLATO is expected to detect is highly uncertain, mostly due to the poor knowledge we currently have about the occurrence rate of this typology of planets. Estimates are in the range of tens or, at most, a few hundreds (Rauer et al. 2024).

Regarding the data products, light curves, centroids, stellar and planetary parameters will be made public in a timely manner. About 2 000 light curves will remain proprietary of the PLATO team for a year.

### 2.1.3 Scientific goals

The scientific goals which will be achieved by the PLATO mission are numerous and deserve a specific discussion, which cannot be done in the context of this thesis. In this subsection we present only a part of them and in a concise fashion. For an in-depth analysis we refer to Rauer et al. (2014) and Rauer et al. (2024).

Regarding the field of planetary science, PLATO will characterize the bulk properties of exoplanets, such as the radius, the mass, the mean density and the age, in a wide range of systems. Earth-sized planets orbiting at distances of about 1 au around Sun-like stars will be of particular interest. PLATO will also investigate the orbital separation-mass function for low mass planets. It will study planetary evolution as a function of

age. It will study the co-planarity of exoplanets and their dynamical excitation. It will also study how planetary properties and frequencies correlate with stellar properties, orbital distance, disk properties and in general properties relevant for planet formation. PLATO will also study the correlation between Earth-like planets and the environment where they formed.

Another important field where PLATO is expected to give significant contributions is stellar structure and evolution, thanks to asteroseismic observations. Asteroseismology will be employed to determine the bulk properties of stars as well as their internal structure. This will allow to determine the ages of the stars and therefore the ages of the exoplanets that orbit such stars. This will also allow to improve our stellar evolution models. For Sun-like stars, PLATO will provide stellar masses with accuracy better than 10%, stellar radii with accuracy at the level of 1 or 2 % and stellar ages with accuracy at the level of 10%.

Besides these main objectives, PLATO is expected to provide precious insight into other fields of study, such as stellar activity and variability, accretion onto compact objects, various typologies of stars, structure and evolution of the Milky Way and other topics as well.

## 2.2 The PLATO Input Catalogue

Because of telemetry limitations, PLATO targets need to be pre-selected. For a fraction of those targets, imagettes will be transmitted to ground, while for the remaining targets centering and photometry will be performed on-board and then transmitted to ground. Pre-selection of targets is a fundamental process. Indeed, the properties of the targets are extremely important, as they impact the determination of the properties of the orbiting exoplanets as well as the asteroseismic modelling. They also play an important role in the habitability of the orbiting exoplanets and allow to study the frequency of exoplanets with respect to such properties. The all-sky PLATO input catalogue (asPIC) (Montalto et al. 2021) is therefore needed to:

- select the optimal PLATO observing fields;
- select FGKM dwarf and subgiant stars that satisfy the magnitude and the signal-to-noise constraints defined in the PLATO stellar samples requirements;
- estimate basic stellar parameters for the targets;
- identify known variable stars, known planets, binaries, members of multiple systems, active stars with bitmasks, and summarize the information available from existing catalogues;

- supply a list of all target contaminants up to a specific angular distance from the target and up to a limiting magnitude, for the targets in the fields to be observed;
- guide the organization and optimization of ground-based follow-up strategies.

The catalogue includes 2 675 539 stars, of which 2 378 177 are FGK dwarfs and subgiants and 297 362 are M dwarfs. The median distance of the FGK stars is 428 pc and that for M dwarfs is 146 pc.

### 2.2.1 Stellar samples

PLATO stellar samples consists of four samples called P1, P2, P4 and P5 which will be observed with the broad bandpass telescopes and one additional colour sample which will be observed in two broad blue and red spectral bands (Corso et al. 2018, Montalto et al. 2021). The specifics of each sample are (Montalto et al. 2021):

- P1: at least 15 000 (goal is 20 000) dwarfs and subgiants with spectral type between F5 and K7, $V \leqslant 11$, photometric accuracy better than 50 ppm in 1 hour and such that the number of bright targets ($V \leqslant 10.5$) is maximized;
- P2: at least 10 000 dwarfs and subgiants with spectral type between F5 and K7, $V \leqslant 8.5$ and photometric accuracy better than 50 ppm in 1 hour;
- P4: at least 5 000 M dwarfs with $V \leqslant 16$;
- P5: at least 245 000 dwarfs and subgiants with spectral type from F5 to late K with $V \leqslant 13$;
- colour sample: 300 stars from anywhere in the Hertzsprung-Russell diagram, observed in two separate colour broad-bands with a cadence of 2.5 s in order to obtain colour information and imagettes.

### 2.2.2 Selection criteria

The selection of the targets was made using the reddening-corrected absolute Color-Magnitude Diagrams (CMD). Theoretical models based on Galactic simulations were used to locate the targets in the CMD. On the same CMD stars satisfying the scientific requirements were represented. Using both the theoretical and the empirical distributions of stars on the CMD, an analytical selection region was defined and assessed in terms of its completeness and contamination. As a final step, it was demonstrated that such selection did not present any metalicity bias with respect to a local sample of stars. The selection criteria can be summarized as follows (Montalto et al. 2021):

**M sample**

For the M sample:

- $(G_{BP} - G_{RP})_0 \geqslant 1.84$;
- $M_{G,0} > 2.334(G_{BP} - G_{RP})_0 + 2.259$;
- distance $< 600$ pc;
- $V \leqslant 16$.

**FGK sample**

For the FGK sample:

- $0.56 \leqslant (G_{BP} - G_{RP})_0 < 1.84$;
- $M_{G,0} \leqslant 4.1(G_{BP} - G_{RP})_0 + 5.0$;
- $M_{G,0} \geqslant 4.1(G_{BP} - G_{RP})_0 - 2.2$;
- $V \leqslant 13$.

### 2.2.3 Reddening and absorption correction

As it is widely known, interstellar matter, due to its absorption capabilities, is responsible for the so-called reddening, namely the fact that astronomical objects appear redder and fainter than they really are. PLATO samples are magnitude-limited. As a consequence F-type stars, which are intrinsically more luminous than late-type stars, are, on average, located at larger distances than GKM stars and therefore are more affected by reddening. It follows that the assessment of the reddening, when selecting the targets of the mission, is of crucial importance. In order to correct for interstellar absorption, it is necessary to use reddening maps. In this case, it was decided to use the reddening map presented in Lallement et al. (2018), because of its accurate description of the local interstellar medium and its overall spatial coverage which allowed to determine the reddening for a large fraction of PIC stars in a homogeneous way.

### 2.2.4 Stellar parameters

For an in-depth discussion of the algorithms used to determine the effective temperature, the radius and the mass of the targets we refer to Section 5 of Montalto et al. (2021). Here I simply show the distributions of such parameters (Fig 2.3, Fig. 15 of the same paper).

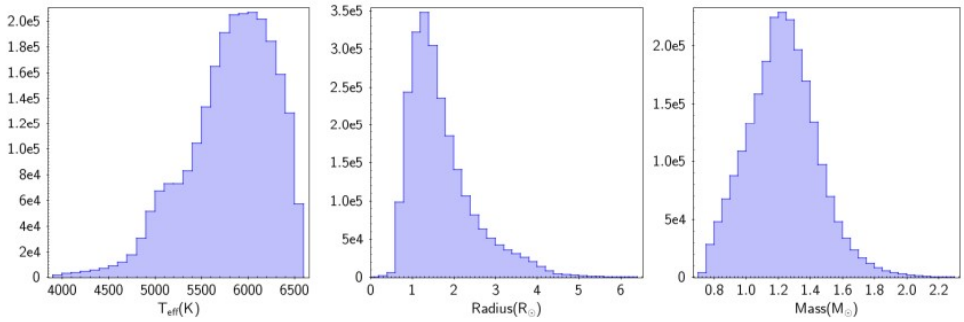


Figure 2.3: Effective temperature, radius and mass distributions of asPIC targets (from Montalto et al. 2021)

## 2.3 PLATO field selection

PLATO will likely employ a two-staged observing strategy, where two pointings will be monitored during the Long-duration Observation Phase (LOP). Each pointing will last at least one year and can be complemented by a Step-and stare Observation Phase (SOP), consisting of shorter pointings. At the moment, only the LOP field in the southern ecliptic hemisphere (LOPS2) has been conclusively defined: this will allow me to describe its properties in detail.

### 2.3.1 Field selection process

Formal requirements for the mission which have an important impact on the field selection process are (Nascimbeni et al. 2022):

- geometrical constraints: to allow for a proper orientation of the spacecraft throughout the year, the center of the LOP fields has to lie within the two caps defined by having an ecliptic longitude such that $|\beta| > 69.671°$ (Nascimbeni et al., in prep.). This requirement is needed only for the centers of the fields, meaning that the outer parts of such fields can expand beyond that threshold;

- target counts: the number of observed targets included in the PLATO stellar samples has to be larger than a defined threshold for all the samples. P1, which is considered the most important stellar sample, must contain, considering both LOP fields, at least 15 000 F5-K7 dwarfs and subgiants brighter than V=11 to be observed with a photometric precision better than 50 ppm in one hour.

In addition to formal requirements, there are also criteria of practical and scientific nature. These are useful to choose among fields which satisfy the formal requirements, in order to choose the fields which can maximize the scientific output and, at the same

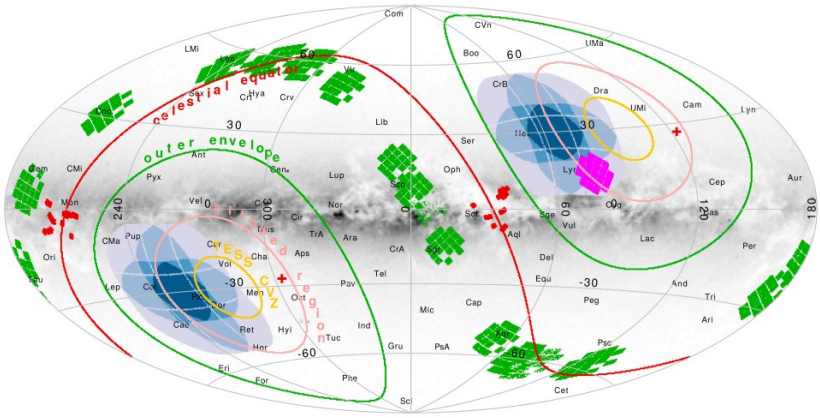


Figure 2.4: All-sky Aitoff projection in Galactic coordinates to visualize the geometrical constraints on the field selection. The pink circles identify the allowed regions for the center of the LOP fields. The fields observed by other missions are also shown, such as CoRoT (red), Kepler (magenta), K2 (green) and the TESS continuous viewing zone (yellow). The image is taken from Nascimbeni et al. (2022).

time, minimize the follow-up effort. The most important ones are (Nascimbeni et al. 2022):

- stellar contamination: a field closer to the Galactic plane will result in an increased number of stellar counts and, at the same time, it will increase the density and the flux of contaminants, resulting in a larger photometric noise and a higher false-alarm probability;
- follow-up resources: the location of the fields has an important implication in terms of the availability of ground resources for the necessary RV follow-up. The fraction of false-positives and the astrophysical parameters of the targets also have an effect on the follow-up process;
- special targets of interest: it is reasonable to verify whether known targets of interest can be observed during the pointing;
- synergy with other missions: it is possible that additional science may emerge by observing fields already observed by other missions. This is not possible for the K2 and CoRoT fields, because of the geometrical constraints, but is feasible for the Kepler field and the TESS continuous viewing zone. Furthermore, the James Webb Space Telescope (JWST) will be able to observe the vast majority of the LOP targets.

Another aspect that has to be taken into account is that the PLATO attitude is not defined entirely by the pointing direction, but it depends also on the rotation angle around the Z axis of the payload module. Different rotation angles result in different observed targets. Also, while some selection parameters depend weakly on the rotation angle, others are strongly dependent. However, in Nascimbeni et al. (in prep.), it is demonstrated that the rotation angle does not have a significant effect on the planet yield for PLATO, so it is reasonable to keep it to 0°.

To select the fields, a grid-based approach based on a prioritization metric has been used. The details can be found in Sections 4 and 5 of Nascimbeni et al. (2022).

We start by presenting the provisional field LOPN1, located in the northern ecliptic hemisphere. Successively, we present in much more detail the already selected LOPS2, located in the southern ecliptic hemisphere.

### LOPN1

LOPN1 is located at galactic longitude $l \approx 81.6°$ and galactic latitude $b \approx 24.6°$. Some very bright stars fall into this field, such as Vega (or $\alpha$ *Lyr*) and Deneb (or $\alpha$ *Cyg*). That some very bright stars are contained in the fields is unavoidable, given their extension. LOPN1 contains also some already known exoplanets, mostly (but not only) from the Kepler mission, since the field of the latter is contained within LOPN1. LOPN1 is dominated by stars larger than the Sun, with the median radius being 1.67 $R_\odot$. This is a general feature associated to any magnitude-limited sample in the dynamic range of PLATO and is not due to the field selection process. A significant number of open clusters (OCs) falls, at least partially, within LOPN1. It has been estimated that 6 of these clusters would be such that a hypothetical solar twin would be within the magnitude limit and not too young, so that stellar activity would not be a limiting factor. LOPN1 also contains 4 globular clusters (GCs). Furthermore, LOPN1 contains 45 detached eclipsing binaries (DEBs), 12 of which could meet the requirements to be included in the stellar samples. As mentioned before, LOPN1 overlaps with the fields of previous mission, such as the Kepler field and the north TESS continuous viewing zone: as a matter of fact, about 60 % of LOPN1 targets have already TESS short-cadence data.

### LOPS2

LOPS2 is centered at Galactic latitude $b \approx -24.6°$ and Galactic longitude $l \approx 255.9°$. It contains more than 90% of the TESS continuous viewing zone, mostly in regions observed with 6 cameras and 12 cameras.

Regarding the targets, LOPS2 contains:

- 8 235 P1 targets (FGK dwarfs and subgiants with $V < 11$ to be observed with a photometric precision better than 50 ppm);

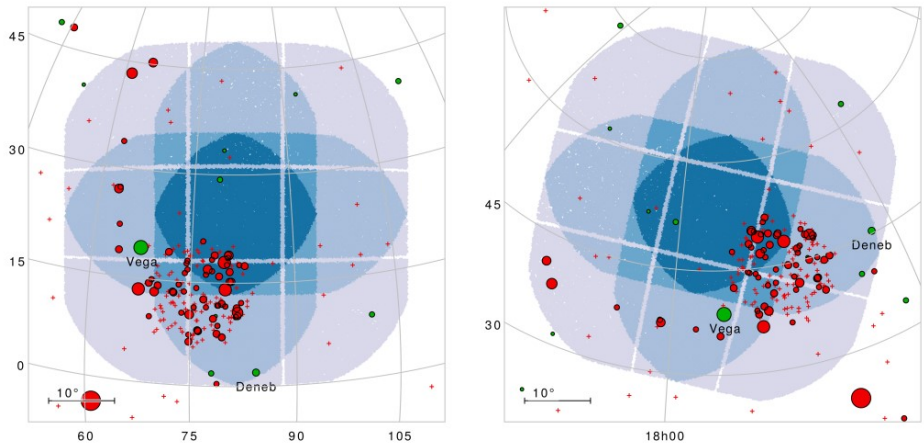


Figure 2.5: LOPN1 in Galactic (left) and equatorial (right) coordinates. Green circles indicate stars brighter than V=3. Crosses indicate already known exoplanets. Exoplanets with more than 50 references are identified by red circles, whose areas are proportional to the number of references. The image is taken from Nascimbeni et al. (2022).

- 699 P2 targets (FGK dwarfs and subgiants with $V < 8.5$ to be observed with a photometric precision better than 50 ppm):
- 12 415 P4 targets (M dwarfs with $V < 16$);
- 167 149 P5 targets (FGK dwarfs and subgiants with $V < 13$).

Computing the samples as disjoint sets, the total number of targets is 179 564. As expected, G and K dwarfs are, on average, closer to us with respect to F stars and subgiants. Identifying bright stars that fall in the field is fundamental, since they can produce photometric artifacts that may contaminate fainter targets in their vicinity. Nascimbeni et al. (in prep.) used the Yale Bright Star Catalogue (YBSC) to identify star brighter than $V \approx 6.5$. They found 712 of such stars, of which only 47 brighter than V = 4, the limit beyond which stars will be heavily saturated on the normal cameras. With the exception of 3 stars, all the 12 very bright stars ($V < 3$) are located close to the Galactic plane. In any case, because of their spectral properties, they are not suitable for any of the stellar samples of PLATO. The brightest star in LOPS2 belonging to the PIC is $\zeta$ Dor A (or HD 33262) with V = 4.68, a F7V star in a very wide binary system (Dodson-Robinson et al. 2011). The brightest single solar twin in the PIC is HD 59967 (V = 6.66), a young G2V star (Lorenzo-Oliveira et al. 2018). 92 confirmed transiting exoplanets, belonging to 71 planetary systems, are contained within LOPS2 (Nascimbeni et al., in prep.). The vast majority of them are Jupiter or Neptune-like planets, but 16 are of rocky nature. Regarding non-transiting exoplanets, LOPS2 contains 73 of them in 50 planetary systems (Nascimbeni et al., in prep.). In terms of open clusters within LOPS2, 367 of them

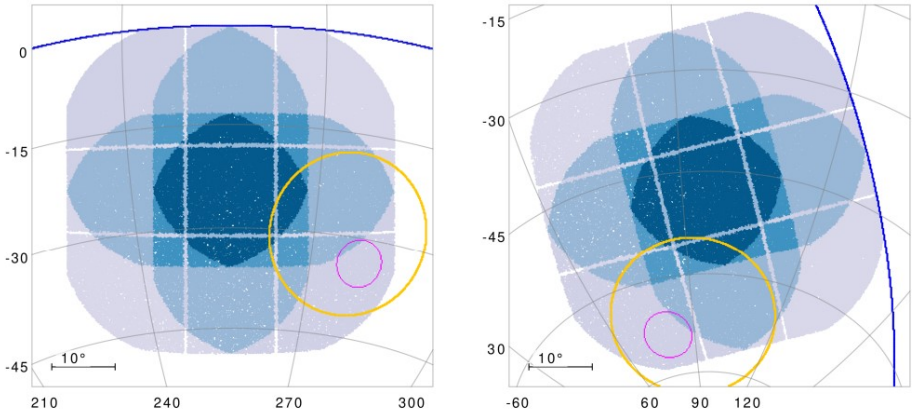


Figure 2.6: LOPS2 in Galactic (left) and equatorial (right) coordinates. The yellow circle represents the TESS continuous viewing zone, while the magenta circle represents the Large Magellanic Cloud. The image is taken from Nascimbeni et al. (in prep.).

are of interest for PLATO. This results, taking into account the scientific requirements for PLATO, in 3 506 targets of interest with spectral type later than F5V. All these clusters are very young, with ages between 15 Myr and 150 Myr (Nascimbeni et al., in prep.). When considering variable stars, it turns out that, by applying the magnitude requirement $V < 15$, LOPS2 contains 31 211 and 15 932 variable stars (Nascimbeni et al., in prep.). These numbers come from the cross-matching with the latest versions of the VSX catalogue (Watson, Henden, and Price 2006) and the Gavras et al. (2023) catalogue.

# Chapter 3

# The Gaia mission

In this chapter I describe the Gaia mission, explaining its observing strategy, its main instruments and its scientific goals.

## 3.1 Overview of the mission

Gaia is a space-based astrometric ESA mission, launched in 2013 to orbit at the L2 Lagrangian point, whose main objective is the kinematic characterization of stars (three-dimensional spatial and three-dimensional velocity distributions) in order to determine their properties, such as their effective temperature and their surface gravity, and to map and study the structure, the formation and the evolution of the Milky Way. To achieve its goals, Gaia needs to sample down to a magnitude, in the Gaia band, of at least 20. Considering such magnitude limit, it is expected that Gaia will sample 1 000 millions stars, retrieving their three-dimensional spatial structure and their three-dimensional space motions. Gaia provides us with absolute parallaxes and transverse kinematics. For a subset of the sample, this is complemented by radial velocity and photometric information. Regarding the data policy, the Gaia collaboration, after the processing, calibration and validation, makes the data available without limitations (Gaia Collaboration et al. 2016). So far, there have been three major data releases.

### 3.1.1 Mission concept and instrument

The measurement principle of Gaia is based on the global-astrometry principle adopted by the previous HIPPARCOS mission (Esa, 1989). It is based on the principle of scanning space astrometry, which consists in a slowly spinning satellite which measures the crossing times of targets transiting the focal plane. The observation times represent the one-dimensional along-scan stellar position relative to the instrument axes. Gaia is equipped with two FoVs, separated by a constant, large angle on the sky along the

scanning circle. The two viewing directions map the images onto a common focal plane such that the observation times can be converted into small-scale angular separations between stars inside each field of view and large-scale separations between objects in the two fields of view. These measurements are therefore purely differential. It is however possible to retrieve absolute parallaxes because the relative parallactic displacements can be measured between stars that are separated on the sky by a large angle and so have a substantially different parallax factor.

Gaia is equipped with two identical, three-mirror anastigmatic telescopes, with apertures of 1.45 m x 0.50 m pointing in directions separated by an angle of 106.5°. The focal plane contains 106 CCDs arranged in a mosaic of 7 across-scan rows and 17 along-scan strips, with a total of 938 million pixels. The CCDs are divided into three types: broadband CCDs (centered on 650 nm), blue-enhanced CCDs (centered on 360 nm) and red-enhanced CCDs (centered on 750 nm) (Gaia Collaboration et al. 2016).

Let me now briefly discuss the three instruments aboard Gaia.

### Astrometric instrument

The astrometric instrument is composed of the two telescopes, a dedicated area of 7 + 7 CCDs in the focal plane devoted to the sky mappers of the preceding and following telescopes and a dedicated area of 62 CCDs in the focal plane where the two fields of view are combined onto the astrometric field. It observes in the so-called G (for Gaia) band, namely an unfiltered white light band comprised between 330 nm and 1050 nm. Gaia performs an unbiased, flux-limited survey of the scale, mainly because an all-sky input catalogue at the resolution of Gaia that is complete down to 20th mag does not exist. Consequently, Gaia has been equipped with the Sky Mapper to perform autonomous on-board object detection. This instrument can manage object densities up to 1 050 000 objects $\mathrm{deg}^{-2}$. Once this limit is surpassed, only the brightest stars are observed. The instrument is able to provide astrometric data with precision at the level of the $\mu$as (Gaia Collaboration et al. 2016).

### Photometric instrument

The photometric instrument measures the spectral energy distribution (SED) of all detected objects at the same angular resolution and at the same epoch as the astrometric observations. This is performed in order to achieve two major goals:

- to provide astrophysical classification and astrophysical characterization (effective temperatures, surface gravities, metallicities...) for all objects;
- to enable chromatic corrections of the astrometric centroid data induced by optical aberrations of the telescope.

This instrument is highly integrated with the astrometric instrument, using the same telescopes, the same focal plane and the same sky mapper function for object detection. The photometry function is possible by using two fused-silica prisms dispersing light entering the FoVs. This results in two photometers: the blue photometer (BP) works in the wavelength range 330-680 nm, while the red photometer (RP) operates in the wavelength range 640-1050 nm. This instrument can manage object densities up to 750 000 objects $\mathrm{deg}^{-2}$. Above this limit, only the brightest stars are observed. It must be noted that the data quality is already affected at even lower densities because of the contamination from the point spread function wings of nearby sources falling outside the window and by blending with sources falling inside the window. If we consider a FGKM star with G = 15 and less than two magnitudes extinction, the effective temperature can be determined to levels between 75 K and 250 K, the extinction can be determined to levels between 0.06 mag and 0.15 mag, the surface gravity can be determined to levels between 0.2 dex and 0.5 dex and the metallicity can be determined to levels between 0.1 dex and 0.3 dex (Gaia Collaboration et al. 2016).

**Spectroscopic instrument**

The spectroscopic instrument or radial-velocity spectrometer (RVS) collects the spectra of the brighter end of the Gaia sample in order to achieve four goals:

- radial velocity measurements using cross-correlation for stars brighter than $G_{RVS} \approx 16$. These measurements are needed for the study of Galactic populations and to derive good astrometry of nearby, fast-moving sources showing perspective acceleration;
- coarse stellar parametrization for stars brighter than $G_{RVS} \approx 14.5$;
- astrophysical information (interstellar reddening, atmospheric parameters, rotational velocities) for stars brighter than $G_{RVS} \approx 12.5$;
- individual element abundances for some specific elements for stars brighter than $G_{RVS} \approx 11$.

$G_{RVS}$ is the integrated, instrumental magnitude in the spectroscopic bandpass. The spectroscopic instrument is highly integrated with the astrometric instrument, using the same telescopes, the same focal plane and the same sky mapper function for object detection. The selection of an object for RVS is based on an on-board estimate of $G_{RVS}$, which is generally derived from the RP spectrum collected just before the object enters RVS. By using a multilayer-interference bandpass-filter, the wavelength range of RVS is limited between 845 nm and 872 nm. This choice has been performed to cover the Ca II triplet, the hydrogen Paschen series and a diffuse interstellar band (at 862 nm) used

to trace out interstellar reddening. This instrument can manage object densities up to 35 000 objects $\mathrm{deg}^{-2}$. Above that limit, only the brightest stars are observed. Similarly to what happens with the photometric instrument, the data quality is already lowered at densities below that limit because of contamination and blending with nearby sources. The instrument is able to determine radial velocities with accuracies at the level of a few 100 $\mathrm{m\,s}^{-1}$ (Gaia Collaboration et al. 2016).

### 3.1.2 Scientific goals

Thanks to its unique capabilities, Gaia can provide insight into many different fields. I refer to Perryman et al. (2001) and Gaia Collaboration et al. (2016) for the detailed description of the science cases of the mission. I now present the scientific goals of Gaia in a concise manner:

- structure, dynamics and evolution of the Milky Way: the main aim of Gaia is the study of the dynamics, structure and evolution of the Galaxy through the analysis of the distribution and kinematics of the luminous and dark mass in the Galaxy as well as through the study of the physical properties of the constituents stars;
- star formation history of the Milky Way: Gaia distances allow to derive absolute luminosities for stars which, if combined with metallicities, can be used to determine the age of such stars with great accuracy. This knowledge is useful to better understand the star formation histories of the stellar populations contained within our Galaxy;
- stellar physics and evolution: the ability of Gaia to provide accurate distances, using the parallax method, is proving and will prove paramount in the study of stellar astrophysics, particularly when it comes to stellar formation, evolution and modelling, the latter both for individual stars as well as for stellar populations;
- stellar variability and distance scale: Gaia is a valuable instrument to study the variable sky because of its sampling and scanning law. It is estimated that it will provide tens of millions of new variables;
- binaries and multiple stars: the astrometric, photometric and spectroscopic measurements performed by Gaia will improve our understanding of binary and multiple systems;
- exoplanets: thanks to its astrometric capabilities, Gaia will probe a poorly explored area in the parameter space of exoplanetary systems: it will provide an unbiased volume-limited sample of Jupiter-mass exoplanets in distant orbits around their host stars. The astrometric detection technique also allows to measure the actual masses of these planets;

- Solar System: Gaia is able to detect asteroids. It will provide a census of orbital parameters and taxonomy of these objects in a single, homogeneous photometric system;

- Local Group: Gaia, with its spatial resolution, is able to resolve and observe the brightest individual stars in the Local Group. In the Andromeda Galaxy and in the Magellanic Clouds, it can observe thousands and even millions of stars. Gaia will study the interaction between the Magellanic Clouds and between such galaxies and the Milky Way. It will also investigate the internal stellar motions within dwarf galaxies;

- unresolved galaxies, quasars and the reference frame: Gaia will provide a homogeneous, magnitude-limited sample of unresolved galaxies. Quasars can be used in comparisons of optical and radio reference frames. This will allow to study the coincidence of quasar positions across different wavelengths;

- fundamental physics: Gaia can be used to perform tests of fundamental physics, in particular to study relativistic effects.

# Chapter 4

# Stellar components of the Galaxy

In this chapter I explore some basic concepts of Galactic astronomy, particularly concerning the stellar components of the Milky Way. The Milky Way is composed of three main stellar components, namely the bulge, the disk and the halo, each characterized by its own properties, such as kinematics, metallicity, stellar density, age and others. I aim to illustrate the fundamental properties of these three stellar components, which are crucial to understand the work presented in this thesis. This chapter is largely inspired by the famous Galactic Astronomy of Binney and Merrifield (1998).

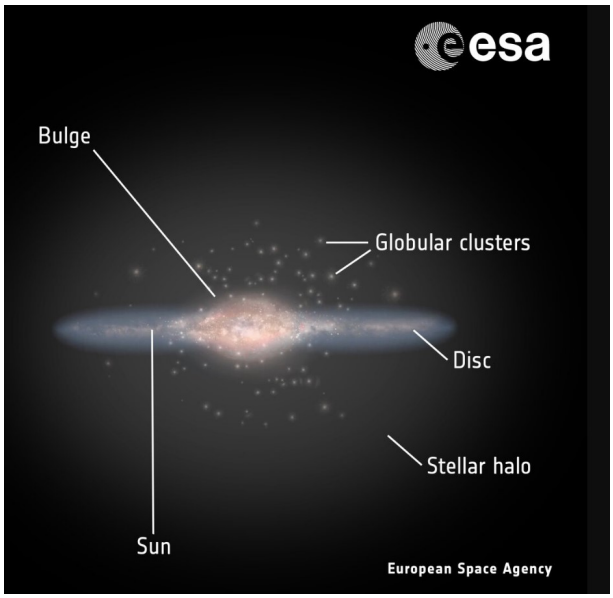


Figure 4.1: Schematic depiction of the main stellar components of the Milky Way. Credits to ESA/ATG medialab.

## 4.1 The Galactic bulge

The Galactic bulge is the central structure of the Milky Way. It is peanut-shaped, with one side larger than the other, it has a very dense central cluster of stars, it has a central bar and it extends for about 3-4 kpc from the center of the Galaxy. It has a stellar mass at the level of $20 \times 10^9$ $M_\odot$ and a luminosity at the level of $5 \times 10^9$ $L_\odot$. It hosts a super-massive black hole, Sagittarius A*, whose mass is estimated at about $4 \times 10^6$ $M_\odot$. Its stellar population is old (10-12 Gyr), but not as metal-poor as the Galactic halo. It is more flattened than the halo and its stars have larger random motions and follow a general direction of rotation with a rotation speed of the order of 100 $\mathrm{km\,s^{-1}}$. It is not of particular interest for our work, since bulge stars are constrained in the inner regions of the Galaxy. The long distance and the reddening of bulge stars is such that FGK stars of this component are too faint to be included in the P1, P2 and P5 samples.

## 4.2 The Galactic disk

The disk is a key component of the Milky Way, containing most of its baryonic matter, in the form of stars and gas. It has a radius of about 15 kpc. The Sun, which is located at about 8 kpc from the Galactic Center, belongs to the disk. The stars of the disk orbit around the Galactic center with velocities at the level of 200 $\mathrm{km\,s^{-1}}$, following almost circular orbits. The radial stellar density profile for the disk follows an exponential law, with the number of stars falling down when moving outwards from the Galactic center. The gas and dust components of the disk lie on a very thin layer whose width is of the order of 100 pc. The mass in the form of stars contained in the disk is about $60 \times 10^9$ $M_\odot$ and the luminosity of the disk is at the level of $15 - 20 \times 10^9$ $L_\odot$. The disk is home to several kinds of stellar populations, with a great variety in terms of age and chemical properties.

### 4.2.1 The thick disk and the thin disk

For stars with absolute magnitudes $M_V$ in the range 4-5, the stellar density profile as a function of the distance from the Galactic plane, $\nu(z)$, is described by the sum of two exponentials, one having a scale height $z_0 = 300$ pc, the other having a scale height $z_0 = 1350$ pc. This is true also for less luminous stars, although the evidence for a second exponential with a scale height of $z_0 = 1350$ pc is much weaker, because the density profile for these stars cannot be probed far from the Galactic plane. Stars more luminous than $M_V \approx 3$, instead, require an exponential describing the density close to the plane with a scale height much smaller than 300 pc. Furthermore, it is not clear whether their density profile also requires a second exponential with a large scale height (Gilmore and Reid 1983).

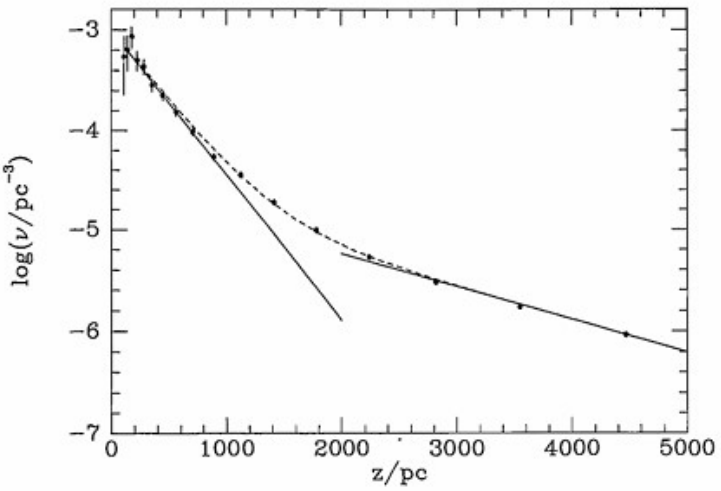


Figure 4.2: Vertical density profile for MS stars with absolute magnitudes between 4 and 5. Since this is a log-linear plot, the two exponentials which describe the profile appear as lines. The left one has a scale height $z_0 = 300$ pc, while the right one has a scale height $z_0 = 1350$ pc. The image is taken from Binney and Merrifield (1998) and originally appeared in Gilmore and Reid (1983).

The nature of the density profile can be explained in two ways. The first one is to assume that the Milky Way possesses a single disk whose vertical density profile is simply not exponential. The second one is to assume that the Milky Way possesses two disks, the thin disk and the thick disk. Both disks would follow an exponential vertical density profile, with the thin disk dominating at low z and the thick disk dominating at large z. Now, there is no known physical reason for which the disk should follow an exponential vertical density profile, so the hypothetical double nature of the disk has to be demonstrated by showing that they are made of different kinds of stars. One possible division between the two disks is made by assuming that thick disk stars are older than 10 Gyr and are more metal-poor than $[Fe/H]$ = -0.4. As a consequence, the vast majority of the remaining stars are younger than 10 Gyr and more metal-rich than $[Fe/H] = -0.4$. These stars therefore form the thin disk. One interesting feature is that stars with $[Fe/H] > -0.4$ usually have $[Mg/Fe] < 0.2$, while most of the more metal-poor stars have significantly larger over-abundances of the $\alpha$-element Mg. This hints at the fact that type Ia supernovae gave a much smaller contribution in terms of iron-peak elements to thick disk stars than they gave to thin disk stars. When analyzing the kinematics of the stars within the two disks, it appears that thick disk stars have larger characteristic velocities. Whether the Galactic disk is truly composed of two disks or not is still an open and fiercely debated question.

## 4.3 The Galactic halo

The Galactic halo is a spherical structure made of globular clusters and field stars orbiting the Milky Way far out of the Galactic disk. It reaches out to 150 kpc and its stellar density profile follows a law of the type $\rho(r) \sim r^{-3.5}$. It has a luminosity of about $10^9$ $L_\odot$ and a baryonic mass of the order of $10^9$ $M_\odot$. In terms of their chemical properties, halo stars typically have low and very low metallicities.

### 4.3.1 The globular cluster system

The globular clusters of the Milky Way can be divided in two groups: disk globular clusters, with metallicity $[Fe/H] > -0.8$, and halo globular clusters, with metallicity $[Fe/H] < -0.8$. The metallicity of disk globular clusters strongly peaks at $[Fe/H] = -0.5$, while the metallicity of halo globular clusters is much wider and reaches down to $[Fe/H] = -2.6$. Another key difference between the two groups regards their kinematics: the halo group of clusters is dominated by random motions, while the disk group of clusters is flattened, because it rotates rapidly. To give some numbers, according to the analysis of Armandroff (1989), halo clusters have an average azimuthal velocity, relative to the Local Standard of Rest, of $< v_\phi > = -177$ km s$^{-1}$, while disk clusters have an average azimuthal velocity, relative to the Local Standard of Rest, of $< v_\phi > = -27$ km s$^{-1}$. The two groups seem to have a common luminosity function. There is no statistically significant evidence for a correlation of luminosity with the Galactocentric distance or the distance from the Galactic plane.

### 4.3.2 Field halo stars

Some field stars are observed to be extremely metal-poor. This feature opens up two very interesting possibilities. Firstly, they are much closer than halo globular clusters stars, therefore they can be studied in much greater detail. Secondly, they must have formed outside of the Milky Way or when the interstellar medium of the Milky Way was not significantly polluted with metals, therefore they carry information about the origin of our Galaxy. In the solar neighborhood, the space density of very metal-poor stars is at least two orders of magnitude smaller than that of metal-rich stars, so effective strategies must be developed in order to observe such very metal-poor stars. One way is to look for RR Lyrae stars that have periods in the range defined by RR Lyrae stars in the halo globular clusters. These stars have the same metallicity distribution of halo clusters and can be identified from their characteristic variability. RR Lyrae stars, however, make up only a fraction of Horizontal Branch (HB) stars, so they cannot be used to safely infer the number of halo stars at a given location. As a consequence, it is necessary to look also for blue HB stars, since the ratio between the number of blue HB stars and the number of RR Lyrae stars can be used to reasonably predict the number of red HB stars.

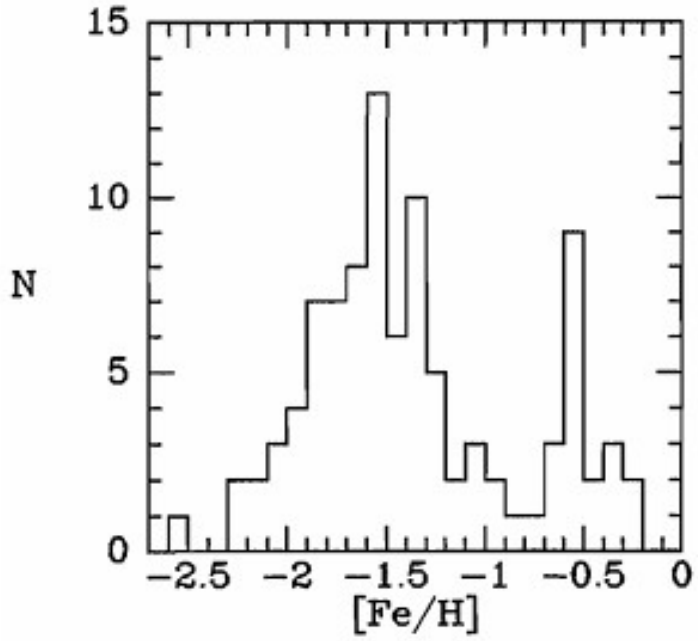


Figure 4.3: Metallicity distribution for 96 globular clusters. On the left we can see the halo globular clusters, characterized by a larger spread in metallicity and lower metallicities. On the right we can see the disk globular clusters, with their higher metallicities strongly peaked at $[Fe/H] = -0.5$. The image is taken from Binney and Merrifield (1998) and originally appeared in Armandroff (1989).

Finally, the total number of HB stars is tightly coupled to the density of all types of stars in an old population. By performing this technique, it appears that the local density of halo stars is rather small, so many studies of the halo are based on relatively distant stars. For these stars, very often only radial velocities are available. It is found that the average azimuthal velocity of halo stars is $< v_{phi} > = -185\ \mathrm{km\,s^{-1}}$ and the dispersion velocities on the three cylindrical axes are $\sigma_R = 135\ \mathrm{km\,s^{-1}}$, $\sigma_{phi} = 105\ \mathrm{km\,s^{-1}}$ and $\sigma_z = 90\ \mathrm{km\,s^{-1}}$.

An effective kinematic selection strategy to identify possible field halo stars for a successive spectroscopic investigation is to select targets which have large proper motions. Halo stars have large heliocentric velocities because they have orbits which differ greatly from the Sun's orbit. This results in them having large proper motions out to a greater distance in comparison to disk stars.

When it comes to their metallicity, field halo stars reach metallicities even lower than those of the halo globular clusters stars.

### 4.3.3 Gaia-Enceladus

I briefly illustrate the recent discovery of the Gaia-Enceladus structure (Helmi et al. 2018). It was recently found, using the data from the second Gaia Data Release (DR2), that a significant fraction of the halo stars close to the Sun belongs to a single large kinematic structure characterized by a slightly retrograde mean motion and that dominates the blue sequence in the Hertzsprung-Russell diagram revealed by the Gaia data. The most likely origin for this structure in a merging event with an external galaxy. A further confirmation for this hypothesis comes from the chemical properties of the stars, which are depleted in $\alpha$-elements. In terms of the metallicity $[Fe/H]$, they show a large spread, suggesting that they did not form in a single burst in a low mass system. The stellar mass of the progenitor system is estimated at $\sim 6 \times 10^8$ $M_\odot$, comparable to the stellar mass of the Small Magellanic Cloud. This separate galaxy has been given the name of Gaia-Enceladus. The merging event took place between 8 and 11 Gyr ago.

# Chapter 5

# Kinematics and metallicity characterization of PIC targets

In this chapter I analyze the kinematic properties of the PIC targets, sorting them out in terms of the Galactic stellar component that they belong to. Successively, I study their metallicity, in order to validate the results of the kinematic analysis.

## 5.1 Galactic coordinates

### 5.1.1 Galactic coordinates definition

In the context of this thesis I work in so-called Galactic coordinates. In this spherical celestial coordinate system the Sun is placed at its center, the Galactic Equator is the great circle that most closely approximates the plane of the Milky Way, which happens to be 82.87° inclined with respect to the celestial equator, and the north pole is located, in equatorial coordinates, at $(\alpha_{GP}, \delta_{GP}) = (192.85948, 27.12825)$. In this system, the position of a celestial object is specified in terms of the Galactic latitude $b$ and the Galactic longitude $l$. The Galactic latitude is defined as the angle from the Galactic equator to the star along the great circle through the star and the Galactic poles. This means that the north Galactic Pole is located at $b$ = +90° and the south Galactic Pole is located at $b$ = -90°. The Galactic longitude is the angle measured with respect to the direction of the Galactic Center. This results in the direction of the Galactic Center being described by $b$ = 0° and $l$ = 0°. It is possible to convert from equatorial coordinates to Galactic coordinates using the following relations:

$$\begin{cases} \sin(b) = \sin(\delta_{GP})\sin(\delta) + \cos(\delta_{GP})\cos(\delta)\cos(\alpha - \alpha_{GP}) \\ \cos(b)\sin(l_{CP} - l) = \cos(\delta)\sin(\alpha - \alpha_{GP}) \\ \cos(b)\cos(l_{CP} - l) = \cos(\delta_{GP})\sin(\delta) - \sin(\delta_{GP})\cos(\delta)\cos(\alpha - \alpha_{GP}) \end{cases} \tag{5.1}$$

where $l_{CP} = 123.932°$ is the longitude of the north celestial pole.
The inverse relations are:

$$\begin{cases} \sin(\delta) = \sin(\delta_{GP})\sin(b) + \cos(\delta_{GP})\cos(b)cos(l_{CP} - l) \\ \cos(\delta)\sin(\alpha - \alpha_{GP}) = \cos(b)\sin(l_{CP} - l) \\ \cos(\delta)\cos(\alpha - \alpha_{GP}) = \cos(\delta_{GP})\sin(b) - \sin(\delta_{GP})\cos(b)cos(l_{CP} - l) \end{cases} \tag{5.2}$$

It is possible to express Galactic coordinates in rectangular coordinates. The $XYZ$ axes are such that $X$ grows going towards the Galactic Center, $Y$ grows moving in the direction of galactic rotation and $Z$ grows moving towards the north Galactic pole. To transform from Galactic latitude and longitude to rectangular coordinates, the following relations are used:

$$\begin{cases} X_{Gal} = \cos(l)\cos(b) \\ Y_{Gal} = \sin(l)\cos(b) \\ Z_{Gal} = \sin(b) \end{cases} \tag{5.3}$$

Velocities in rectangular Galactic coordinates are typically identified as $U$, for the velocity along the $X$ direction, $V$, for the velocity along the Y direction, and $W$, for the velocity along the $Z$ direction. They can be computed using the following relations (Esa 1997):

$$\begin{pmatrix} U \\ V \\ W \end{pmatrix} = A'_G R \begin{pmatrix} k\mu_{\alpha*}A_V/\pi \\ k\mu_\delta A_V/\pi \\ kV_R \end{pmatrix} \tag{5.4}$$

where $A_V = 4.74047...$ km yr s$^{-1}$ is the astronomical unit expressed in appropriate units, $\pi$, $\mu_{\alpha*}$ (where $\mu_{\alpha*} = \mu_\alpha \cos(\delta)$) and $\mu_\delta$ are the parallax and the proper motion components expressed, respectively, in mas and mas/yr and $k = (1 - V_R/c)^{-1}$, where $V_R$ is the radial velocity of the star, is the Doppler factor. $A'_G$ and $R$ are matrices. $R$ is defined as:

$$R = \begin{pmatrix} -\sin(\alpha) & -\sin(\delta)\cos(\alpha) & \cos(\delta)\cos(\alpha) \\ \cos(\alpha) & -\sin(\delta)\sin(\alpha) & \cos(\delta)\sin(\alpha) \\ 0 & \cos(\delta) & \sin(\delta) \end{pmatrix} \tag{5.5}$$

while $A'_G$ is:

$$A'_G = \begin{pmatrix} -0.0548755604 & +0.4941094279 & -0.8676661490 \\ -0.8734370902 & -0.4448296300 & -0.1980763734 \\ -0.4838350155 & +0.7469822445 & +0.4559837762 \end{pmatrix} \tag{5.6}$$

### 5.1.2 The Local Standard of Rest

The Local Standard of Rest (LSR) is a reference frame defined by a fictional particle that moves around the plane of the Milky Way on the closed orbit in the plane that passes through the present location of the Sun. It follows that if the Milky Way is axisymmetric, such orbit is circular, otherwise it is oval. It is important to know the Sun's velocity with respect to the LSR in order to transform any observed heliocentric velocity to a local Galactic frame. In the context of this thesis, I adopt the values determined by Schönrich, Binney, and Dehnen (2010):

$$(U_\odot, V_\odot, W_\odot) = (11.1^{+0.69}_{-0.75}, 12.24^{+0.47}_{-0.47}, 7.25^{+0.37}_{-0.36})\ kms^{-1} \tag{5.7}$$

From now on, unless otherwise specified, every time I refer to $U$, $V$, $W$ velocities I consider them expressed in the LSR, meaning that they are corrected for the Sun's velocity in such reference frame.

## 5.2 TOPCAT

A fundamental software in the making of this thesis work has been TOPCAT (Tool for OPerations on Catalogues And Tables)[1]. TOPCAT is an interactive graphical viewer and editor for tabular data. It is particularly useful to deal with large tables. It is able to calculate statistics, cross-match tables and visualize data. For a further description of the software, I refer to Taylor (2005) and Taylor (2006).

## 5.3 Toomre diagrams for LOPS2 and LOPN1

In this section I present the Toomre diagrams for the two fields LOPS2 and LOPN1 and the resulting kinematic analysis.

### 5.3.1 Toomre diagrams and stellar populations

A Toomre diagram is a type of plot, vastly used for kinematic studies of stars, which displays on the horizontal axis the $V$ velocity of the stars and on the vertical axis the Toomre component of the stars, defined by the sum in quadrature of the $U$ and $W$ velocites: $T = \sqrt{U^2 + W^2}$. Toomre diagrams are particularly useful to sort out stars in terms of the stellar population that they belong to. In fact, it is known that thin disk stars, thick disk stars and halo stars concentrate on different areas of the Toomre diagram. Following the results of the work of Venn et al. (2004), who performed a Bayesian

[1] TOPCAT website

investigation of the kinematics of stars, I can roughly distinguish stars on the basis of their total velocity $V_{Tot} = \sqrt{V^2 + T^2}$. In particular, it is possible to find that:

- if $V_{Tot} \leqslant 70$ km s$^{-1}$, the star likely belongs to the thin disk;
- if $V_{Tot} > 70$ km s$^{-1}$ and $V_{Tot} \leqslant 180$ km s$^{-1}$, the star likely belongs to the thick disk;
- if $V_{Tot} > 180$ km s$^{-1}$, the star likely belongs to the halo;

Furthermore, I define two groups that, because of their particular kinematic properties, require specific attention:

- if $V < -400$ km s$^{-1}$, I identify the star as an "extreme retrograde motion target";
- if $T > 340$ km s$^{-1}$, I identify the star as an "extreme Toomre component target".

### 5.3.2 Building the Toomre diagrams

PIC targets are associated to their kinematic properties from Gaia: their Right Ascension and Declination in the ICRS system, their proper motion, their parallax and their radial velocity. In the making of this work, I used the PIC version called PIC 2.0.0. Building a Toomre diagram from these raw ingredients requires a specific recipe. As a first step, it is necessary to obtain $U$, $V$ and $W$ velocities. They were obtained using the following command in TOPCAT: >icrsToGal(astromUVW(RAdeg, DEdeg, pmRA, pmDE, RV, distance, false))

This command takes the Right Ascension and Declination (expressed in degrees), the proper motions, the radial velocity and the distance and computes the corresponding velocity in Galactic coordinates following Equation 5.4. The output coordinate system is right-handed, so that the three components are positive in the directions of the Galactic center, Galactic rotation, and the north Galactic Pole respectively. The velocities thus obtained were then corrected for the motion of the Sun in the LSR, in order to refer them to the LSR. Clearly, there is uncertainty propagation relative to these operations. The computation of the related uncertainties is described in Appendix C. At this point, it is possible to build the Toomre diagrams for the two fields.

### 5.3.3 LOPS2 Toomre diagram

I show in Fig. 5.1 the Toomre diagram relative to LOPS2, made with the data relative to 174 334 targets out of the total 179 564 targets in LOPS2 because about 5 000 stars lacked the radial velocity measurement from Gaia.

According to the criteria defined in Subsection 5.3.1, I find that:

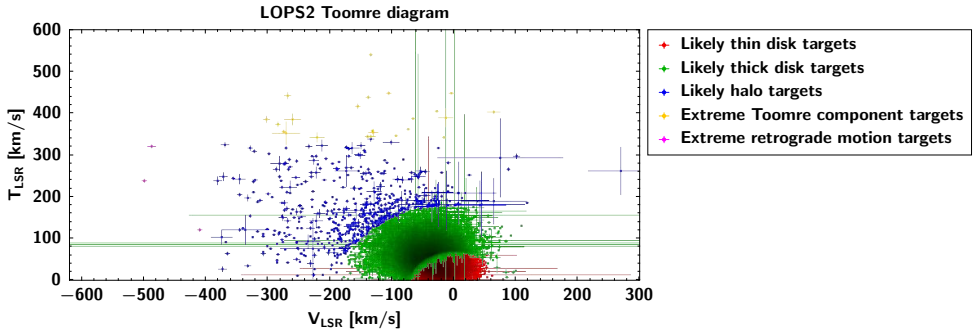


Figure 5.1: Toomre diagram for LOPS2. As expected, most stars belong to the disk populations. About 600 targets belong to the halo. There are also 26 extreme targets.

- 127 642 targets are likely to belong to the thin disk ($\sim$ 73.2% of the total sample);
- 46 071 targets are likely to belong to the thick disk ($\sim$ 26.4% of the total sample);
- 595 targets are likely to belong to the halo ($\sim$ 0.3% of the total sample);
- 23 targets are classified as extreme Toomre component targets;
- 3 targets are classified as extreme retrograde motion targets.

These results are not surprising. It is in fact natural to expect that the majority of the targets of PLATO belongs to the populations of the disk, since they are (relatively) nearby stars. There is a small but non-zero fraction of halo stars. Again, this is not surprising, since it is well known that halo stars may follow orbits that bring them close the Sun. I also found some targets characterized by extreme kinematic properties. They deserve a particular investigation.

### Extreme targets

I identified 26 extreme targets in LOPS2. I searched for them in SIMBAD[2] (Wenger et al. 2000) to see if there are interesting properties associated to them. Regarding the 3 extreme retrograde motion targets, I found information about 2 of them (1 was not found):

- CD-44 2691 (Gaia DR3 5556830959605647360): high proper motion star;
- CD-29 2277 (Gaia DR3 2905773322545989760): high proper motion star.

Regarding the 23 extreme Toomre component targets, I found information about 20 of them (3 were not found):

[2]SIMBAD website

- HD 34328 (Gaia DR3 4761346872572913408): chemically peculiar star;
- HD 29907 (Gaia DR3 4662889729476972416): spectroscopic binary;
- HD 273190 (Gaia DR3 4818949324679566720): high proper motion star;
- CD-60 1432 (Gaia DR3 5481840968055553920): high proper motion star;
- V* RY Col (Gaia DR3 4818854972838127360): RR Lyrae variable;
- CD-34 2301 (Gaia DR3 4822196285595543168): high proper motion star;
- CD-40 1349 (Gaia DR3 4840980067365790720): high proper motion star:
- L 595-22 (Gaia DR3 2910503176753011840): chemically peculiar star;
- TYC 8546-505-1 (Gaia DR3 5494999304741520768): high proper motion star;
- TYC 8502-1656-1 (Gaia DR3 4780899006812952576): high proper motion star;
- V* AV Col (Gaia DR3 2910611895263048064): RR Lyrae variable;
- LP 836-21 (Gaia DR3 2957773415014463872): chemically peculiar star;
- TYC 8516-466-1 (Gaia DR3 4774002113969313664): chemically peculiar star;
- ASAS J065847-4926.0 (Gaia DR3 5508253367659073408): RR Lyrae variable;
- L 56-29 (Gaia DR3 4653997738423471360): chemically peculiar star;
- UCAC4 149-006254 (Gaia DR3 4759040028458164480): chemically peculiar star;
- UCAC4 156-004355 (Gaia DR3 4678867935527380864): chemically peculiar star;
- SOI 821 (Gaia DR3 4654587145385190400): high proper motion star;
- L 56-35 (Gaia DR3 4653600196249261056): chemically peculiar star;
- SCR J0529-3950 (Gaia DR3 4807289862860349824): high proper motion star.

As we can see, most of the extreme targets are classified as high proper motion stars. Among them, there are 3 RR Lyrae variables, despite the fact that PLATO should target only MS and subgiant stars, 1 spectroscopic binary and 8 stars classified as chemically peculiar. It is worth to give a look at the PIC parameters of the 3 RR Lyrae variables, in order to understand how they "slipped" inside the PIC. In particular, it is interesting

to consider their effective temperature ($T_{eff}$), their radius ($R$), their mass ($M$), their distance ($D$), their absorption in the Johnson Cousin V band and their Galactic latitude $b$:

- V* RY Col: $T_{eff} \sim 6317$ K, $M \sim 1.94$ $M_\odot$, $R \sim 4.61$ $R_\odot$, $D \sim 1006$ pc, $A_V \sim 0.02$, $b \sim -35°$;
- V* AV Col: $T_{eff} \sim 6627$ K, $M \sim 1.97$ $M_\odot$, $R \sim 4.18$ $R_\odot$, $D \sim 2026$ pc, $A_V \sim 0.03$. $b \sim -23°$;
- ASAS J065847-4926.0: $T_{eff} \sim 6240$ K, $M \sim 1.99$ $M_\odot$, $R \sim 5.07$ $R_\odot$, $D \sim 1932$ pc, $A_V \sim 0.06$, $b \sim -19°$.

All the three targets are rather distant (1 or 2 kpc) and are relatively close to the Galactic plane. Given these two conditions, one would expect a much higher absorption, which, instead, for all the three targets, is unusually low. It is then highly probable that these three targets ended up in the PIC because the interstellar extinction they are subjected to was not properly accounted for. Interstellar extinction is such that stars appear fainter and redder than they really are. If this effect is not properly corrected, a luminous star subjected to heavy extinction may be considered to be an intrinsically fainter star.

### 5.3.4 LOPN1 Toomre diagram

I show in Fig. 5.2 the Toomre diagram relative to LOPN1, made with the data relative to 170 794 targets out of the total 175 597 targets in LOPN1 because about 5 000 stars lacked the radial velocity measurement from Gaia.

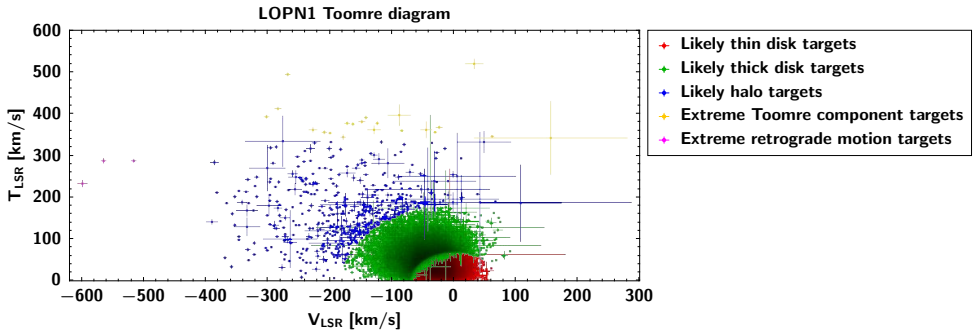


Figure 5.2: Toomre diagram for LOPN1. As expected, most stars belong to the disk populations. About 550 targets belongs to the halo. There are also 24 extreme targets.

According to the criteria defined in Subsection 5.3.1, I find that:

- 136 324 targets are likely to belong to the thin disk ($\sim$ 79.8% of the total sample);
- 33 894 targets are likely to belong to the thick disk ($\sim$ 19.8% of the total sample);
- 552 targets are likely to belong to the halo ($\sim$ 0.3% of the total sample);
- 21 targets are classified as extreme Toomre component targets;
- 3 targets are classified as extreme retrograde motion targets.

Similarly to LOPS2, most targets belong to the disk, while 552 belong to the halo. In this field I find 24 extreme targets, worth of a further investigation.

**Extreme targets**

In LOPN1 there are 24 extreme targets. I searched for them in SIMBAD to see if there are interesting properties associated to them. Regarding the 3 extreme retrograde motion targets, I found information about 2 of them (1 was not found):

- LSPM J1731+3627 (Gaia DR3 1336408284224866432): high velocity star;
- LP 335-14 (Gaia DR3 4587905579084735616): high velocity star.

Regarding the 21 extreme Toomre component targets, I found information about 17 of them (4 were not found):

- BD+42 3187 (Gaia DR3 2104987557947509888): red giant branch star;
- LSPM J2015+4411 (Gaia DR3 2081319509313600000): high proper motion star;
- V* AR Her (Gaia DR3 1398766021041835648): RR Lyrae variable;
- TYC 3077-459-1 (Gaia DR3 1341929103906579328): high proper motion star;
- TYC 3514-882-1 (Gaia DR3 1362826555046617728): high proper motion star;
- LP 45-210 (Gaia DR3 2265206777438235776): chemically peculiar star;
- Wolf 644 (Gaia DR3 1337770819649876480): chemically peculiar star;
- Ross 712 (Gaia DR3 4538449614789801216): high proper motion star;
- 2MASS J16371161+4704577 (Gaia DR3 1407226690002492544): high proper motion star;
- TYC 3932-254-1 (Gaia DR3 2155595436770674688): high proper motion star;

- GD 367 (Gaia DR3 1362976191707207552): high proper motion star;
- V* CW Her (Gaia DR3 1327053639295450880): RR Lyrae variable;
- ROTSE1 J175255.33+463216.6 (Gaia DR3 1350844459580412288): RR Lyrae variable;
- LSPM J1912+3330 (Gaia DR3 2043452431931201920): high proper motion star;
- V* AF Her (Gaia DR3 1356103870372434560): RR Lyrae variable;
- 2MASS J16293596+6057586 (Gaia DR3 1625310187102498048): high proper motion star;
- G 258-19 (Gaia DR3 1651179805919101056): high proper motion star.

Interestingly enough, I notice that among the extreme targets in LOPN1 there are some evolved stars: a red giant branch star and 4 RR Lyrae variables. There are also 2 chemically peculiar stars. The other targets are classified as high proper motion or high velocity stars. It is worth to investigate the evolved targets, as already done for LOPS2:

- BD+42 3187: $T_{eff} \sim 5595$ K, $M \sim 1.35$ $M_{\odot}$, $R \sim 2.40$ $R_{\odot}$, $D \sim 233$ pc, $A_V \sim 0.03$, $b \sim +18°$;
- V* AR Her: $T_{eff} \sim 6606$ K, $M \sim 1.99$ $M_{\odot}$, $R \sim 4.30$ $R_{\odot}$, $D \sim 1258$ pc, $A_V \sim 0.03$, $b \sim +48°$;
- V* CW Her: $T_{eff} \sim 6560$ K, $M \sim 2.17$ $M_{\odot}$, $R \sim 5.59$ $R_{\odot}$, $D \sim 2685$ pc, $A_V \sim 0.04$, $b \sim +39°$;
- ROTSE1 J175255.33+463216.6: $T_{eff} \sim 6667$ K, $M \sim 2.03$ $4M_{\odot}$, $R \sim 4.42$ $R_{\odot}$, $D \sim 2140$ pc, $A_V \sim 0.04$, $b \sim +29°$;
- V* AF Her: $T_{eff} \sim 6638$ K, $M \sim 2.16$ $M_{\odot}$, $R \sim 5.32$ $R_{\odot}$, $D \sim 2975$ pc, $A_V \sim 0.03$, $b \sim +42°$.

Once again, most of the targets are characterized by particularly large distances and unusually low absorption, suggesting that they ended up in the PIC because the interstellar extinction that they are subjected to was not taken into account properly.

## 5.4 Metallicity distributions for LOPS2 and LOPN1

Previously I separated the stars in the two fields into the different stellar components on the basis of their kinematic properties. This is a sound approach, but it is worthwhile to verify the validity of the results by studying the metallicity distributions of the various groups of targets that I obtained. As a matter of fact, I expect the disk stars to have a higher $[Fe/H]$ than halo stars. In Section 4.2 I explained that I expect halo stars to be characterized by a particularly low metallicity, typically $[Fe/H] < -0.8$, while disk stars tend to have higher metallicities, with a particular prominence at about $[Fe/H] \approx -0.5$. In this section I study the metallicity distributions for the two fields.

### 5.4.1 LOPS2 metallicity distribution

In this subsection I study the metallicity distribution of LOPS2 targets. To do so, I firstly use the metallicity measurements from Gaia (column "[Fe/H]" in the Gaia dataset), since I have them for most of the targets in the Toomre diagrams (146 281 out of 174 334 targets for LOPS2).

I start by showing in Fig. 5.3 the Toomre diagram for LOPS2, color-coded for the metallicities of the stars.

It is immediately visible at a glance that there is a decrease in metallicity going from disk stars, which are darker, to halo and extreme stars, which are lighter. I investigate this trend further by looking at the metallicity distribution, shown in Fig. 5.4.

The mean metallicity is $[Fe/H] = -0.31$ and the standard deviation is $\sigma = 0.32$. I notice that thin disk and thick disk stars do indeed have, on average, a higher metallicity than halo and extreme stars. In particular, both thin disk and thick disk stars metallicity distributions peak at about $[Fe/H] = -0.3$, while halo stars have a more uniform distribution and there is a larger fraction of them that has low metallicity. In particular, the mean metallicities and the standard deviations for each group are:

- likely thin disk targets (107 499 targets): $[Fe/H] = -0.30$, $\sigma = 0.31$;
- likely thick disk targets (38 295 targets): $[Fe/H] = -0.30$, $\sigma = 0.32$;
- likely halo targets (463 targets): $[Fe/H] = -0.90$, $\sigma = 0.54$;
- extreme Toomre component targets (21 targets): $[Fe/H] = -1.55$, $\sigma = 0.66$;
- extreme retrograde motion targets (3 targets): $[Fe/H] = -2.13$, $\sigma = 0.40$;

I notice that there is a small number of disk stars presenting particularly low metallicities, covering the range from $[Fe/H] \approx -3$ to $[Fe/H] \approx -4$. Clearly, as a consequence of the metallicity distributions, while a significant fraction of disk stars is characterized by super-solar metallicities, most of halo stars are characterized by sub-solar metallicities.

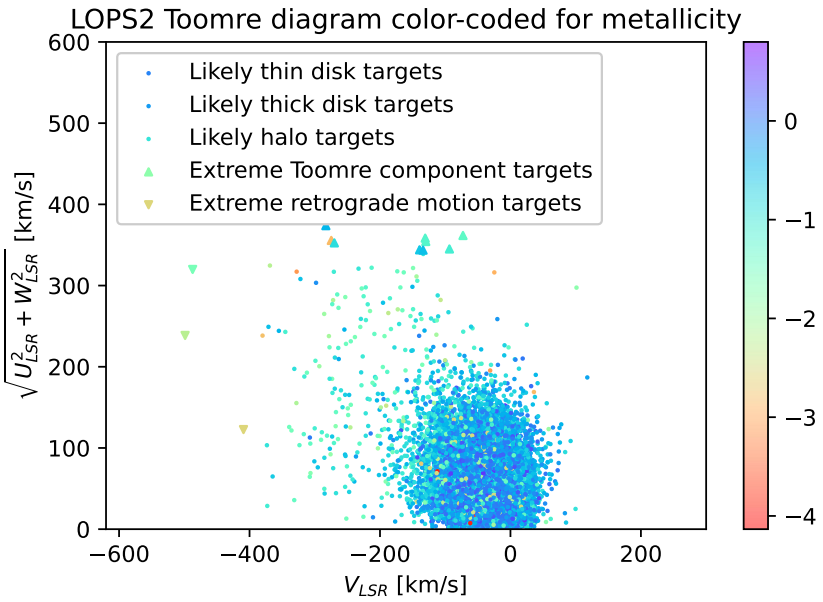


Figure 5.3: Toomre diagram for LOPS2 color-coded for metallicity. It appears visually that there is a decrease in metallicity moving from the denser region of the diagram, corresponding to the disk stars, to the less populated regions of the diagram, corresponding to halo and extreme stars.

It is worth to consider also metallicity measurements from other surveys, since Gaia metallicities are known to not be fully reliable (Bianchini and Mastrobuono-Battisti 2024). In particular, I consider the measurements included in the sixth data release of the RAVE (Radial Velocity Experiment) survey (Steinmetz et al. 2020, Steinmetz et al. 2020). RAVE is a magnitude-limited ($9 < I < 12$) spectroscopic survey of stars randomly selected in the southern sky. The RAVE medium-resolution spectra ($R \approx 7500$) cover the Ca-triplet region (8410 - 8795 Å) and span the complete time frame from the start of RAVE observations on 12 April 2003 to their completion on 4 April 2013. RAVE DR6, the final data release, is based on 518 387 observations of 451 783 unique stars. It includes wavelength-calibrated and flux-normalized spectra and error spectra for all observations, spectral classification and radial velocities of the targets, spectroscopically-derived atmospheric stellar parameters, enhanced stellar atmospheric parameters obtained with Bayesian methods, asteroseismically-calibrated stellar parameters for giant stars and, most importantly for this work, elemental abundances. The accuracy for elemental abundances is at the level of $\approx 0.1 - 0.2$ dex (see Fig. 4.5.3 in Steinmetz et al. 2020).

I cross-matched the PIC with the RAVE DR6 catalogue using TOPCAT. To do so, I compared the stars in the two catalogues to identify those which presented a separation

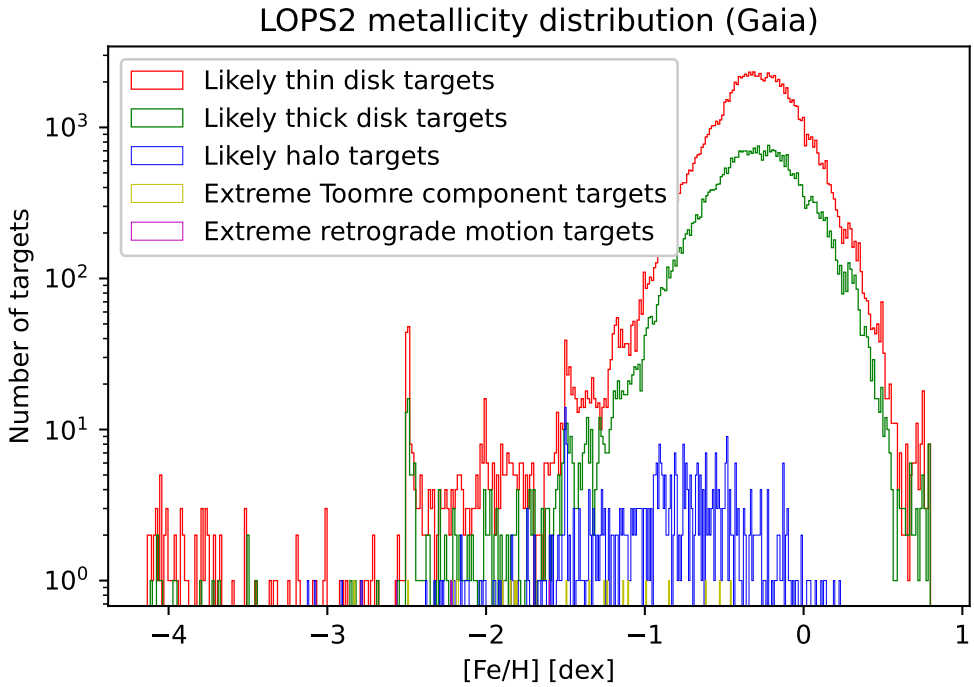


Figure 5.4: Metallicity distribution (from Gaia data) for LOPS2. The vertical axis in logarithmic, so that differences among the populations become appreciable.

within 1 arcsec. In both catalogues stars are associated to their position from Gaia DR3 (RAVE DR6 data can be retrieved already cross-matched with Gaia DR3), so I expect to have selected all the targets which are present in both catalogues. Out of the LOPS2 targets represented in the Toomre diagram, 8 858 are associated to a measurement of metallicity from RAVE DR6. However, one star (UCAC2 9410604, which has Gaia identification: Gaia DR3 5502341980830214272) is associated to an extremely low metallicity ($[Fe/H] = -8.31$), so I decided to not take into consideration such object, as its metallicity is "unphysically" low and is most likely due to a catalogue error. In Fig. 5.5 I show the metallicity distribution for such LOPS2 targets using RAVE DR6 data.

With respect to the metallicity distribution obtained using Gaia data, metallicities seem to be higher. The mean metallicity of the distribution is $[Fe/H] = -0.03$ and the standard deviation is $\sigma = 0.26$. The mean metallicity and the standard deviation for each group are:

- likely thin disk targets (6436 targets): $[Fe/H] = -0.02$, $\sigma = 0.25$;
- likely thick disk targets (2404 targets): $[Fe/H] = -0.05$, $\sigma = 0.28$;

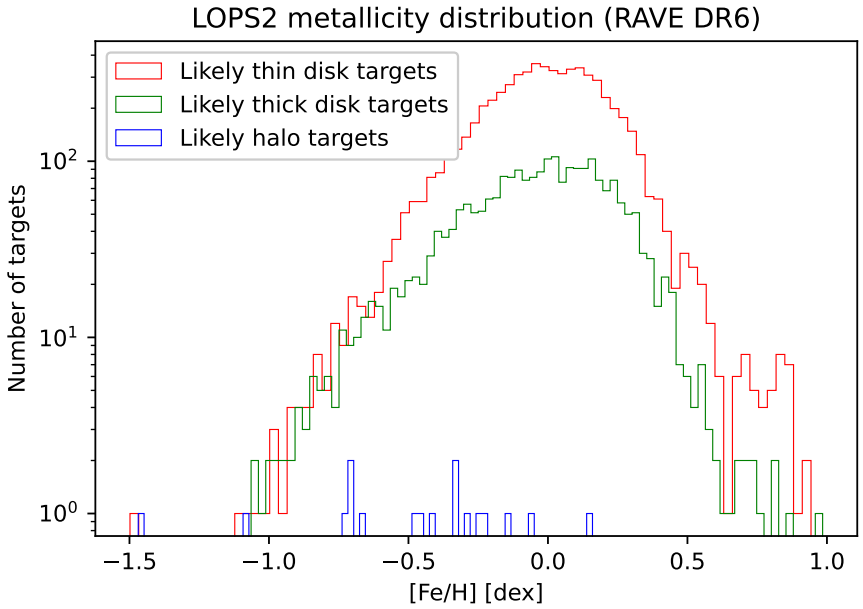


Figure 5.5: Metallicity distribution using RAVE DR6 data for LOPS2. The vertical axis in logarithmic, so that differences among the populations become appreciable.

- likely halo targets (17 targets): $[Fe/H] = -0.48$, $\sigma = 0.38$.

Indeed, the mean metallicity for each group is higher than the one obtained for the same group with Gaia. To see whether this effect is genuine or simply due to a a biased sample, I consider the metallicity distributions obtained using Gaia data and RAVE DR6 data overlapped. To do so, I select only the 7 4989 targets which have a (reasonable) measurement of metallicity from both surveys. The overlapping metallicity distributions are shown in Fig. 5.6.

By looking at the overlapping distributions, the impression seems correct: RAVE DR6 metallicity distributions peak at higher values than Gaia metallicity distributions. In particular, for the 7 489 targets that are featured in both surveys, the mean values are:

- likely thin disk targets (5 508 targets): $[Fe/H]_{RAVE} = -0.01$ and $\sigma_{RAVE} = 0.25$, $[Fe/H]_{Gaia} = -0.14$ and $\sigma_{Gaia} = 0.28$;
- likely thick disk targets (1 974 targets): $[Fe/H]_{RAVE} = -0.04$ and $\sigma_{RAVE} = 0.28$, $[Fe/H]_{Gaia} = -0.13$ and $\sigma_{Gaia} = 0.28$;
- likely halo targets (7 targets): $[Fe/H]_{RAVE} = -0.56$ and $\sigma_{RAVE} = 0.40$, $[Fe/H]_{Gaia} = -0.43$ and $\sigma_{Gaia} = 0.29$.

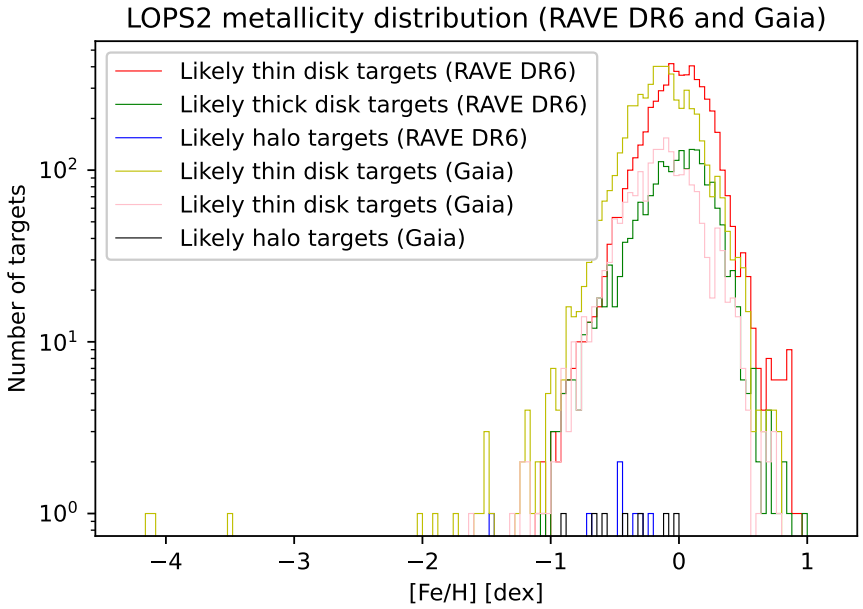


Figure 5.6: Metallicity distributions using RAVE DR6 data and Gaia data for LOPS2. The vertical axis in logarithmic, so that differences among the populations become appreciable. The distributions obtained using RAVE DR6 data peak at higher metallicities than the distributions obtained with Gaia data.

With the exception of halo targets, whose number is however very small, the metallicity measurements from RAVE are, on average, higher than the Gaia ones for the considered stellar populations.

Let us see now the metallicity distributions, from both surveys, of each stellar population in detail.

### Thin disk targets metallicity distributions

There is a total of 5 508 thin disk targets which have a (reasonable) metallicity measurement from both surveys. In Fig. 5.7 I show the metallicity distributions for such targets using both RAVE DR6 and Gaia data.

As we can see, the effect I previously observed, namely that RAVE DR6 metallicity measurements appear higher than the Gaia ones, is proven to be true for the same stars observed in both surveys.

Now I investigate the nature of the metallicity distribution of thin disk targets in LOPS2. “By eye” I notice immediately that it resembles a Gaussian distribution. Using the Python package scipy, I fit the distribution obtained with Gaia to a Gaussian distribution using the function “optimize”. I obtain the fit in Fig. 5.8. As we can see, the fit

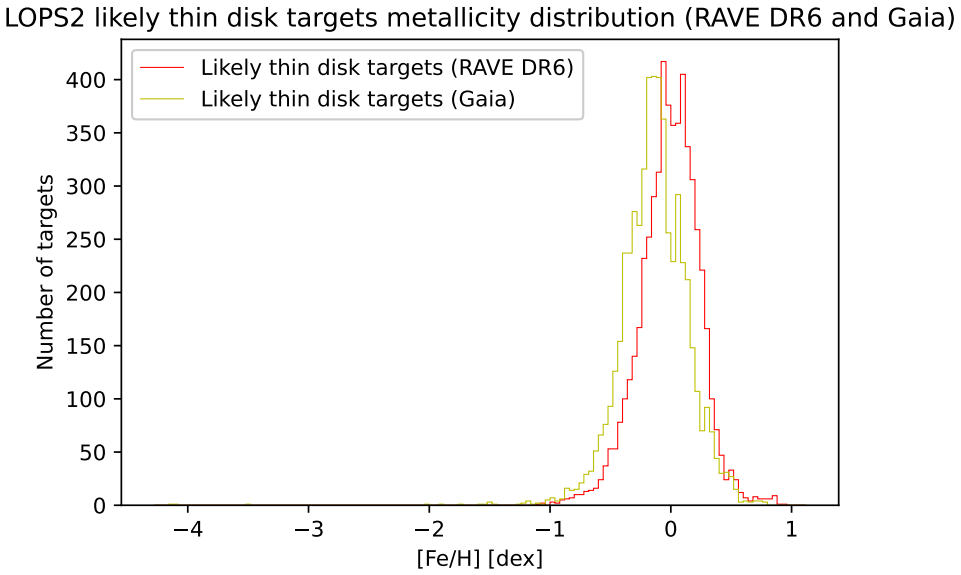


Figure 5.7: Metallicity distributions using RAVE DR6 data and Gaia data for likely thin disk targets in LOPS2. The metallicity distribution from RAVE DR6 is characterized by a higher mean value with respect to the metallicity distribution from Gaia.

describes well the data. The function scipy.optimize does not provide me with the $\chi^2$, but I notice that the diagonal elements of the covariance matrix are small, meaning that a Gaussian function is a good fit for the data. Furthermore, it is reasonable to expect that metallicity distribution of the thin disk targets is described by a Gaussian function.

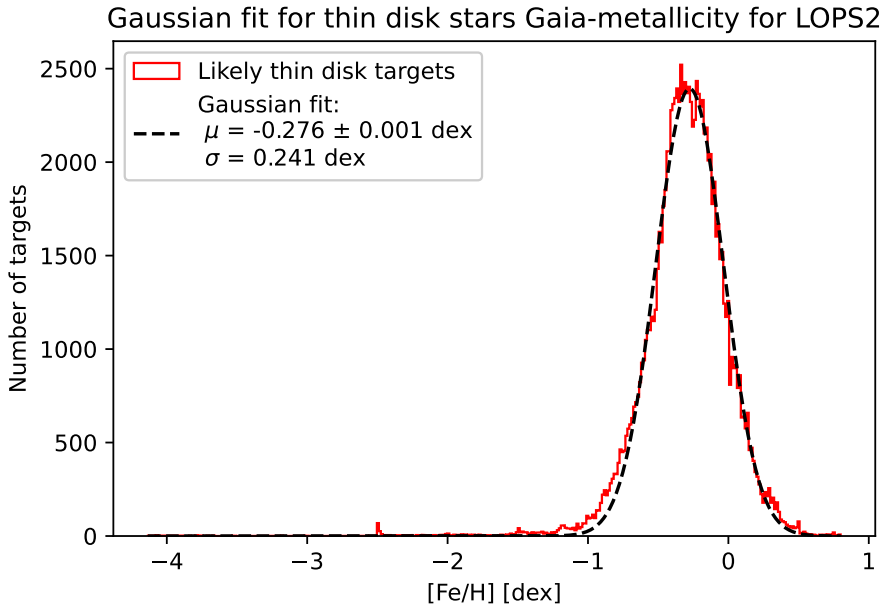


Figure 5.8: Metallicity distribution using Gaia data for likely thin disk targets in LOPS2 and the associated Gaussian fit.

I can do the same exercise using RAVE DR6 data, resulting in Fig. 5.9.

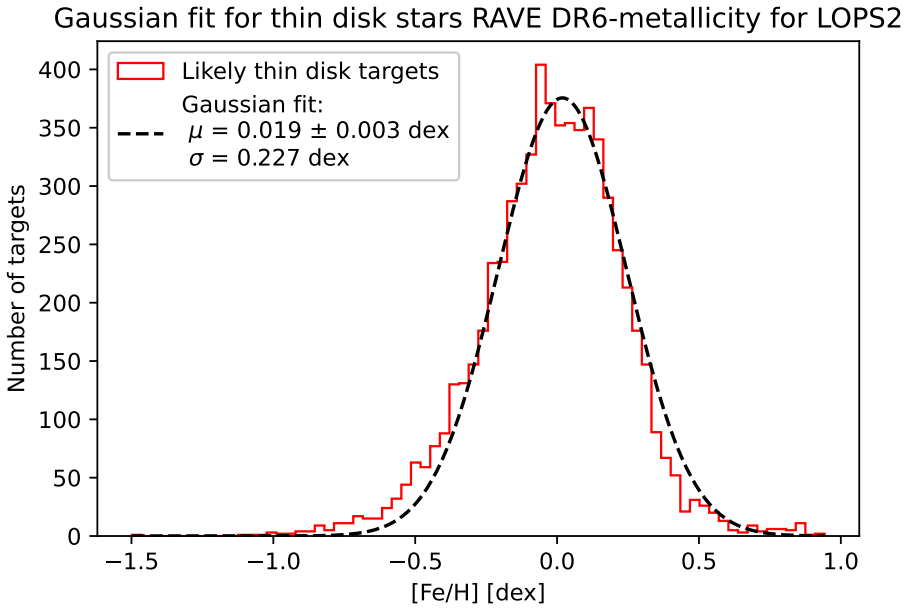


Figure 5.9: Metallicity distribution using RAVE DR6 data for likely thin disk targets in LOPS2 and the associated Gaussian fit.

Once again, not surprisingly the data are well described by a Gaussian fit.

### Thick disk targets metallicity distribution

There is a total of 1 974 thick disk targets which have a metallicity measurement from both surveys. In Fig. 5.10 I show the metallicity distributions for such targets using both RAVE DR6 and Gaia data.

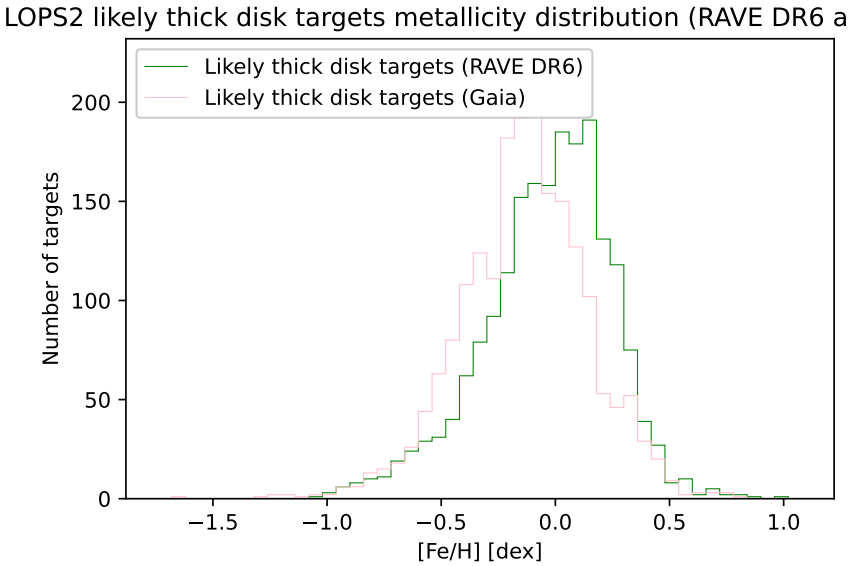


Figure 5.10: Metallicity distributions using RAVE DR6 data and Gaia data for likely thick disk targets in LOPS2. The metallicity distribution from RAVE DR6 is characterized by a higher mean value with respect to the metallicity distribution from Gaia.

As we can see, the effect I previously observed, namely that RAVE DR6 metallicity measurements appear higher than the Gaia ones, is proven to be true for the same stars observed in both surveys.

Also in this case I proceed with the Gaussian fit for the associated Gaia data. The results are presented in Fig 5.11.

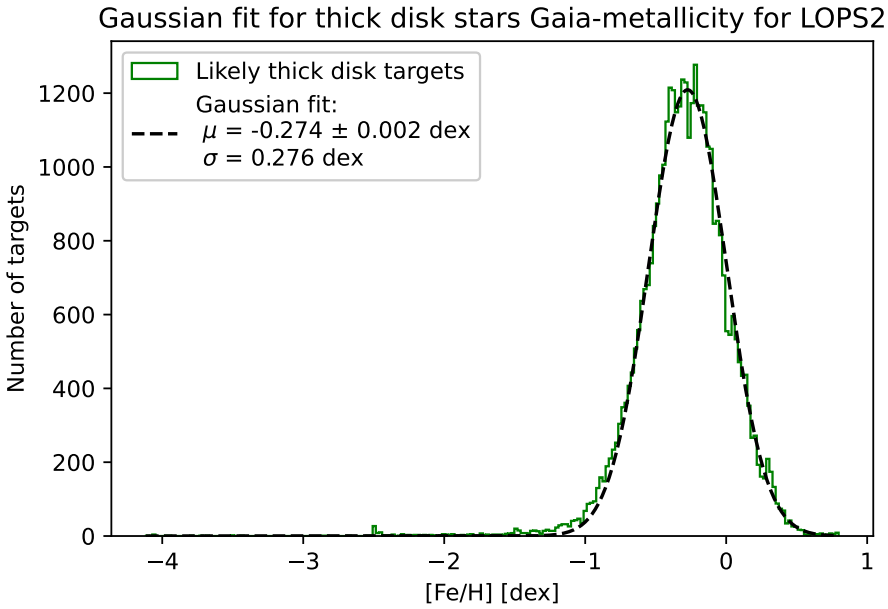


Figure 5.11: Metallicity distribution using Gaia data for likely thick disk targets in LOPS2 and the associated Gaussian fit.

The data are well described by a Gaussian function. I repeat the same procedure using RAVE DR6 data, obtaining Fig. 5.12.

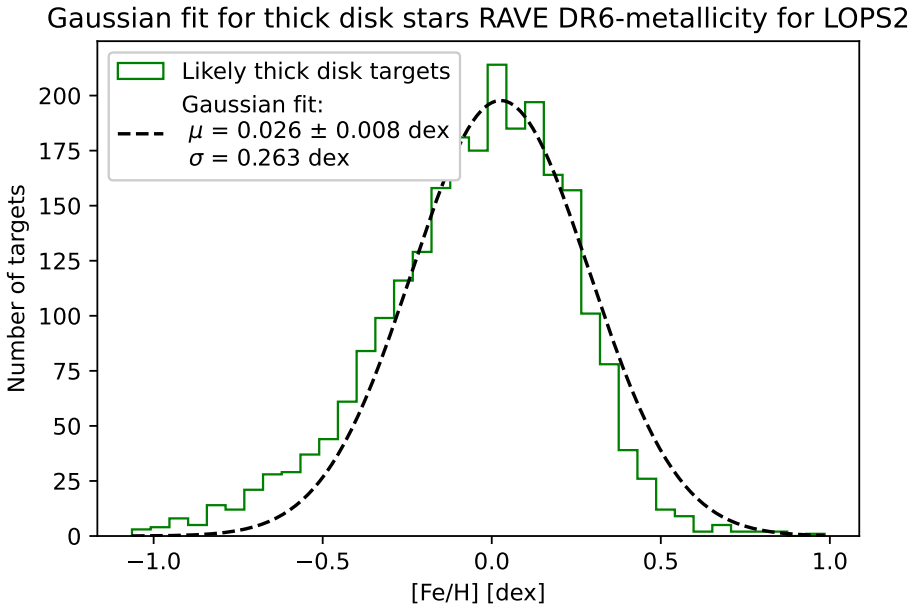


Figure 5.12: Metallicity distribution using RAVE DR6 data for likely thick disk targets in LOPS2 and the associated Gaussian fit.

The metallicity distribution follows a Gaussian profile.

### Halo targets metallicity distribution

There is a total of 7 halo targets which have a metallicity measurement from both surveys. In Fig. 5.13 I show the metallicity distributions for such targets using both RAVE DR6 and Gaia data.

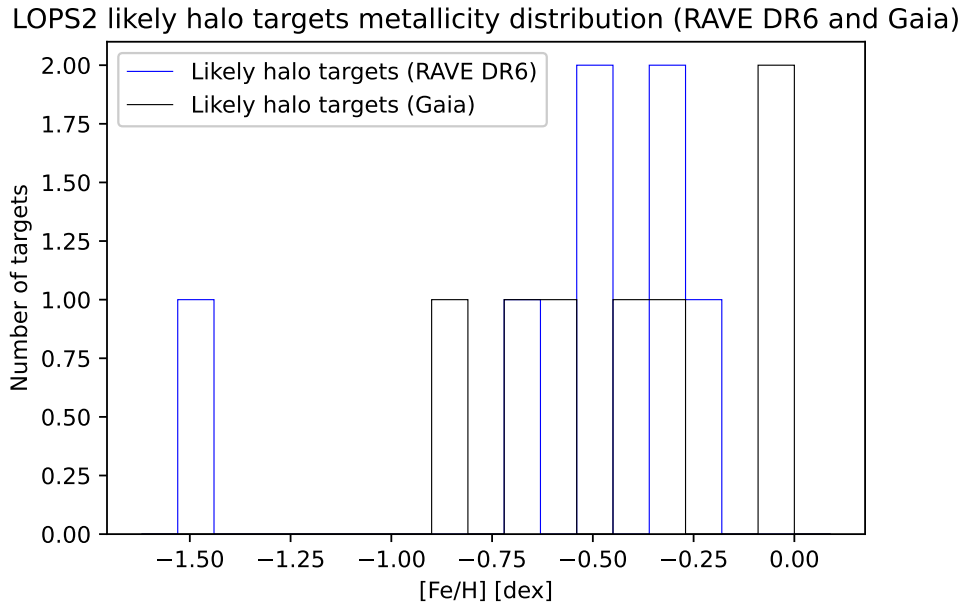


Figure 5.13: Metallicity distributions using RAVE DR6 data and Gaia data for likely thick disk targets in LOPS2. The metallicity distribution from RAVE DR6 is characterized by a smaller mean value with respect to the metallicity distribution from Gaia.

Contrary to what happens for thin disk and thick disk stars, in this case Gaia metallicities are, on average, higher than RAVE DR6 metallicities. I must stress, however, that I have only 10 targets at my disposal, meaning that these results must be taken with a grain of salt.

I proceed with the Gaussian fit for the metallicity distribution of halo targets using Gaia data. The results are presented in Fig. 5.14.

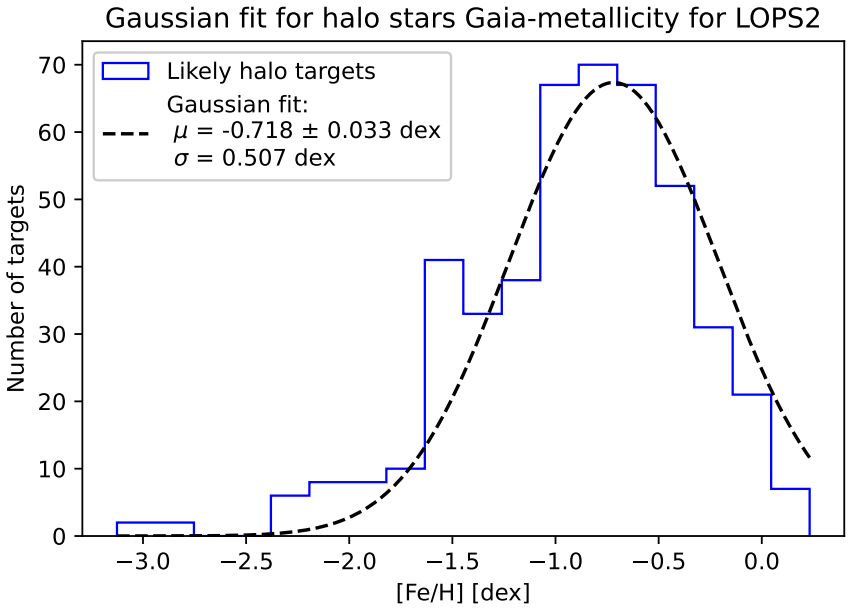


Figure 5.14: Metallicity distribution using Gaia data for likely halo targets in LOPS2 and the associated Gaussian fit.

Overall, the Gaussian function looks like a reasonable fit for the metallicity distribution.

### Extreme targets metallicity distribution

There are 21 extreme Toomre component targets and 3 extreme retrograde motion targets for which I have a measurement of metallicity from Gaia. Their distributions are shown in Fig. 5.15.

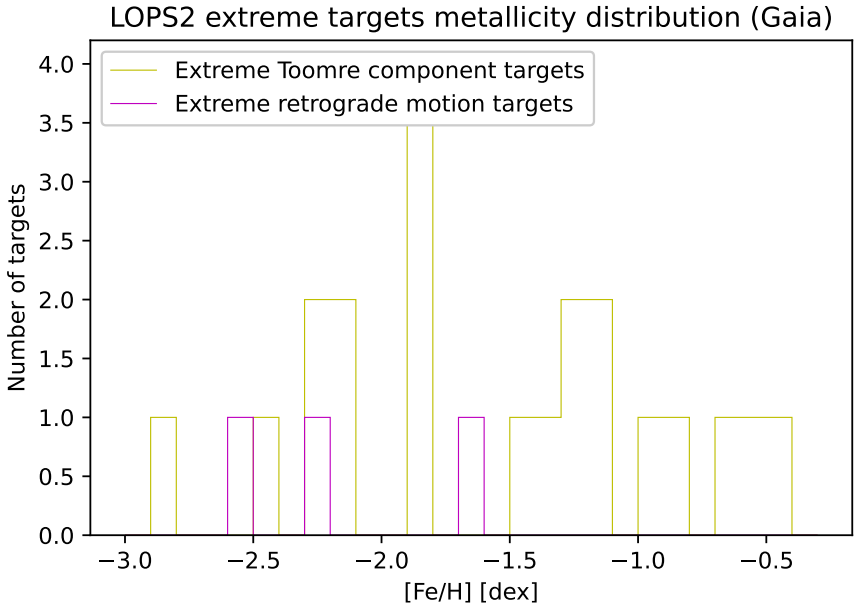


Figure 5.15: Metallicity distribution using Gaia data for extreme targets in LOPS2.

I notice that they are characterized by a rather low metallicity, with the most metal-rich star having $[Fe/H] \approx -0.4$ and the most metal-poor one having $[Fe/H] \approx -2.8$.

### 5.4.2 LOPN1 metallicity distribution

In this subsection I study the metallicity distribution of LOPN1 targets. To do so, I use the measurements of metallicity from Gaia. Out of the 170 794 targets appearing in the LOPN1 Toomre diagram, 145 428 are associated to a Gaia measurement of metallicity. I start by showing in Fig. 5.16 the Toomre diagram for LOPN1, color-coded for the metallicities of the stars.

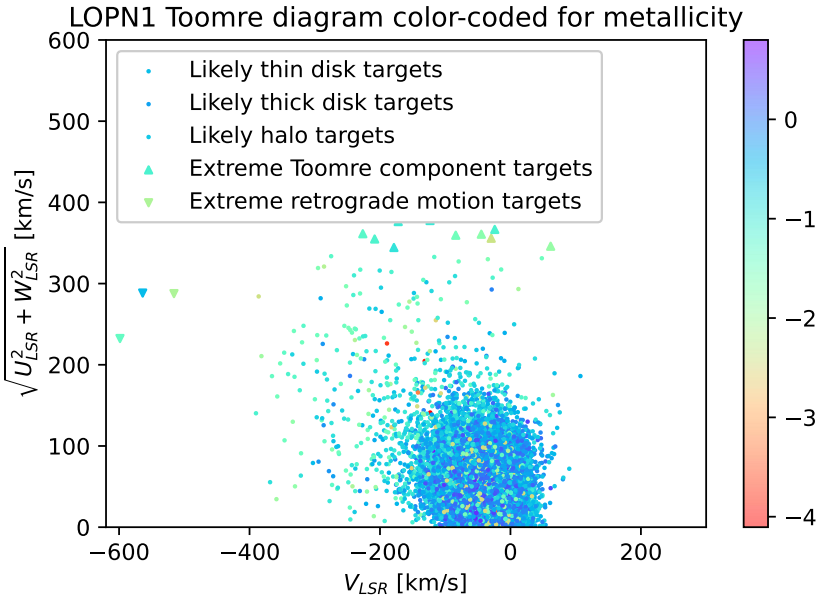


Figure 5.16: Toomre diagram for LOPN1 color-coded for metallicity. It appears visually that there is a decrease in metallicity moving from the denser region of the diagram, corresponding to the disk stars, to the less populated regions of the diagram, corresponding to halo and extreme stars.

Similarly to what I found when dealing with LOPS2, I notice that there is a decrease in metallicity going from disk stars to halo stars. Let us visualize this phenomenon more clearly by looking at the metallicity distribution, presented in Fig. 5.17.

The mean metallicity is $[Fe/H] = -0.25$ and the standard deviation is $\sigma = 0.30$. Thin and thick disk stars are characterized by a higher mean metallicity, peaking at about $[Fe/H] \approx -0.2$. The distribution for halo stars is less peaked and has a smaller mean metallicity. In particular, the mean metallicity and the standard deviation for each group are:

- likely thin disk targets (116 328 targets): $[Fe/H] = -0.24$, $\sigma = 0.28$;
- likely thick disk targets (28 613 targets): $[Fe/H] = -0.27$, $\sigma = 0.34$;

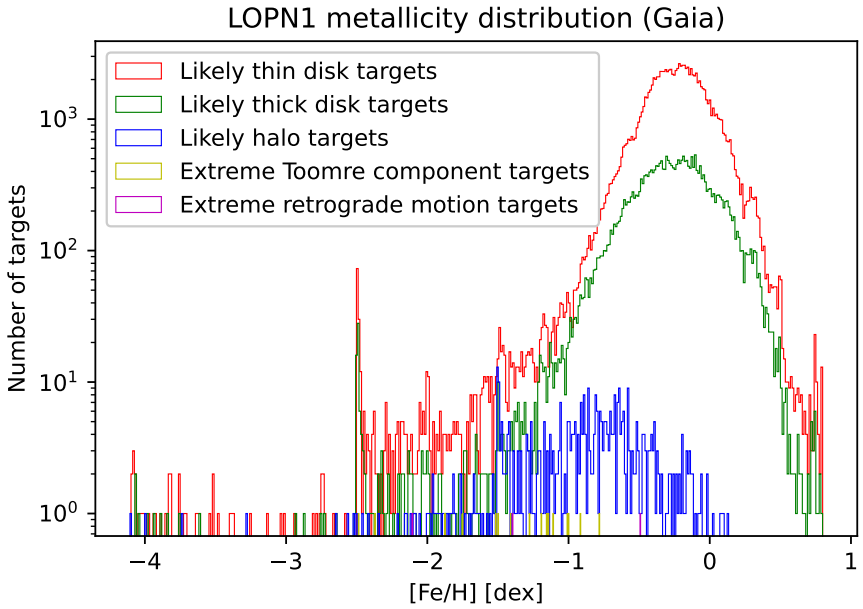


Figure 5.17: Metallicity distribution using Gaia data for LOPN1. The vertical axis in logarithmic, so that differences among the populations become appreciable.

- likely halo targets (468 targets): $[Fe/H] = -0.96$, $\sigma = 0.57$;
- extreme Toomre component targets (16 targets): $[Fe/H] = -1.41$, $\sigma = 0.48$;
- extreme retrograde motion targets (3 targets): $[Fe/H] = -1.33$, $\sigma = 0.66$;

Also in this case, I notice that, despite the fact that disk stars stars have a higher mean metallicity, some of them are characterized by extremely low metallicities, reaching levels as low as $[Fe/H] \approx -4$. In any case, while while a significant fraction of disk stars is characterized by super-solar metallicities, most of halo stars are characterized by sub-solar metallicities.

Let me now consider the metallicity distribution for each stellar component in detail.

### Thin disk targets metallicity distribution

I want to investigate the nature of the metallicity distribution for likely thin disk targets in LOPN1. To do so, I perform the same exercise that I did in Subsection 5.4.1: I fit the distribution to a Gaussian function. The results are shown in Fig. 5.18.

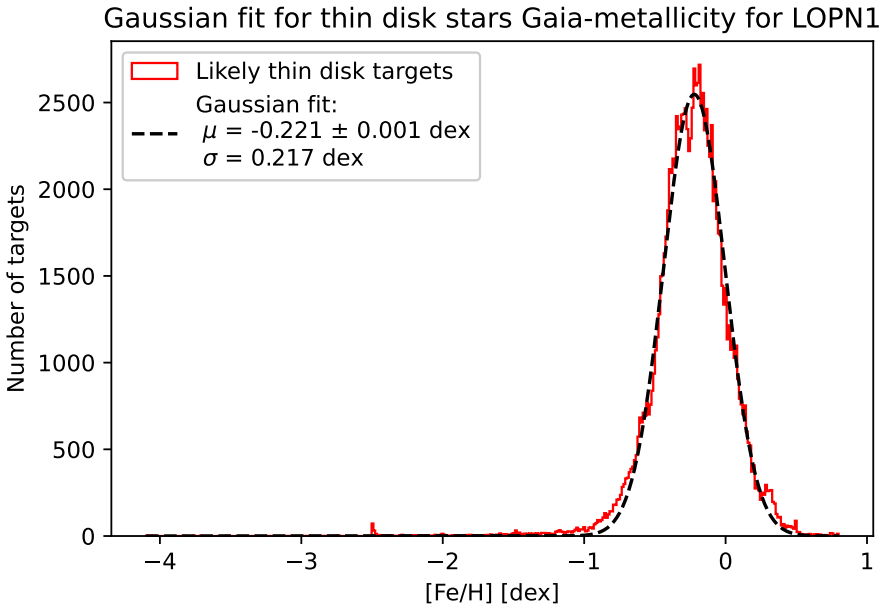


Figure 5.18: Metallicity distribution using Gaia data for likely thin disk targets in LOPN1 and the associated Gaussian fit.

As we can see, similarly to what I found for LOPS2, the Gaussian function describes well the data.

### Thick disk targets metallicity distribution

I fit the metallicity distribution of likely thick disk targets in LOPN1 to a Gaussian function. The results are shown in Fig. 5.19.

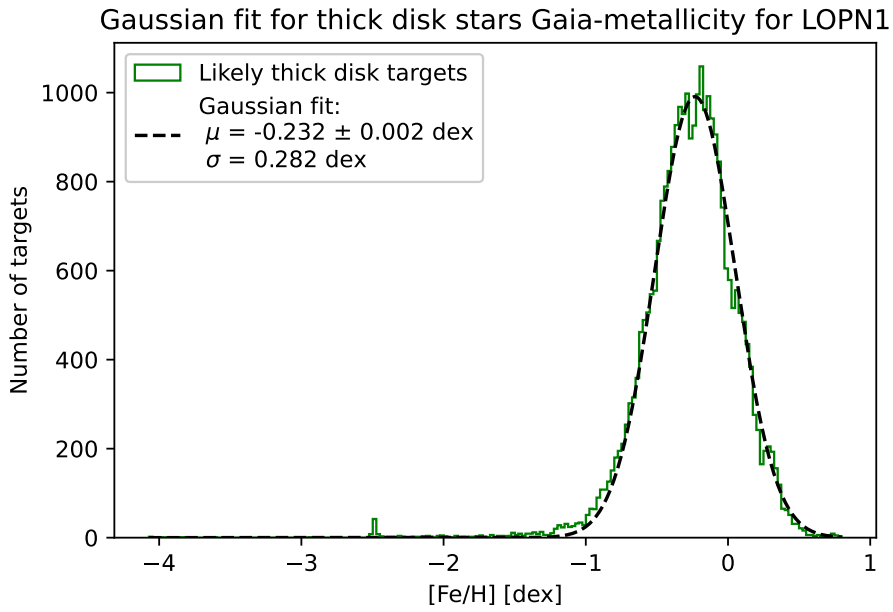


Figure 5.19: Metallicity distribution using Gaia data for likely thick disk targets in LOPN1 and the associated Gaussian fit.

Not surprisingly, the Gaussian distribution is a good fit for the data.

### Halo targets metallicity distribution

I fit the metallicity distribution of likely halo targets in LOPN1 to a Gaussian function. The results are shown in Fig. 5.20.

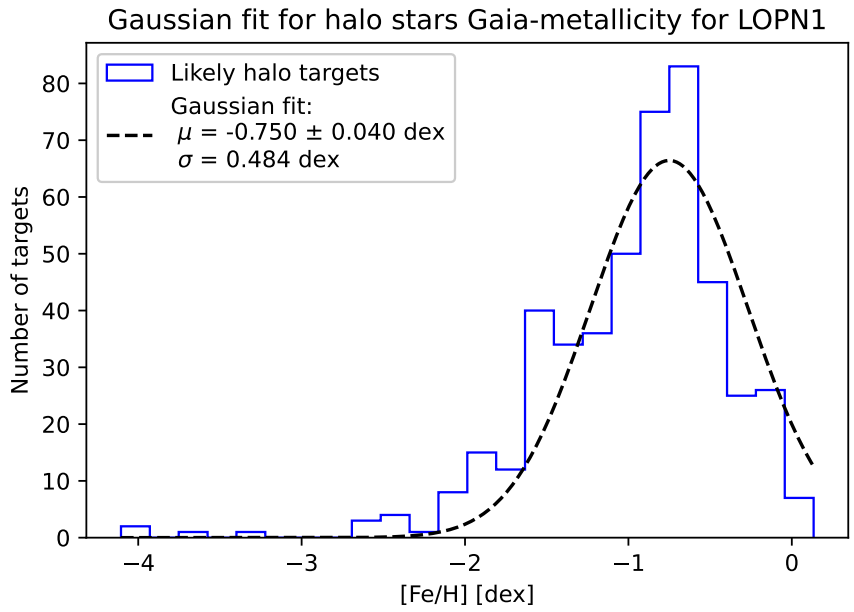


Figure 5.20: Metallicity distribution using Gaia data for likely halo targets in LOPN1 and the associated Gaussian fit.

The Gaussian function is a reasonable fit for the metallicity distribution.

**Extreme targets metallicity distribution**

There are 16 extreme Toomre component targets and 3 extreme retrograde motion targets that are associated to a metallicity measurement from Gaia. Similarly to what I found for extreme targets in LOPS2, they are characterized by low metallicities, with the most metal-rich target having $[Fe/H] \approx -0.5$ and the most metal-poor target having $[Fe/H] \approx -2.5$. Their metallicity distribution is presented in Fig. 5.21.

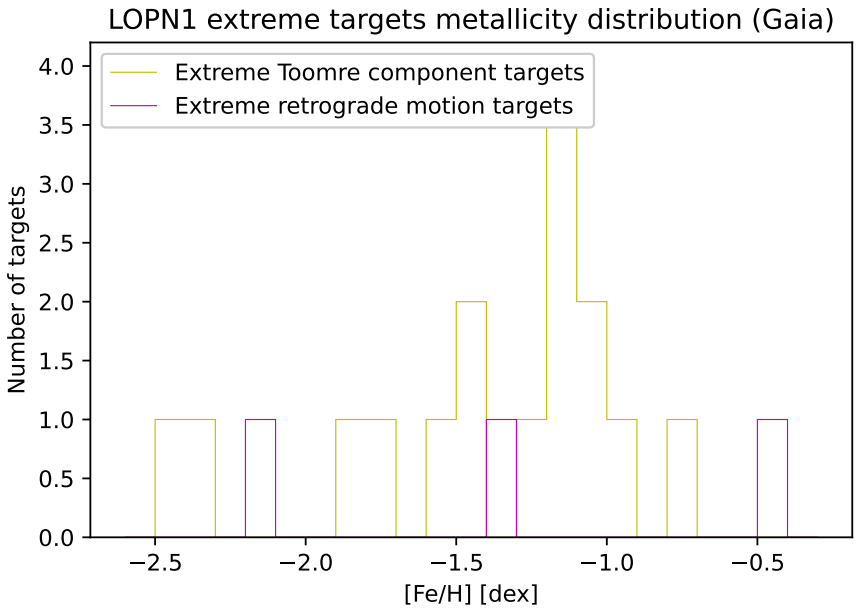


Figure 5.21: Metallicity distribution using Gaia data for extreme targets in LOPN1.

## 5.5 Positions of targets

In this section I show the positions of the targets in the PIC in Galactic coordinates $XYZ$. These are obtained using the measurements of Right Ascension, Declination and distance from Gaia.

### 5.5.1 LOPS2 targets positions

In Fig 5.22 the plots representing the targets in terms of their $X-Y$, $X-Z$ and $Y-Z$ positions are shown. Halo-associated targets appear to be more clustered around the zero-points than disk-associated targets. The same can be said about extreme targets, which, with a couple of exceptions, also tend to cluster around the zero-points.

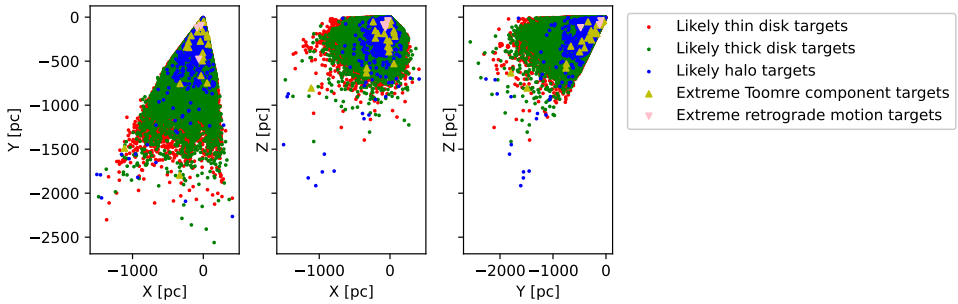


Figure 5.22: $X-Y, X-Z$ and $Y-Z$ positions of LOPS2 targets

The most distant star in LOPS2, which is Gaia DR3 5606458031102770176 (no match was found in SIMBAD), is located at a distance of $D \approx 2780$ pc and is not associated to a stellar component, since it does not have a radial velocity measurement from Gaia. The closest one, which is HD 33793 (Gaia DR3 4810594479418041856), is located at a distance of $D \approx 4$ pc and is associated to the Halo.

### 5.5.2 LOPN1 targets positions

In Fig 5.23 the plots representing the targets in terms of their $X-Y$, $X-Z$ and $Y-Z$ positions are shown. Similarly to what was found for LOPS2, Halo-associated targets and extreme targets appear to be more clustered around the zero-points than disk associated targets.

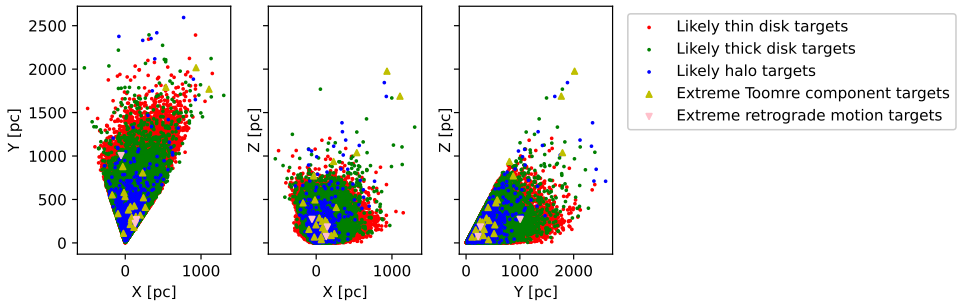


Figure 5.23: $X-Y, X-Z$ and $Y-Z$ positions of LOPN1 targets

The most distant target in LOPN1 is V* AF Her (Gaia DR3 1356103870372434560), an extreme Toomre component star which is located at a distance of $D \approx 2975$ pc. It is an RR-Lyrae variable and its presence in the PIC was discussed in Subsection 5.3.4. The closest target in LOPN1, HD 173740 (Gaia DR3 2154880616774131712), is located at a distance of $D \approx 3.5$ pc. It is associated to the thin disk.

Table 5.1: Comparison of LOPS2 results

| Stellar component | My results | Paper results |
|---|---|---|
| Thin disk | 127 642 ($\sim$ 73.2%) | 80 954 ($\sim$ 65.3%) |
| Thick disk | 46 071 ($\sim$ 26.4%) | 42 522 ($\sim$ 34.3%) |
| Halo | 621 ($\sim$ 0.3%) | 426 ($\sim$ 0.3%) |

## 5.6 Comparison with the results of other papers

In this section I compare my results with the results obtained by other authors.

### 5.6.1 Results comparison: kinematics

The study of the kinematic properties of PIC targets is a relatively new line of research, since PIC targets and the fields that will be observed or have been proposed have been decided only in the last few years. Recently, a paper by Boettner, Viswanathan, and Dayal (2024) appeared on arXiv[3], whose aim is the kinematic classification of PIC targets in terms of the stellar components of the Galaxy. It is then worth to compare the results they obtained with the ones that I have presented in this work. They considered targets whose uncertainties on their parallaxes, proper motions and radial velocities from Gaia DR3 do not exceed 20%. Furthermore, they considered only targets which have an estimate of their metallicity and surface gravity. As a consequence of these criteria, their LOPS2 sample is composed of 123 902 targets, while mine is composed of 174 334 targets, and their LOPN1 sample is composed of 132 078 targets, while mine is composed of 170 794 targets. The difference in the total numbers between my study and theirs arises from the fact that the only limiting factor that I considered when studying the kinematics of the targets is the presence (or not) of radial velocity measurements for such targets in Gaia DR3.

To classify the targets in terms of their stellar component, they followed a probabilistic approach developed by Bensby, Feltzing, and Lundström (2003, 2014). This method is based entirely on the kinematics of stars and in particular on their velocities in the Galactic reference frame $U_{LSR}$, $V_{LSR}$ and $W_{LSR}$. I refer to the referenced papers for the details. My classification method is also based purely on the kinematics of stars and in particular on their velocities $U_{LSR}$, $V_{LSR}$ and $W_{LSR}$. However, to classify the stars I used the set of inequalities presented in subsection 5.3.1.

In Table 5.1 and Table 5.2 I compare my results with theirs.

Before starting to compare the results, I need to make two remarks. The first one is that in the paper by Boettner, Viswanathan, and Dayal, they considered a large frac-

[3] arXiv website

Table 5.2: Comparison of LOPN1 results

| Stellar component | My results | Paper results |
|---|---|---|
| Thin disk | 136 324 ($\sim$ 79.8%) | 85 626 ($\sim$ 64.8%) |
| Thick disk | 33 894 ($\sim$ 19.8%) | 46 000 ($\sim$ 34.8%) |
| Halo | 576 ($\sim$ 0.3%) | 452 ($\sim$ 0.3%) |

tion the targets to be "Thick Disk candidate" and "Halo candidate", as they were not clearly classifiable. In the tables presented here, I consider candidate targets to belong to the component that they are associated to. Secondly, in my analysis I have identified some targets characterized by particularly extreme kinematic properties: the "extreme Toomre component targets" and the "extreme retrograde motion targets". In the tables presented here, they are summed to the Halo-associated targets, as their extreme kinematic properties suggest that they belong to such component, and, as a matter of fact, they satisfy the inequality that I used to identify likely halo targets.

Let me now discuss the numbers presented in Tables 5.1 and 5.2. There are some discrepancies between mine and their results, which are particularly marked for LOPN1. In fact, while for LOPS2 the percentage difference of targets classified as thin disk and thick disk between the two studies is about 8%, for LOPN1 it is about 15%, almost double the value for LOPS2. Regarding the targets classified as halo stars, we found similar results. The differences between my and their results may arise for a series of reasons. The first one is that we used two different methods to classify the targets, although they are both based only on the kinematics of stars. Secondly, as noted before, Boettner, Viswanathan, and Dayal classified a significant part of the targets they analyzed as "candidate", meaning that the classification scheme they followed was not able to clearly classify such targets. Therefore the classification of such targets is to be taken with a grain of salt. Another aspect to consider regards my classification approach. I classified the targets according to the inequalities listed in subsection 5.3.1. However, this approach is somewhat "rough", in the sense there is a transition region in the velocity space in which the classification of the targets is not really straightforward (hence the fact that I chose to name the populations that I identified as "likely thin disk", "likely thick disk" and "likely halo", as, for some of the targets - particularly those whose velocities happen to lie close to the limits defined by the set of inequalities - the classification is not entirely clear). We must also keep in mind that we considered different samples, as they analyzed reduced samples with respect to mine. Finally, it is worth considering that, as I have already discussed in previous sections, stellar components differ not only by their kinematics, but also by their metallicity distributions. For a proper classifications of the targets, metallicity has to be considered, since otherwise contamination could play an important role. This explains the importance of the work

I performed in previous section, where I analyzed the metallicity of the targets in order to confirm the validity of the kinematic analysis.

### 5.6.2 Results comparison: chemical composition

In a similar fashion to what I did, Boettner, Viswanathan, and Dayal also investigated the metallicity distributions of the PIC targets. In particular, they used metallicities extracted from high-resolution spectra coming from APOGEE DR17 (Abdurro'uf et al. 2022) and GALAH DR3 (Buder et al. 2021). Since the metallicity measurements from those surveys are not present for most of PIC targets, they studied the metallicities of only about 5% of the sample of all-sky PIC targets they had previously selected. They found the following results:

- the thin disk population peaks at $[Fe/H] \sim 0.0$;
- the thick disk population peaks at $[Fe/H] \sim -0.4$;
- the halo population has a bimodal distribution with peaks at $[Fe/H] = -0.7$ and $[Fe/H] = -1.2$.

Since they found a large overlap between the thin disk and the thick disk populations, they also investigated the abundances of $\alpha$-elements, since thick disk stars tend to be more $\alpha$-enhanced than thin disk stars. They found that stars that they had previously kinematically selected and that also have metallicities and $\alpha$-elements abundances from the surveys above-mentioned follow the typical chemical trends that are expected on the basis of the Galactic component that they have been associated to: high metallicity ($[Fe/H] \sim 0$) and low $\alpha$-elements abundances ($[\alpha/Fe] \sim 0$) for thin disk stars, lower metallicity ($[Fe/H] \sim -0.4$) and larger $\alpha$-elements abundances ($[\alpha/Fe] \sim 0.2$) for thick disk stars and low metallicity ($[Fe/H] < -0.5$) for halo stars.

But how do their results compare to mine? Firstly, it is necessary to notice that I used metallicities from Gaia and RAVE. The Gaia spectroscopic instrument is a medium resolution spectrograph. This means that the metallicities extracted from Gaia spectra are less accurate than the ones obtained from high-resolution spectra, such as those coming from APOGEE and GALAH. The advantage of using Gaia metallicities is that they are present for most of PIC targets, thus allowing for a more complete investigation of their chemical properties. For a small part of LOPS2 targets I also used metallicities from RAVE, which are more accurate than Gaia metallicities. Let me now discuss how the results compare:

- regarding thin disk targets, I found, for both fields, that the peak of the distribution using Gaia data is at lower metallicities ($[Fe/H] \sim -0.3$ for LOPS2, $[Fe/H] \sim -0.2$ for LOPN1). When I compare the metallicity distribution using RAVE data,

however, we find very similar results, as the metallicity distribution using RAVE data has a peak at $[Fe/H] \sim -0.0$;

- regarding thick disk targets, I found, for both fields, a distribution with a peak at $[Fe/H] \sim -0.3$, so slightly less metal-poor than what is found by

  Boettner, Viswanathan, and Dayal. However, when it comes to the metallicity distribution obtained from RAVE data, I find that the peak is at $[Fe/H] \sim -0.0$, significantly higher than the results from Boettner, Viswanathan, and Dayal;

- regarding halo stars, I found that the metallicity distribution has a single peak at low metallicities: $[Fe/H] \sim -0.9$ for LOPS2, $[Fe/H] \sim -1.0$ for LOPN1. The metallicity distribution obtained from RAVE data, which are present for only 17 targets, shows a peak at $[Fe/H] \sim -0.5$. The metallicity distributions for halo targets I presented in this work differ from the ones from Boettner, Viswanathan, and Dayal as they have only one peak. The peak is located at metallicities which are in the middle with respect to the ones at which Boettner, Viswanathan, and Dayal found the two peaks.

The discrepancies in the results between the two studies can be explained by two factors. Firstly, the targets they analyzed come from the all-sky sample, while I studied only targets in LOPS2 and LOPN1. Secondly, as it has been already pointed out before, Gaia spectra are obtained from a medium resolution spectrograph, while APOGEE and GALAH spectra are obtained from high-resolution instruments.

### 5.6.3 Further insights from Boettner, Viswanathan, and Dayal (2024)

In their paper, Boettner, Viswanathan, and Dayal not only characterized the kinematics of PIC targets, but also provided further insights about the PLATO expected results. Using synthetic mock populations they made the following predictions:

- assuming a 2+2 years observing strategy for the LOPS2 and LOPN1 fields, they estimate that PLATO will find between 13 000 and 17 000 exoplanets, with more than 90% orbiting thin disk stars;

- although most of the discovered exoplanets will be Super-Earths and

  Sub-Neptunes, they expect PLATO to find between 20 and 130 Earth-like planets having orbital periods between 250 and 500 days;

- thin disk stars are expected to host a diverse range of exoplanets, while thick disk stars, being, on average, more metal-poor, are predicted to host a higher relative fraction of low-mass planets and a lower occurrence of giant planets;

- PLATO is expected to find about 400 exoplanets around the $\alpha$-enriched thick disk stars. This will allow to study the relation between the $\alpha$-abundances of host stars and the process of planet formation and the planetary diversity around this type of stars;
- they expect PLATO to find between 1 and 80 exoplanets orbiting around halo stars with $[Fe/H] < -0.3$ and hundreds of exoplanets orbiting around thin disk, thick disk and halo stars with $[Fe/H] < -0.6$. These observations will help in understanding if there is a minimum metallicity threshold for planet formation;
- they identified 47 targets kinematically classified as halo stars in the P1 sample across LOPS2 and LOPN1 that would be targets of prime interest in the search for planets orbiting low-metallicity stars.

# Chapter 6

# Stellar properties of PIC targets

In this chapter I analyze the stellar properties (such as effective temperature, mass, radius) and other parameters (such as distance) of the PIC targets.

## 6.1 LOPS2 stellar properties

I want to study the stellar properties of the targets in LOPS2. In particular, I want to investigate how these change among the different stellar populations.

### 6.1.1 Mass distribution

I start by investigating the mass distribution in terms of the various populations. Out of the 174 334 targets in the LOPS2 Toomre diagram, 174 095 are associated to a mass value in the PIC. The mass distribution is shown in Fig. 6.1.

The mean mass is $M_{mean} = 1.17$ M$_\odot$, the median mass is $M_{median} = 1.20$ M$_\odot$. The mean and median masses for each stellar population are:

- likely thin disk targets (127 472 targets): $M_{mean} = 1.17$ M$_\odot$, $M_{median} = 1.21$ M$_\odot$;
- likely thick disk targets (46 007 targets): $M_{mean} = 1.17$ M$_\odot$, $M_{median} = 1.19$ M$_\odot$;
- likely halo targets (590 targets): $M_{mean} = 1.14$ M$_\odot$, $M_{median} = 1.15$ M$_\odot$;
- extreme Toomre component targets (23 targets): $M_{mean} = 1.18$ M$_\odot$, $M_{median} = 1.10$ M$_\odot$;
- extreme retrograde motion targets (3 targets): $M_{mean} = 1.02$ M$_\odot$, $M_{median} = 0.99$ M$_\odot$.

It looks like there is no particular difference in terms of stellar mass among the different populations.

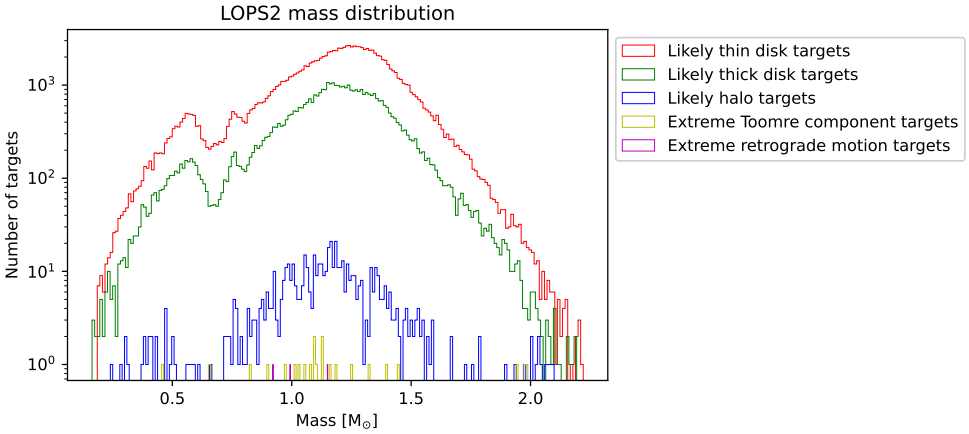


Figure 6.1: Mass distribution for LOPS2. The vertical axis is in logarithmic scale in order to make the differences between the groups appreciable.

### 6.1.2 Radius distribution

I investigate the radius distribution for the various populations. Out of the 174 334 targets in the LOPS2 Toomre diagram, 174 012 are associated to a radius value in the PIC. The radius distribution is shown in Fig. 6.2.

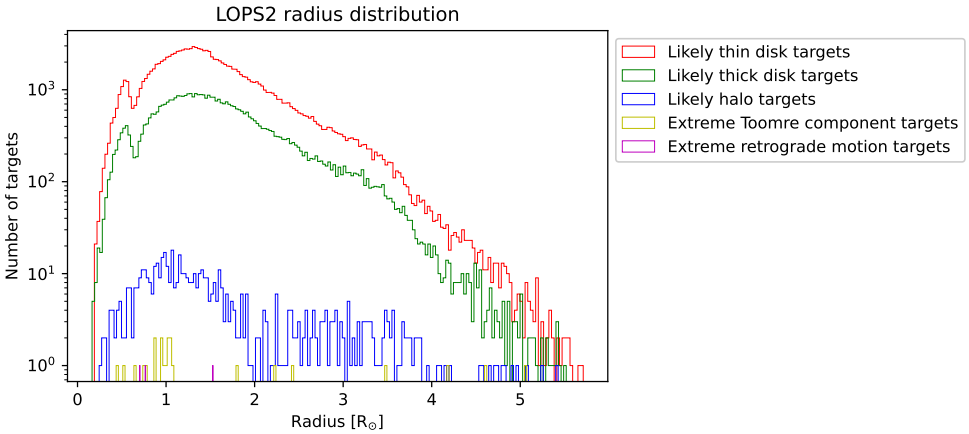


Figure 6.2: Radius distribution for LOPS2. The vertical axis is in logarithmic scale, in order to make the differences between the groups appreciable.

The mean radius is $R_{mean} = 1.55$ R$_\odot$, the median radius is $R_{median} = 1.42$ R$_\odot$. The mean and median radii for each stellar population are:

- likely thin disk targets (127 397 targets): $R_{mean} = 1.55$ R$_\odot$, $R_{median} = 1.42$ R$_\odot$;

- likely thick disk targets (45 996 targets): $R_{mean} = 1.62$ R$_\odot$, $R_{median} = 1.49$ R$_\odot$;
- likely halo targets (593 targets): $R_{mean} = 1.66$ R$_\odot$, $R_{median} = 1.32$ R$_\odot$;
- extreme Toomre component targets (23 targets): $R_{mean} = 1.65$ R$_\odot$, $R_{median} = 1.02$ R$_\odot$;
- extreme retrograde motion targets (3 targets): $R_{mean} = 1.00$ R$_\odot$, $R_{median} = 0.77$ R$_\odot$.

Similarly to what was found investigating the mass distribution, and not surprisingly given that discovery, I notice no particular difference among the different populations. Extreme retrograde motion targets are characterized by smaller radii with respect to the other groups. This is expected, since their mean mass also appeared slightly inferior to the values of the other populations. Their low number, however, is such that this behaviour is not relevant.

### 6.1.3 Effective temperature

I investigate the effective temperature distribution for the various populations. All the 174 334 targets in the LOPS2 Toomre diagram are associated to an effective temperature value in the PIC. The effective temperature distribution is shown in Fig. 6.3.

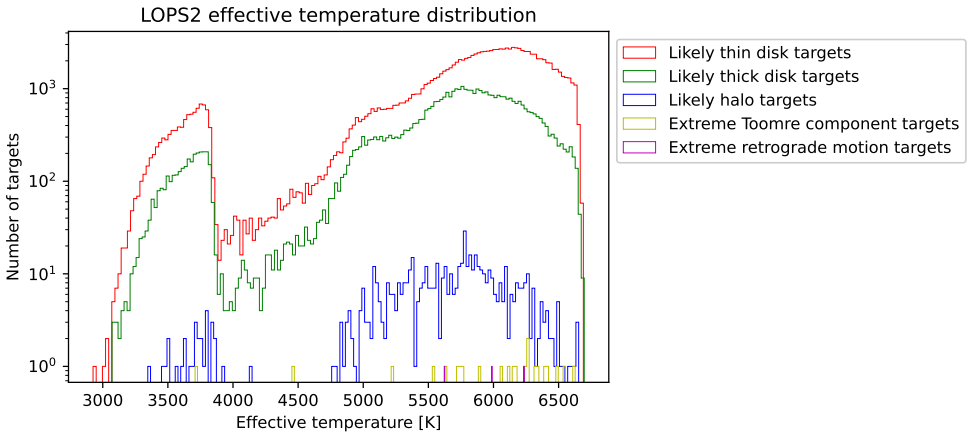


Figure 6.3: Effective temperature distribution for LOPS2. The vertical axis is in logarithmic scale, in order to make the differences between the groups appreciable.

The mean effective temperature is $T_{eff-mean} = 5723$ K, the median effective temperature is $T_{eff-median} = 5896$ K. The mean and median effective temperatures for each stellar population are:

- likely thin disk targets (127 642 targets): $T_{eff-mean} = 5751$ K, $T_{eff-median} = 5942$ K;
- likely thick disk targets (46 071 targets): $T_{eff-mean} = 5646$ K, $T_{eff-median} = 5782$ K;
- likely halo targets (595 targets): $T_{eff-mean} = 5606$ K, $T_{eff-median} = 5736$ K;
- extreme Toomre component targets (23 targets): $T_{eff-mean} = 5917$ K, $T_{eff-median} = 6154$ K;
- extreme retrograde motion targets (3 targets): $T_{eff-mean} = 5948$ K, $T_{eff-median} = 5988$ K.

Once again, there is no particular difference among the various populations. The extreme targets seem to be characterized by higher effective temperatures, but it is necessary to take into account that their number is very small, therefore their mean values are not particularly significant.

### 6.1.4 Distance

I investigate the distance distribution for the various populations. All the 174 334 targets in the LOPS2 Toomre diagram are associated to a distance value in the PIC. The distance distribution is shown in Fig. 6.4.

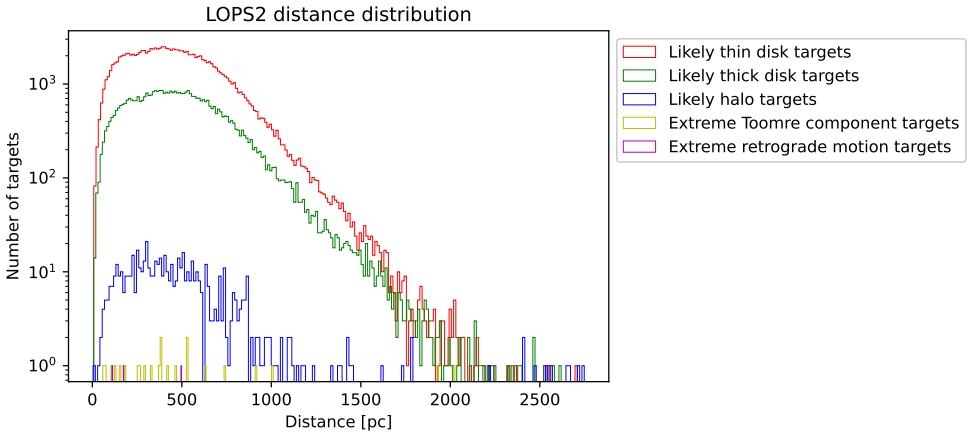


Figure 6.4: Distance distribution for LOPS2. The vertical axis is in logarithmic scale, in order to make the differences between the groups appreciable.

The mean distance is $D_{mean} = 482$ pc, the median distance is $D_{median} = 451$ pc. The mean and median distances for each stellar population are:

- likely thin disk targets (127 642 targets): $D_{mean} = 476$ pc, $D_{median} = 445$ pc;
- likely thick disk targets (46 071 targets): $D_{mean} = 500$ pc, $D_{median} = 468$ pc;
- likely halo targets (595 targets): $D_{mean} = 501$ pc, $D_{median} = 419$ pc;
- extreme Toomre component targets (23 targets): $D_{mean} = 530$ pc, $D_{median} = 381$ pc;
- extreme retrograde motion targets (3 targets): $D_{mean} = 260$ pc, $D_{median} = 173$ pc.

With the exception of the extreme retrograde motion targets, which, with respect to the other groups, are relatively close, the other groups have similar average and median distances. This is not surprising: PLATO samples are magnitude-limited and it was shown before that these groups also have similar mean radii and effective temperatures. This means that the magnitude cut acts in a similar way on the distances of the four groups.

### 6.1.5 Dereddened apparent magnitude in the Johnson Cousin V filter

I investigate the dereddened apparent magnitude in the Johnson Cousin V filter distribution for the various populations. All the 174 334 targets in the LOPS2 Toomre diagram are associated to a dereddened apparent magnitude in the Johnson Cousin V filter value in the PIC. The dereddened apparent magnitude in the Johnson Cousin V filter distribution is shown in Fig. 6.5.

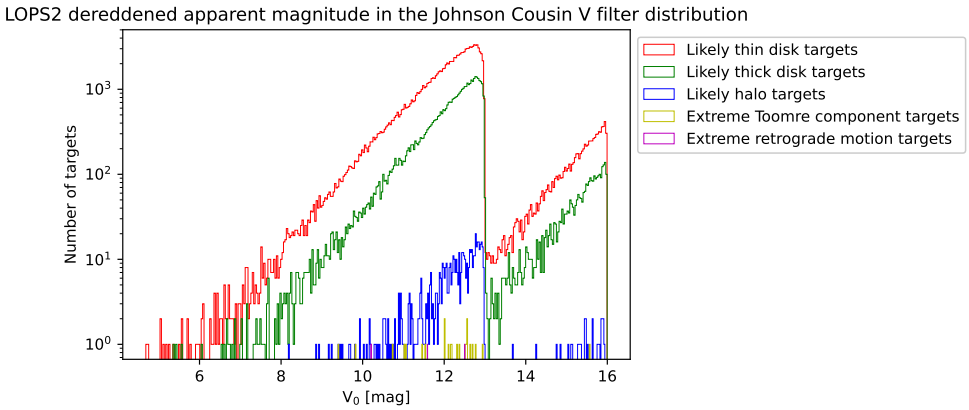


Figure 6.5: Dereddened apparent magnitude in the Johnson Cousin V filter distribution for LOPS2. The vertical axis is in logarithmic scale, in order to make the differences between the groups appreciable.

The mean dereddened apparent magnitude in the Johnson Cousin V filter is $V_{0-mean} = 12.27$ mag, the median dereddened apparent magnitude in the Johnson Cousin V filter is $V_{0-median} = 12.35$ mag. The mean and median dereddened apparent magnitudes in the Johnson Cousin V filter for each stellar population are:

- likely thin disk targets (127 642 targets): $V_{0-mean} = 12.24$ mag, $V_{0-median} = 12.31$ mag;
- likely thick disk targets (46 071 targets): $V_{0-mean} = 12.36$ mag, $V_{0-median} = 12.43$ mag;
- likely halo targets (595 targets): $V_{0-mean} = 12.33$ mag, $V_{0-median} = 12.43$ mag;
- extreme Toomre component targets (23 targets): $V_{0-mean} = 12.04$ mag, $V_{0-median} = 12.19$ mag;
- extreme retrograde motion targets (3 targets): $V_{0-mean} = 11.43$ mag, $V_{0-median} = 11.59$ mag.

The various populations display a similar behaviour in terms of the dereddened apparent magnitude in the Johnson Cousin V filter. The mean and median dereddened apparent magnitudes in the Johnson Cousin V filter of the extreme retrograde motion targets are quite brighter than the means and medians of such parameter for other groups. This could seem odd at first, since they are characterized by smaller masses and effective temperature; parameters that, for MS stars, would suggest a smaller luminosity. This trend is however easily explainable once the average distance of the extreme retrograde motion targets is taken into account: they are closer, on average, than the other groups of stars, therefore their apparent magnitude is brighter, despite the fact that they less luminous, as can be seen in Subsection 6.1.6, where I study the absolute intrinsic G magnitude of the targets.

### 6.1.6 Absolute intrinsic G magnitude

I investigate the absolute intrinsic G magnitude distribution for the various populations. All the 174 334 targets in the LOPS2 Toomre diagram are associated to an absolute intrinsic G magnitude value in the PIC. The absolute intrinsic G magnitude distribution is shown in Fig. 6.6.

The mean absolute intrinsic G magnitude is $M_{G_0-mean} = 4.05$ mag, the median absolute intrinsic G magnitude is $M_{G_0-median} = 3.67$ mag. The mean and median absolute intrinsic G magnitudes for each stellar population are:

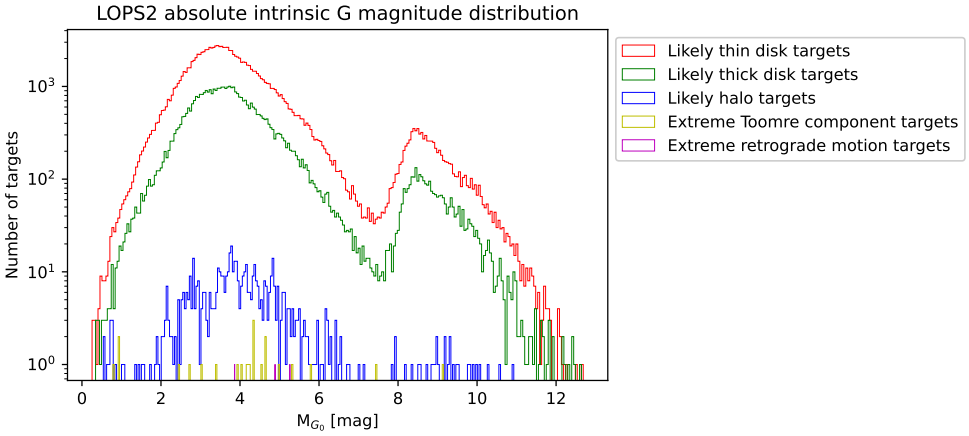


Figure 6.6: Absolute intrinsic G magnitude distribution for LOPS2. The vertical axis is in logarithmic scale, in order to make the differences between the groups appreciable.

- likely thin disk targets (127 642 targets): $M_{G_0-mean} = 4.06$ mag, $M_{G_0-median} = 3.66$ mag;
- likely thick disk targets (46 071 targets): $M_{G_0-mean} = 4.05$ mag, $M_{G_0-median} = 3.71$ mag;
- likely halo targets (595 targets): $M_{G_0-mean} = 4.15$ mag, $M_{G_0-median} = 3.90$ mag;
- extreme Toomre component targets (23 targets): $M_{G_0-mean} = 4.10$ mag, $M_{G_0-median} = 4.24$ mag;
- extreme retrograde motion targets (3 targets): $M_{G_0-mean} = 4.67$ mag, $M_{G_0-median} = 4.89$ mag.

There is no relevant difference among the different populations in terms of the absolute intrinsic G magnitude. I notice that the extreme retrograde motion targets are, on average, less luminous than the other groups. This is not surprising, since I found before that, with respect to the other groups, they have a smaller mean radius and a smaller mean effective temperature.

### 6.1.7 Dereddened color $(BP - RP)_0$

I investigate the dereddened color $(BP - RP)_0$ distribution. The color is obtained from the magnitudes in the blue photometer (BP) and red photometer (RP) of the Gaia photometric instrument. All the 174 334 targets in the LOPS2 Toomre diagram are associated

to a dereddened color $(BP-RP)_0$ value in the PIC. The dereddened color $(BP-RP)_0$ distribution is shown in Fig. 6.7.

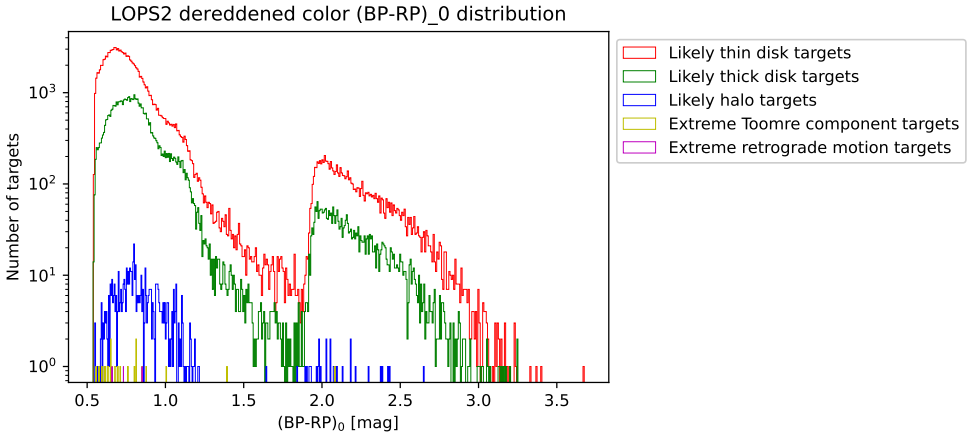


Figure 6.7: Dereddened color $(BP-RP)_0$ distribution for LOPS2. The vertical axis is in logarithmic scale, in order to make the differences between the groups appreciable.

The mean dereddened color $(BP-RP)_0$ is $(BP-RP)_{0-mean} = 0.88$ mag, the median dereddened color $(BP-RP)_0$ is $(BP-RP)_{0-median} = 0.76$ mag. The mean and median absolute intrinsic G magnitudes for each stellar population are:

- likely thin disk targets (127 642 targets): $(BP-RP)_{0-mean} = 0.87$ mag, $(BP-RP)_{0-median} = 0.75$ mag;
- likely thick disk targets (46 071 targets): $(BP-RP)_{0-mean} = 0.90$ mag, $(BP-RP)_{0-median} = 0.80$ mag;
- likely halo targets (595 targets): $(BP-RP)_{0-mean} = 0.90$ mag, $(BP-RP)_{0-median} = 0.81$ mag;
- extreme Toomre component targets (23 targets): $(BP-RP)_{0-mean} = 0.80$ mag, $(BP-RP)_{0-median} = 0.68$ mag;
- extreme retrograde motion targets (3 targets): $(BP-RP)_{0-mean} = 0.75$ mag, $(BP-RP)_{0-median} = 0.73$ mag.

There is no particular difference in the behaviour of the dereddened color $(BP-RP)_0$ among the different populations. It appears that, on average, extreme targets are bluer than the other groups.

### 6.1.8 Color-magnitude diagram

Let me consider now the color-magnitude diagram (CMD) of the targets in LOPS2. It is shown in Fig. 6.8.

Because of the scientific requirements, the targets form a Main Sequence. Disk stars span the whole plot in terms of both color and absolute magnitude. Halo targets tend to be concentrated on the left (bluer) side, although there are some stars also on the right (redder) side. Extreme targets are concentrated on the left side, with a couple of exceptions. In terms of their absolute magnitude, most of them are not particularly luminous, as I have already found before.

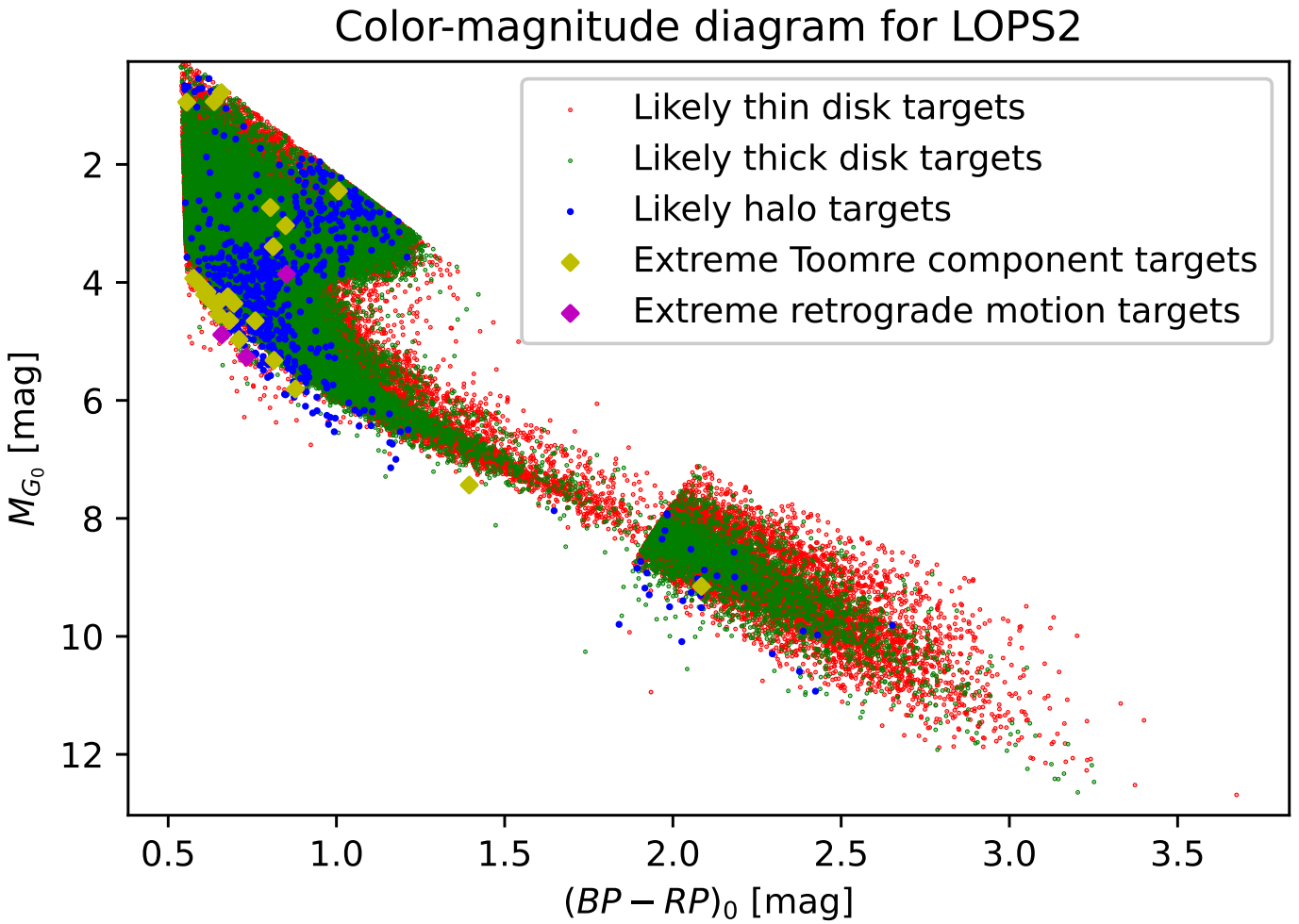


Figure 6.8: LOPS2 CMD.

## 6.2 LOPN1 stellar properties

I want to study the stellar properties of the targets in LOPN1. In particular, I want to investigate how these change among the different stellar populations.

### 6.2.1 Mass distribution

I start by investigating the mass distribution in terms of the various populations. Out of the 170 794 targets in the LOPS2 Toomre diagram, 170 626 are associated to a mass value in the PIC. The mass distribution is shown in Fig. 6.9.

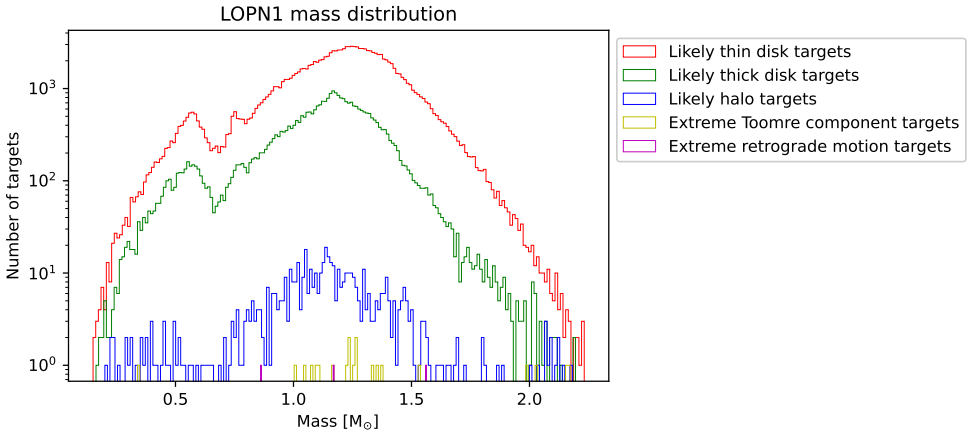


Figure 6.9: Mass distribution for LOPN1. The vertical axis is in logarithmic scale, in order to make the differences between the groups appreciable.

The mean mass is $M_{mean} = 1.17\ M_\odot$, the median mass is $M_{median} = 1.20\ M_\odot$. The mean and median masses for each stellar population are:

- likely thin disk targets (136 192 targets): $M_{mean} = 1.18\ M_\odot$, $M_{median} = 1.22\ M_\odot$;
- likely thick disk targets (33 862 targets): $M_{mean} = 1.11\ M_\odot$, $M_{median} = 1.15\ M_\odot$;
- likely halo targets (548 targets): $M_{mean} = 1.12\ M_\odot$, $M_{median} = 1.14\ M_\odot$;
- extreme Toomre component targets (21 targets): $M_{mean} = 1.35\ M_\odot$, $M_{median} = 1.25\ M_\odot$;
- extreme retrograde motion targets (3 targets): $M_{mean} = 1.20\ M_\odot$, $M_{median} = 1.17\ M_\odot$.

There is no particular difference among the three main populations. Extreme targets, instead, are characterized by larger mean masses, contrary to what happens for LOPS2.

### 6.2.2 Radius distribution

I investigate the radius distribution for the various populations. Out of the 170 794 targets in the LOPN1 Toomre diagram, 170 572 are associated to a radius value in the PIC. The radius distribution is shown in Fig. 6.10.

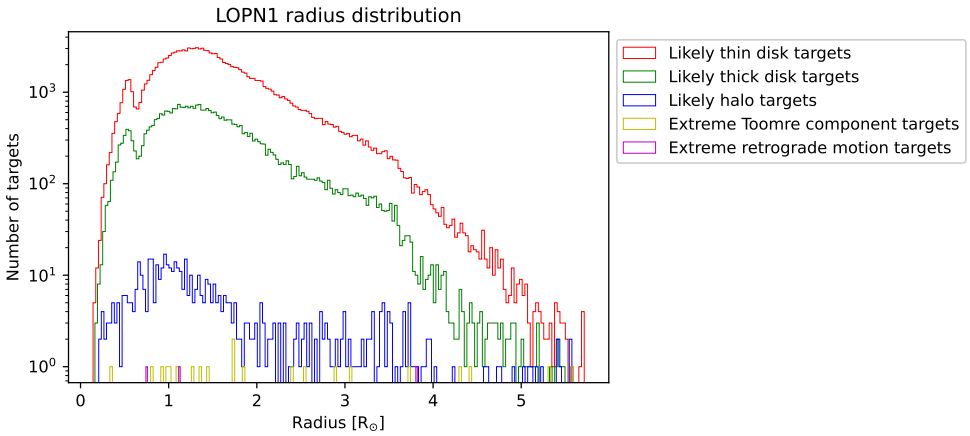


Figure 6.10: Radius distribution for LOPN1. The vertical axis is in logarithmic scale, in order to make the differences between the groups appreciable.

The mean radius is $R_{mean} = 1.56$ R$_\odot$, the median radius is $R_{median} = 1.42$ R$_\odot$. The mean and median radii for each stellar population are:

- likely thin disk targets (136 139 targets): $R_{mean} = 1.57$ R$_\odot$, $R_{median} = 1.43$ R$_\odot$;
- likely thick disk targets (33 858 targets): $R_{mean} = 1.51$ R$_\odot$, $R_{median} = 1.38$ R$_\odot$;
- likely halo targets (551 targets): $R_{mean} = 1.60$ R$_\odot$, $R_{median} = 1.21$ R$_\odot$;
- extreme Toomre component targets (21 targets): $R_{mean} = 2.32$ R$_\odot$, $R_{median} = 1.73$ R$_\odot$;
- extreme retrograde motion targets (3 targets): $R_{mean} = 1.89$ R$_\odot$, $R_{median} = 1.12$ R$_\odot$.

The three main populations have similar mean values for the radius, while extreme targets, similarly to what I found when studying the mass distribution, have larger mean values, but lower or comparable medians, suggesting that some extreme targets have particularly large radii.

### 6.2.3 Effective temperature

I investigate the effective temperature distribution for the various populations. All the 170 794 targets in the LOPN1 Toomre diagram are associated to an effective temperature value in the PIC. The effective temperature distribution is shown in Fig. 6.11.

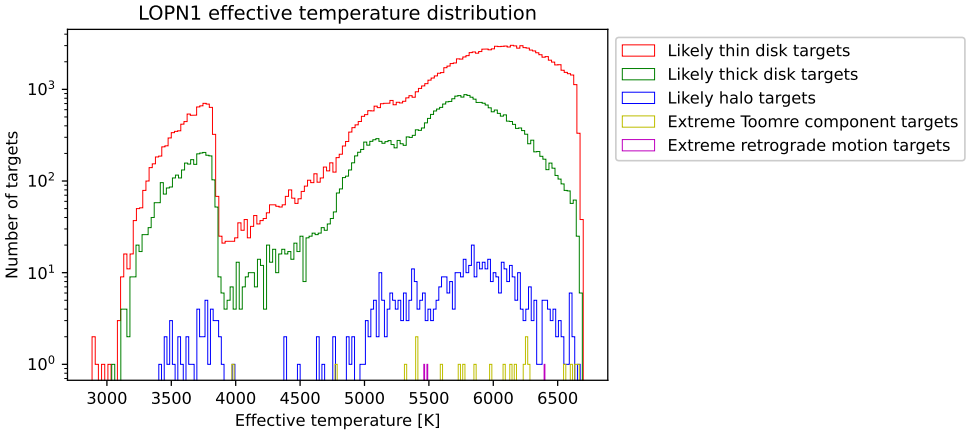


Figure 6.11: Effective temperature distribution for LOPN1. The vertical axis is in logarithmic scale, in order to make the differences between the groups appreciable.

The mean effective temperature is $T_{eff-mean} = 5724$ K, the median effective temperature is $T_{eff-median} = 5896$ K. The mean and median effective temperatures for each stellar population are:

- likely thin disk targets (136 324 targets): $T_{eff-mean} = 5773$ K, $T_{eff-median} = 5956$ K;
- likely thick disk targets (33 894 targets): $T_{eff-mean} = 5527$ K, $T_{eff-median} = 5707$ K;
- likely halo targets (552 targets): $T_{eff-mean} = 5621$ K, $T_{eff-median} = 5801$ K;
- extreme Toomre component targets (21 targets): $T_{eff-mean} = 5892$ K, $T_{eff-median} = 6085$ K;
- extreme retrograde motion targets (3 targets): $T_{eff-mean} = 5784$ K, $T_{eff-median} = 5489$ K.

There is no particular difference among the various populations. The extreme targets seem to be characterized by higher effective temperatures, but it is necessary to take into account that their number is very small, therefore their mean values are not particularly significant. However, given what was found about their mass, it is not surprising that they are associated to higher effective temperatures.

### 6.2.4 Distance

I investigate the distance distribution for the various populations. All the 170 794 targets in the LOPN1 Toomre diagram are associated to a distance value in the PIC. The distance distribution is shown in Fig. 6.12.

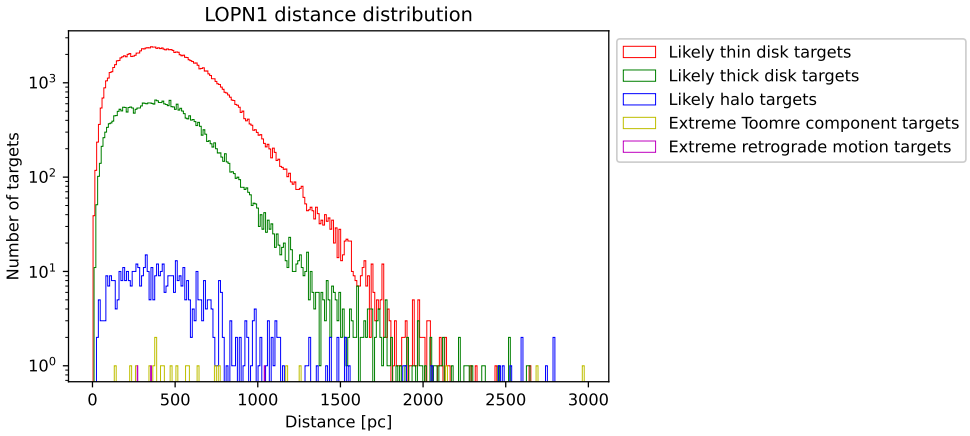


Figure 6.12: Distance distribution for LOPN1. The vertical axis is in logarithmic scale, in order to make the differences between the groups appreciable.

The mean distance is $D_{mean} = 464$ pc, the median distance is $D_{median} = 431$ pc. The mean and median distances for each stellar population are:

- likely thin disk targets (136 324 targets): $D_{mean} = 471$ pc, $D_{median} = 438$ pc;
- likely thick disk targets (33 894 targets): $D_{mean} = 436$ pc, $D_{median} = 409$ pc;
- likely halo targets (552 targets): $D_{mean} = 495$ pc, $D_{median} = 416$ pc;
- extreme Toomre component targets (21 targets): $D_{mean} = 832$ pc, $D_{median} = 513$ pc;
- extreme retrograde motion targets (3 targets): $D_{mean} = 556$ pc, $D_{median} = 355$ pc.

While the three main groups have comparable mean distances, extreme targets are characterized by larger mean distance.

### 6.2.5 Dereddened apparent magnitude in the Johnson Cousin V filter

I investigate the dereddened apparent magnitude in the Johnson Cousin V filter distribution for the various populations. All the 170 794 targets in the LOPN1 Toomre

diagram are associated to a dereddened apparent magnitude in the Johnson Cousin V filter value in the PIC. The dereddened apparent magnitude in the Johnson Cousin V filter distribution is shown in Fig. 6.13.

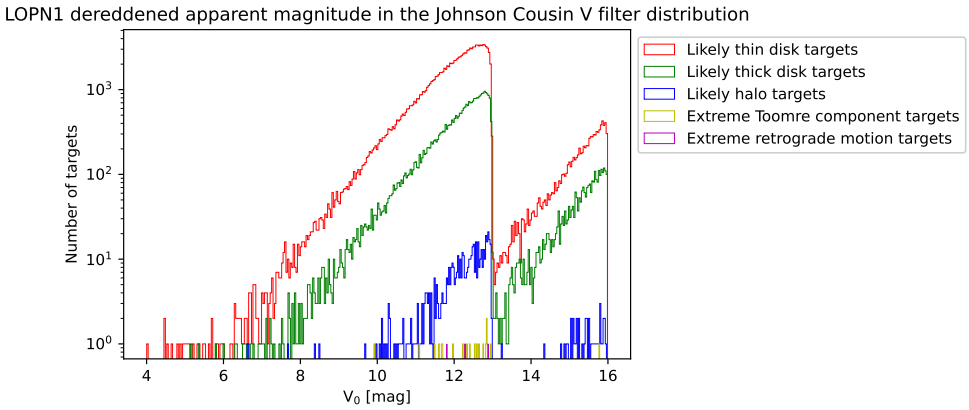


Figure 6.13: Dereddened apparent magnitude in the Johnson Cousin V filter distribution for LOPN1. The vertical axis is in logarithmic scale, in order to make the differences between the groups appreciable.

The mean dereddened apparent magnitude in the Johnson Cousin V filter is $V_{0-mean} = 12.22$ mag, the median dereddened apparent magnitude in the Johnson Cousin V filter is $V_{0-median} = 12.28$ mag. The mean and median dereddened apparent magnitudes in the Johnson Cousin V filter for each stellar population are:

- likely thin disk targets (136 324 targets): $V_{0-mean} = 12.18$ mag, $V_{0-median} = 12.24$ mag;
- likely thick disk targets (33 894 targets): $V_{0-mean} = 12.36$ mag, $V_{0-median} = 12.39$ mag;
- likely halo targets (552 targets): $V_{0-mean} = 12.43$ mag, $V_{0-median}12.45$ mag;
- extreme Toomre component targets (21 targets): $V_{0-mean} = 12.35$ mag, $V_{0-median} = 12.40$ mag;
- extreme retrograde motion targets (3 targets): $V_{0-mean} = 12.33$ mag, $V_{0-median} = 12.29$ mag.

The various populations display a similar behaviour in terms of the dereddened apparent magnitude in the Johnson Cousin V filter. The extreme targets show a mean

dereddened apparent magnitude in the Johnson Cousin V filter comparable to those of the other groups. This is not surprising: given their radius and effective temperature means, I expect them to be brighter, but, at the same time, I found out that, on average, they are also more distant. These two factors work out in such a way that the higher luminosity, which can be also noticed from the absolute intrinsic G magnitude shown in the next subsection, is compensated by the larger average distance, so that the mean dereddened apparent magnitude in the Johnson Cousin V filter in similar to the means of the other populations.

### 6.2.6 Absolute intrinsic G magnitude

I investigate the absolute intrinsic G magnitude distribution for the various populations. All the 170 794 targets in the LOPN1 Toomre diagram are associated to an absolute intrinsic G magnitude value in the PIC. The absolute intrinsic G magnitude distribution is shown in Fig. 6.14.

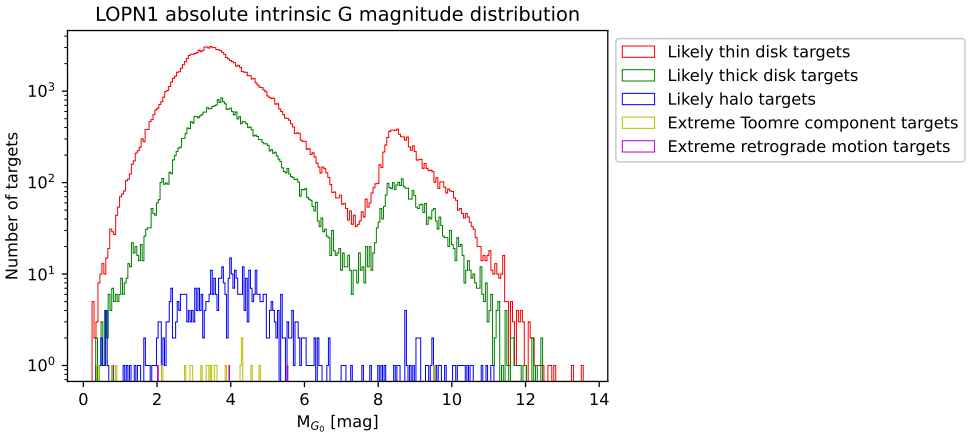


Figure 6.14: Absolute intrinsic G magnitude distribution for LOPN1. The vertical axis is in logarithmic scale, in order to make the differences between the groups appreciable.

The mean absolute intrinsic G magnitude is $M_{G_0-mean} = 4.07$ mag, the median absolute intrinsic G magnitude is $M_{G_0-median} = 3.69$ mag. The mean and median absolute intrinsic G magnitudes for each stellar population are:

- likely thin disk targets (136 324 targets): $M_{G_0-mean} = 4.01$ mag, $M_{G_0-median} = 3.63$ mag;
- likely thick disk targets (33 894 targets): $M_{G_0-mean} = 4.33$ mag, $M_{G_0-median} = 3.89$ mag;

- likely halo targets (552 targets): $M_{G_0-mean} = 4.32$ mag, $M_{G_0-median} = 4.04$ mag;
- extreme Toomre component targets (21 targets): $M_{G_0-mean} = 3.31$ mag, $M_{G_0-median} = 3.41$ mag;
- extreme retrograde motion targets (3 targets): $M_{G_0-mean} = 3.84$ mag, $M_{G_0-median} = 3.96$ mag.

I notice that likely thin disk stars are somewhat more luminous than likely thick disk and halo stars. Extreme targets are, on average, much more luminous. This is a consequence of their larger mean radius and higher mean effective temperature: luminosity increases with increasing radius and with increasing effective temperature.

### 6.2.7 Dereddened color $(BP - RP)_0$

I investigate the dereddened color $(BP - RP)_0$ distribution. The color is obtained from the magnitudes in the blue photometer (BP) and red photometer (RP) of the Gaia photometric instrument. All the 170 794 targets in the LOPN1 Toomre diagram are associated to a dereddened color $(BP - RP)_0$ value in the PIC. The dereddened color $(BP - RP)_0$ distribution is shown in Fig. 6.15.

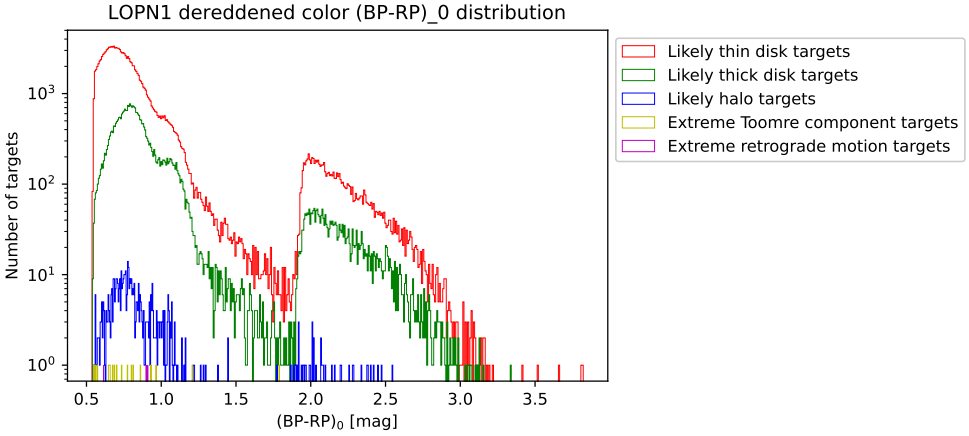


Figure 6.15: Dereddened color $(BP-RP)_0$ distribution for LOPN1. The vertical axis is in logarithmic scale, in order to make the differences between the groups appreciable.

The mean dereddened color $(BP-RP)_0$ is $(BP-RP)_{0-mean} = 0.88$ mag, the median dereddened color $(BP - RP)_0$ is $(BP - RP)_{0-median} = 0.76$ mag. The mean and median absolute intrinsic G magnitudes for each stellar population are:

- likely thin disk targets (136 324 targets): $(BP - RP)_{0-mean} = 0.86$ mag, $(BP - RP)_{0-median} = 0.74$ mag;

- likely thick disk targets (33 894 targets): $(BP-RP)_{0-mean} = 0.95$ mag, $(BP-RP)_{0-median} = 0.82$ mag;
- likely halo targets (552 targets): $(BP-RP)_{0-mean} = 0.91$ mag, $(BP-RP)_{0-median} = 0.79$ mag;
- extreme Toomre component targets (21 targets): $(BP-RP)_{0-mean} = 0.80$ mag, $(BP-RP)_{0-median} = 0.70$ mag;
- extreme retrograde motion targets (3 targets): $(BP-RP)_{0-mean} = 0.81$ mag, $(BP-RP)_{0-median} = 0.90$ mag.

There is no particular difference in the behaviour of the dereddened color $(BP-RP)_0$ among the different populations. I notice that, on average, extreme targets are bluer than the other targets.

### 6.2.8 Color-magnitude diagram

Let me consider now the color-magnitude diagram (CMD)of the targets in LOPN1. It is shown in Fig. 6.16.

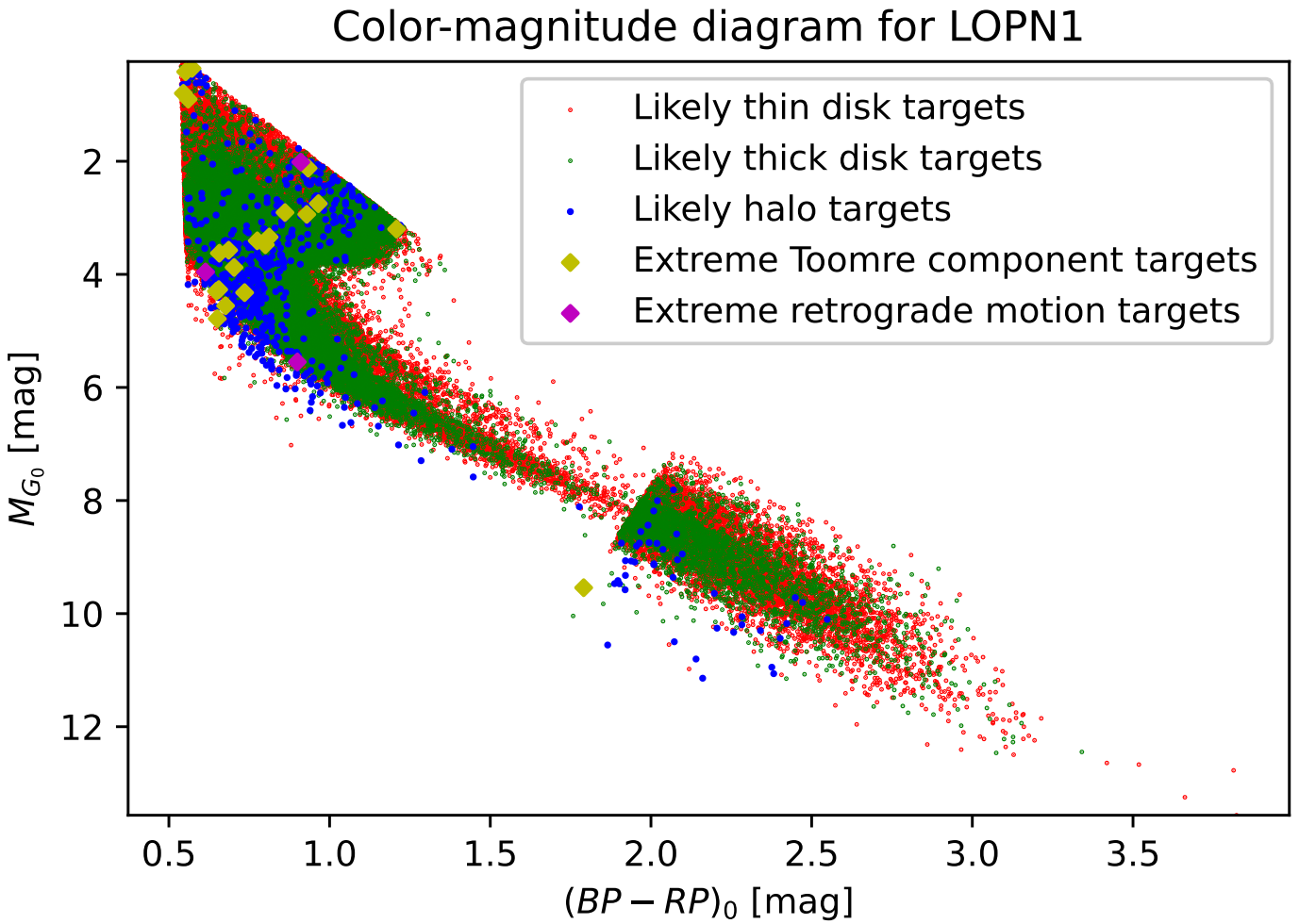


Figure 6.16: LOPN1 CMD.

The results are very similar to the ones I found for LOPS2. Because of the scientific requirements, the targets form a Main Sequence. Disk stars span the whole plot in terms of both color and absolute magnitude. Halo targets tend to be concentrated on the left (bluer) side, although there are some stars also on the right (redder) side. Extreme targets are concentrated on the left side, with a couple of exceptions. In terms of their absolute magnitude, while most of them are not particularly luminous, some of them are. Since extreme targets are very few, the fact that a small fraction of them have quite brighter absolute magnitudes (and therefore are more luminous) causes the trend that I observed before, namely that extreme targets seem to be characterized by a larger mean luminosity.

# Chapter 7

# Cross-matching the PIC with other relevant catalogues

In this chapter I show the results of the cross-matching of the PIC with other relevant catalogues, namely the TESS Objects of Interest (TOI) catalogue, the International Variable Star Index (VSX) catalogue and the open clusters catalogue of Hunt and Reffert (2023).

## 7.1 TOI catalogue

The TESS (Transiting Exoplanet Survey Satellite) mission (Ricker et al. 2014) is a NASA mission launched in 2018 and currently active whose main objective is the identification of planetary transits. It's an all-sky survey . There are 26 observation sectors with areas of $24° \times 96°$, each observed for 27 days. Moving towards the ecliptic poles, sectors overlap. This way, the region of the ecliptic poles (5% of the sky) is constantly observed for almost a year, allowing for the detection of exoplanets with large periods. TESS is expected to detect mostly short-period exoplanets (because of the observation strategy) at distances between 50 pc and 300 pc. TESS Objects of Interest (TOI) are routinely released. They include planet candidates, single transits of potential planet candidates and other timely astrophysical targets of opportunity. The TOI catalogue can be retrieved here. I performed the cross-matching between the PIC and the TOI catalogue by identifying stars which, when comparing their positions in the two catalogues, had separations less than 1 arcsec. PIC positions are those obtained from Gaia and are referred to Epoch 2016, while the TOI catalogue positions are referred to Epoch 2015.5. It is important to notice that such cross-matching was made using all TOI candidates, not only confirmed planets. This means that some cross-matches may be referred to false positives and only a one-by-one analysis could solve this ambiguity. Let me consider the cross-matching results for the two fields of PLATO.

### 7.1.1 LOPS2-TOI catalogue cross-matching

I find that 371 targets of the PIC cross-match with the TOI catalogue in LOPS2. Of these 371, 352 are also associated to a measurement of radial velocity from Gaia and so are represented in the LOPS2 Toomre diagram. 251 of the 347 targets are likely thin disk targets, while the remaining 101 are likely thick disk targets. There are no targets associated to the halo. This is not surprising: I found before that about 0.3% of LOPS2 targets are associated to the halo; if the distribution of stars observed by TESS behaves similarly to the one observed in LOPS2, then one would expect 1 target out of the 347 to be associated to the halo. Such prediction is compatible with the result that no cross-matched target appears to belong to the halo.

Out of the 352 targets, 18 are associated to known planets (label "KP" in the column "TOI disposition " in the TOI catalogue) and 36 are associated to confirmed planets (label "CP" in the column "TOI disposition" in the TOI catalogue). In Fig. 7.1 the Toomre diagram for these 347 targets is shown.

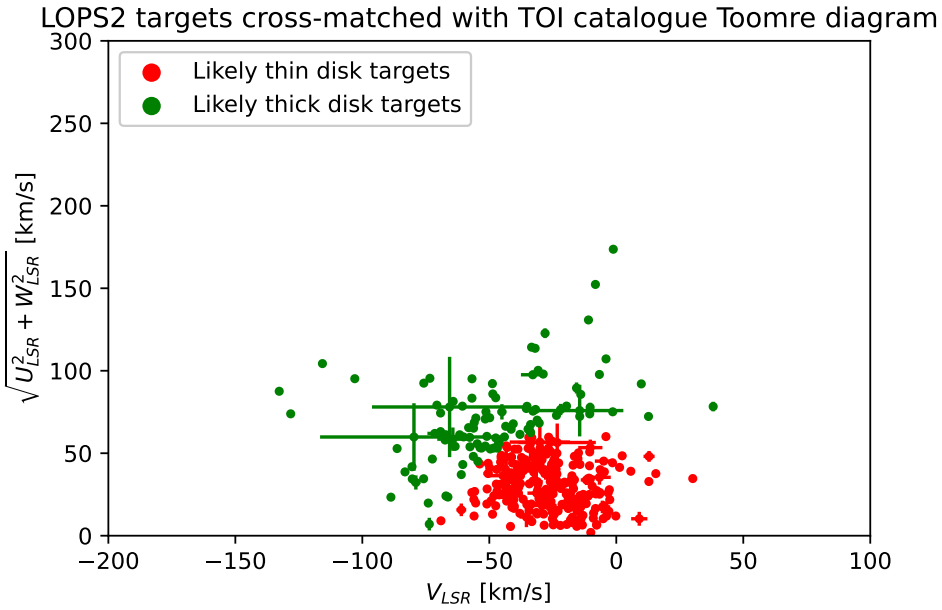


Figure 7.1: Toomre diagram for LOPS2 targets cross-matched with the TOI catalogue.

### 7.1.2 LOPN1-TOI catalogue cross-matching

I find that 409 targets of the PIC cross-match with the TOI catalogue in LOPN1. Of these 402, 392 are present in the LOPN1 Toomre diagram. 321 out of the 385 targets are likely thin disk targets, while the remaining 71 are likely thick disk targets. Once

again, no target is associated to the halo. As explained in the previous subsection, this is not surprising. As a matter of fact, following the same reasoning presented in the previous subsection, one would expect 1 cross-matched target to belong to the halo. Such prediction is compatible with the result of no targets associated to the halo.

Out of the 392 targets, 46 are associated to known planets and 35 are associated to confirmed planets. In Fig. 7.2 the Toomre diagram for these 385 targets is shown.

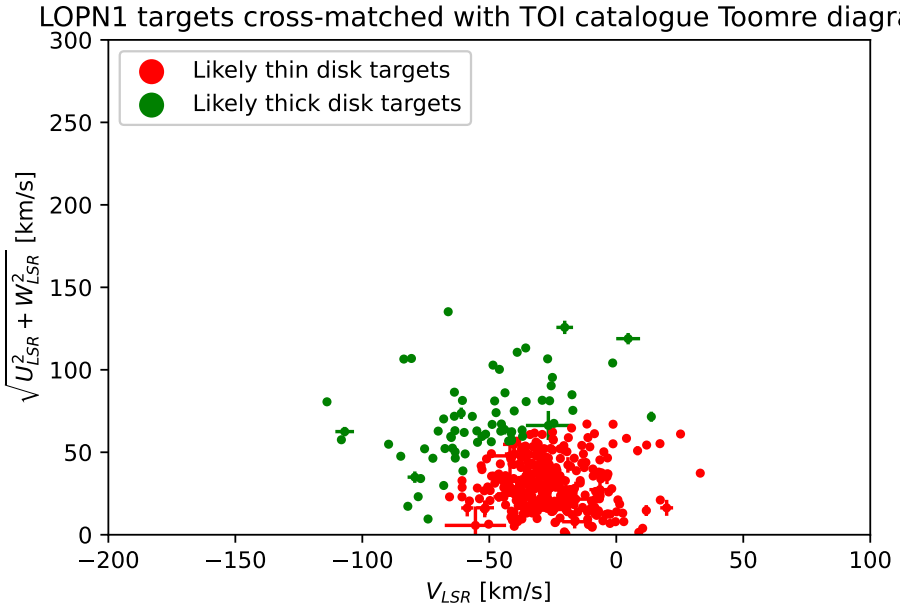


Figure 7.2: Toomre diagram for LOPN1 targets cross-matched with the TOI catalogue.

## 7.2 VSX catalogue

The International Variable Star Index, or VSX (Watson, Henden, and Price 2006), is a comprehensive relational database of known and suspected variable stars gathered from respected published sources and made available through a Web interface. I cross-matched the PIC with VSX. The targets of the latter have positions referred to Epoch 2000.

### 7.2.1 LOPS2-VSX catalogue cross-matching

I find that 2 364 LOPS2 targets cross-match with VSX. Of these, 2 020 are represented in the LOPS2 Toomre diagram. In terms of their stellar populations:

- likely thin disk targets: 1 606;
- likely thick disk targets: 400;
- likely halo targets: 11;
- extreme Toomre component targets: 3.

In Fig. 7.3 the Toomre diagram for the 2 020 targets is shown.

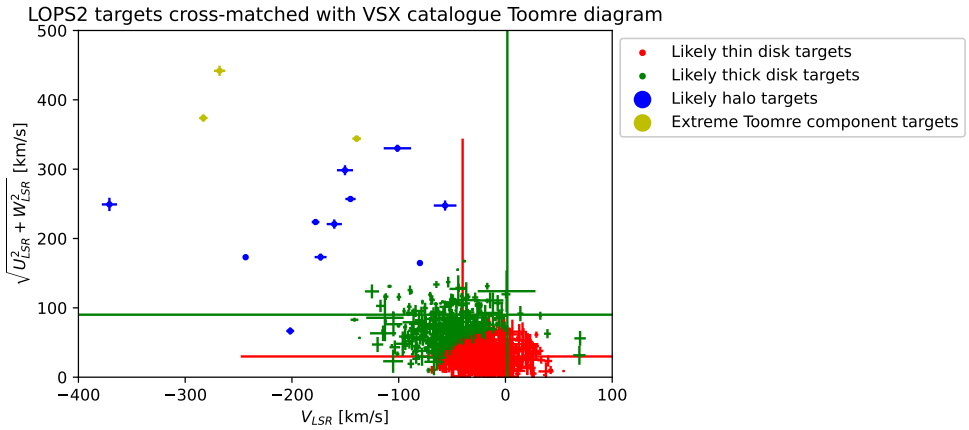


Figure 7.3: Toomre diagram for LOPS2 targets cross-matched with the VSX catalogue.

The VSX catalogue specifies the variability type of the stars it contains (column "Type" in the VSX catalogue). It is interesting to investigate the variability types of likely halo and extreme targets.

Regarding the likely halo targets, 8 are classified as RR-Lyrae variables with asymmetric light curves (Type = "RRAB"), 1 is a variable of an unspecified type (Type =

"VAR"), 1 is a spotted star that is not classified into a particular class (Type = "ROT") and 1 is a double-mode RR Lyrae star which pulsates in the fundamental mode as well as in the first overtone with a period ratio of 0.74 and a fundamental period near 0.5 days (Type = "RRD").

Regarding the extreme targets, 1 is a RR-Lyrae variable showing the Blazhko effect (Type = "RRAB/BL") while the other 2 are RR-Lyrae variables with asymmetric light curves (Type = "RRAB").

### 7.2.2 LOPN1-VSX catalogue cross-matching

I find that 5 385 LOPN1 targets cross-match with VSX. Of these, 5 000 are represented in the LOPN1 Toomre diagram. In terms of their stellar populations:

- likely thin disk targets: 4 438;
- likely thick disk targets: 543;
- likely halo targets: 15;
- extreme Toomre component targets: 4.

In Fig. 7.4 Toomre diagram for the 5 000 targets is shown.

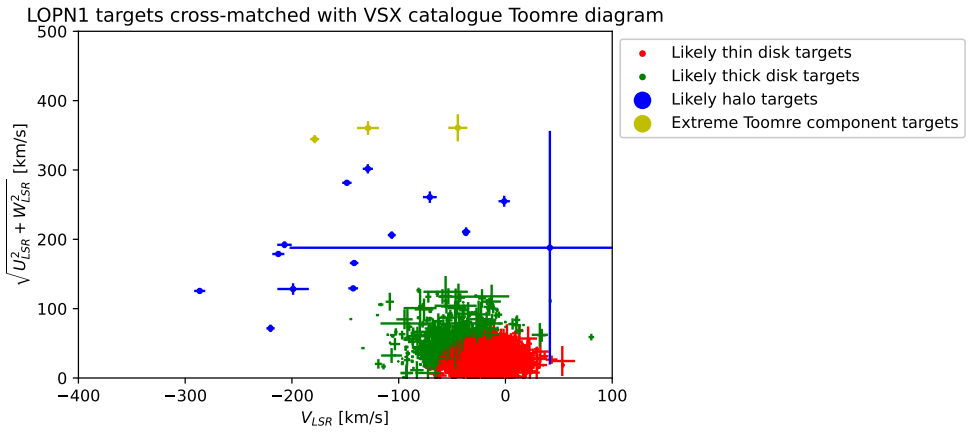


Figure 7.4: Toomre diagram for LOPN1 targets cross-matched with the VSX catalogue.

Similarly to what was done for LOPS2, I investigate the variability types of likely halo and extreme targets.

Regarding the likely halo targets, 10 targets are classified as RR-Lyrae variables with asymmetric light curves (Type = "RRAB"), 2 targets are classified as RR-Lyrae variables showing the Blazhko effect (Type = "RRAB/BL"), 1 is a $\beta$ Lyrae-type eclipsing system (Type = "EB"), 1 target is not clearly classified and is either a $\beta$ Persei-type eclipsing system or as $\beta$ Lyrae-type eclipsing binary (Type = "EA|EB") and 1 target is classified as a RS Canum Venaticorum-type binary system (Type = "RS").

Regarding the extreme targets, 2 of them are classified as RR-Lyrae variables showing the Blazhko effect (Type = "RRAB/BL") and the other 2 as RR-Lyrae variables with asymmetric light curves (Type = "RRAB").

It is important to notice that among likely halo stars there are 2 systems of eclipsing binaries. These stars are particularly interesting, as their light curves may originate a

false-positive signal in transit searches for exoplanets. Furthermore, it is not possible to exclude that these stars may be contaminants, as their binary nature may affect, even drastically, the estimation of their stellar parameters. For these reasons, it is worth to identify them clearly:

- the $\beta$ Lyrae-type eclipsing system (Type = "EB") has the Gaia identifier Gaia DR3 2158239006320505088;
- the eclipsing binary system whose classification is uncertain

  (Type = "EA|EB") is ATO J242.9412+58.6361 which has as Gaia identifier Gaia DR3 1623153288886262400.

## 7.3 Open clusters catalogue

I cross-match the PIC with the open clusters catalogue of Hunt and Reffert (2023). In their work, using Gaia DR3 data, they produced the most reliable and complete census of stellar clusters in circulation. In total, their catalogue contains 7 167 clusters.

2 065 targets of the PIC cross-match with the open clusters catalogue: 1 568 belong to LOPS2, 497 belong to LOPN1. If I consider only targets for which there is a Gaia radial velocity measurement, and that therefore appear in the Toomre diagrams presented in the previous sections, I find a total of 1 952 PIC targets that cross-match with the open clusters catalogue, of which 1 479 belong to LOPS2 and 473 belong to LOPN1.

In Fig. 7.5 I show the all-sky Aitoff projection representing all the targets in LOPS2 and LOPN1 that cross-match with the open clusters catalogue.

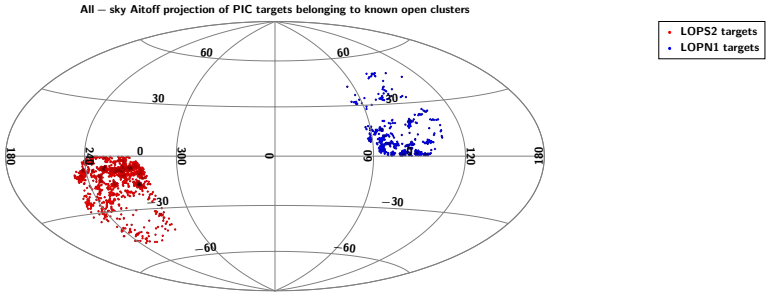


Figure 7.5: All-sky Aitoff projection in Galactic coordinates of PIC targets that cross-match with the open clusters catalogue.

Let me investigate each field in more detail.

### 7.3.1 LOPS2-open clusters catalogue cross-matching

LOPS2 targets cross-match with 160 known open clusters. The cluster containing the larger fraction of LOPS2 targets is NGC 2516, which contains 208 targets. 1 455 targets are likely to belong to the thin disk, while 24 targets are likely to belong to the thick disk. No targets are likely to belong to the halo. This result is expected, as open clusters are typically associated to the Galactic disk. It is interesting to notice that the 24 likely thick disk targets belong to open clusters where the majority of stars are classified as likely thin disk targets. One would expect that all the stars which belong to a given open cluster are associated to the same stellar component. This may suggest either that such likely thick disk targets have been wrongly associated to the open clusters in question or, more likely, that they have been wrongly classified as belonging to the thick disk. If the latter is the case, than this could lead to an estimation of the fraction of thin disk targets that, as a consequence of the classification approach adopted in this work, have been wrongly classified as likely thick disk targets. Such fraction would be of order 1.6 %. Now, having discussed all of this, it is important to remember that the real nature of the subdivision of the Galactic disk into two different components is still a matter of study (and debate) and that the criteria adopted to divide the targets in terms of the stellar component of the Milky Way are somewhat "rough", as already discussed in Section 5.6.1. It is therefore expected that a fraction of the targets may be characterized by a rather uncertain classification.

In Fig. 7.6 I show the sinusoidal sky projection for LOPS2 targets that cross-match with the open clusters catalogue.

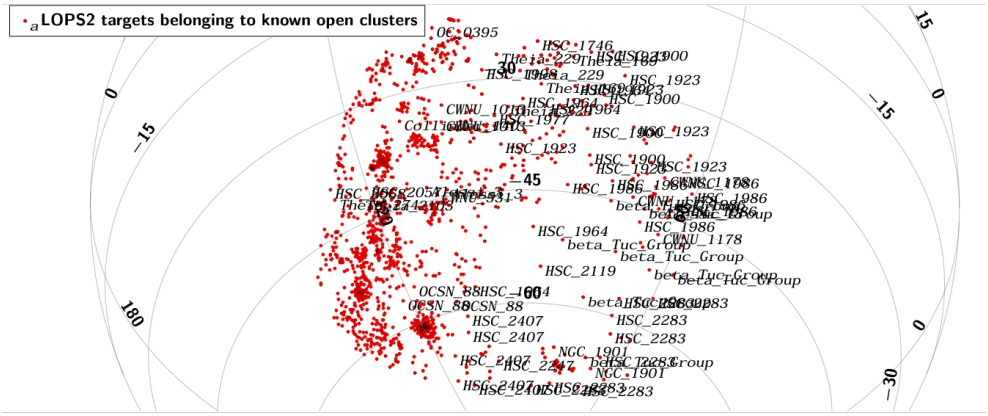


Figure 7.6: Sinusoidal projection of LOPS2 targets that cross-match with the open clusters catalogue. Only a handful of open clusters are labelled on the plot, because of obvious crowding problems.

### 7.3.2 LOPN1-open clusters catalogue cross-matching

LOPN1 targets cross-match with 83 known open clusters. The cluster containing the larger fraction of LOPN1 targets is Roslund 6, which contains 32 targets. Out of the 473 cross-matched targets, 470 are likely to belong to the thin disk and 3 are likely to belong to the thick disk. Given that also in this case the likely thick disk targets belong to open clusters which are dominated by likely thin disk targets and following the reasoning presented in the previous subsection, one would infer a fraction of targets wrongly classified as likely to belong to the thick disk of order 0.6 %. In Fig. 7.7 I show the sinusoidal sky projection for LOPN1 targets that cross-match with the open clusters catalogue.

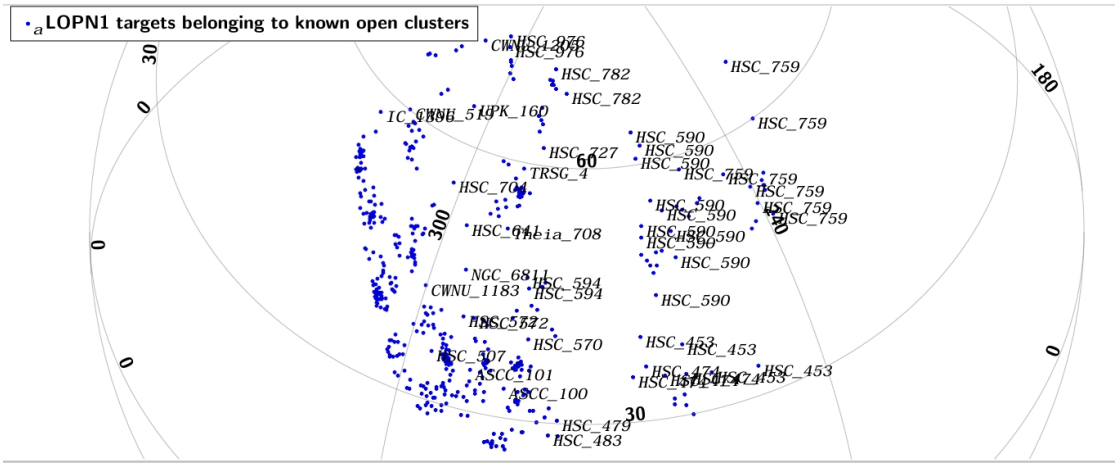


Figure 7.7: Sinusoidal projection of LOPN1 targets that cross-match with the open clusters catalogue. Only a handful of open clusters are labelled on the plot, because of obvious crowding problems.

# Chapter 8

# Conclusions

PLATO, whose launch is rapidly approaching, is expected to discover large numbers of Earth analogs. Furthermore, it will provide key insights into complex phenomena such as planetary formation and planetary evolution. Its results will be able to significantly boost our knowledge of exoplanetary science. In order to assure that the mission will be able to provide the maximum scientific output, a preliminary analysis of the targets is required. In this work I have focused on the kinematics of PLATO targets, aiming at classifying them in terms of the stellar component of the Galaxy that they belong to. To achieve this goal, I exploited Gaia data and, by assessing their kinematic properties, I found that most of the targets in both LOPS2 and LOPN1 belong to the disk populations. In particular, in both cases I found that about 75-80% of the targets belong to the thin disk, about 20% of the targets belong to the thick disk and the remaining targets, about 0.3% of the total, belong to the halo. I also noticed that some targets present peculiar kinematic properties: 6 targets are characterized by rather pronounced retrograde motions, while 44 targets are characterized by a particularly large Toomre component, suggesting that they are rapidly moving away from or moving towards the Galactic plane. In order to confirm the kinematic analysis, I studied the metallicity distributions for targets in both fields, using measurements from Gaia and RAVE. I found that halo-associated targets are, on average, more metal-poor than disk-associated targets. The mean value depends on whether one considers Gaia data or RAVE data, but, in both cases, I found that the mean metallicity of likely halo targets is about five dex smaller than the mean metallicity of likely disk stars, a result which is consistent with previous studies of the Milky Way.

Successively, I showed and analyzed the stellar properties, such as radius, mass and effective temperature, of targets in both fields. I found that, among the three main kinematic groups that I had identified, there are no considerable differences. However, this was just a brief and preliminary analysis using only the data in the PIC: further studies, also employing estimates from different catalogues, would be useful.

Finally, I cross-matched the PIC with other relevant catalogues, such as the TESS

Objects of Interest (TOI) catalogue, the VSX catalogue, which is perhaps the most important catalogue of variable objects, and an open clusters catalogue recently created using Gaia data. I found that almost 800 targets cross-match with the TOI catalogue, almost 8 000 targets cross-match with the VSX catalogue and that a little more than 2 000 targets are contained in 243 open clusters.

Clearly, the investigation presented in this work can and should be expanded. For example, it would be useful to provide a deeper analysis of the stellar properties of the targets in terms of their stellar components, as explained above. This would provide a systematic characterization of the targets in the context of our Galaxy, necessary for the subsequent interpretation of the mission results. Another very interesting and potentially useful evolution of this work would be an extensive metallicity investigation of the targets, which would allow to obtain more precise stellar parameters for the PIC targets. A better determination of stellar parameters would help in the identification of false alarms as well as in the determination of the parameters and properties of the exoplanets.

# Appendix A

# Searching for exoplanets: the radial velocity and the transit methods

Detecting exoplanets is now a common event, with more than 5 000 exoplanets already confirmed. The two most effective methods to detect them, both crucial in then context of the PLATO mission, are the radial velocity method and the transit method. In this appendix we illustrate these two techniques to look for exoplanets.

## A.1 The radial velocity method

The radial velocity method has been a fundamental detection technique in the history of exoplanetary science, leading to the discovery of the first exoplanet orbiting a MS star ever detected: Pegasi 51 b (Mayor and Queloz 1995). The theoretical foundation of this method is rather straight-forward: given a star and a planetary system around such star, we know that the star and the planets orbit around a common barycenter. Considering a simple planetary system with one star and one planet, it can be easily shown, starting from Kepler's laws, that the motion of the star, which takes the name of "reflex motion", is described by:

$$a_\star = a_p \frac{M_p}{M_\star} \tag{A.1}$$

where $a_\star$ is the semimajor axis of the orbit of the star around the common barycenter, $a_p$ is the semimajor axis of the orbit of the planet around the common barycenter, $M_p$ is the mass of the planet and $M_\star$ is the mass of the star.

It is possible to build stellar radial velocity curves, which represent how the stellar radial velocity evolves as a function of time. It is possible to show that the stellar velocity due to the reflex motion is given by:

$$K = \left(\frac{2\pi G}{P}\right)^{1/3} \frac{M_p \sin(i)}{(M_\star + M_p)^{2/3}} \frac{1}{(1-e^2)^{1/2}} \tag{A.2}$$

where K is semi-amplitude of the radial velocity (the variation of $V_\star \sin(i)$, during the orbital period), P is the orbital period of the planet, i is the inclination and e is the eccentricity of the planetary orbit. From an observational perspective, this method is based on a spectroscopic measurement. We measure the radial velocity of a star at various epochs. Since the star is moving, the light that it emits is affected by the Doppler effect. As a consequence, we observe a periodic shift of the photospheric lines in the stellar spectrum. Now, it must be clear that we are considering very small effects. To give some numbers, Earth, which has a mass of about $3 \times 10^{-3}$ $M_J$, where $M_J$ is the mass of Jupiter, produces an effect on the Sun of 0.0089 m s$^{-1}$. Jupiter produces an effect on the Sun of 12.4 m s$^{-1}$. For this reason, high resolution spectroscopy with long term stability is required to detect exoplanets with the radial velocity method, particularly if we want to detect small, Earth-sized exoplanets, which is the main objective of the PLATO mission. HARPS-N, installed at the Telescopio Nazionale Galileo (TNG), is able to measure radial velocities at the level of 40 cm s$^{-1}$. EXPRESSO, a spectograph mounted on the Very Large Telescope (VLT), is now able to detect radial velocities at the level of 10 cm s$^{-1}$, at the edge of the signal produced by an Earth-like planet around a Sun-like star. The radial velocity method can produce false-positives, mainly due to stellar activity mimicking planetary signals, but it is much more reliable than other techniques, such as the transit method. In any case, there are observational tools to mitigate this problem.

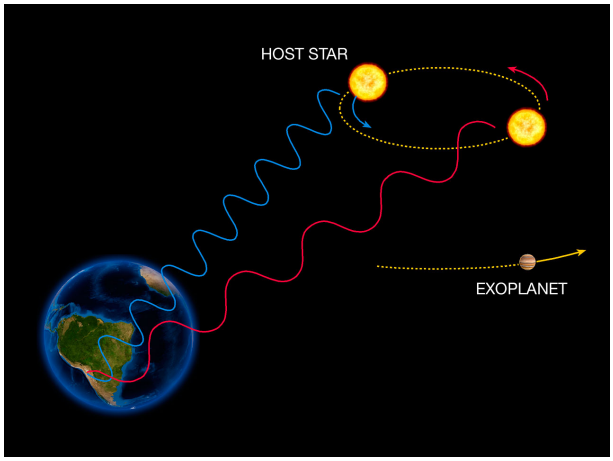


Figure A.1: Image depicting the Doppler effect caused by the stellar motion. Credits to ESO.

As can be easily understood by analyzing Eq. A.2, the radial velocity method suffers from several observation biases:

- $K \sim M_p P^{-1/3}$: it is easier to detect massive planets with short orbital periods (such as Pegasi 51 b);
- $K \sim M_\star^{-2/3}$: it is easier to detect planets orbiting low-mass stars, such as M dwarfs. However, low-mass stars are fainter, so it is more difficult to observe them with the required signal-to-noise ratio;
- $K \sim (1 - e^2)^{-1/2}$: it is easier to observe planets with high eccentricity. However, because of the particular shape of the radial velocity curve in the presence of highly eccentric planets, it is possible to miss them if we have poor sampling;
- $K \sim \sin(i)$: it is easier to detect planets with orbits coplanar with the line of sight.

The last point in the list tells us something very important about the radial velocity method: it suffers from an intrinsic degeneracy with the orbital inclination. In fact, with the radial velocity method alone it is not possible to derive the orbital inclination, meaning that we can measure only the minimum mass of the planet $M_p \sin(i)$.

As a matter of fact, through the radial velocity technique we can derive the following parameters:

- the orbital period P;
- the orientation of the periastron $\omega$;
- the orbital eccentricity e;
- the semimajor axis by using Kepler's law;
- the minimum mass $M_p \sin(i)$.

If we want to measure the true planetary mass, we need also the orbital inclination. This is possible when the radial velocity method is applied in combination with the transit method.

## A.2 The transit method

The transit detection method, at a conceptual level, is perhaps the most simple exoplanet detection technique. When an exoplanet transits across the stellar disk of its host star, the stellar flux is reduced. This is a purely geometrical phenomenon, so that the reduction in

stellar flux can be easily computed, as a first approximation, as the ratio of the squared radii of the planet and of the star:

$$\Delta F = \frac{R_p^2}{R_\star^2} \tag{A.3}$$

In a similar fashion, we can have occultations: when the planet is behind the star, we observe only the stellar flux, not the combined fluxes coming from the star and the planet. This produces a small reduction in the observed flux.

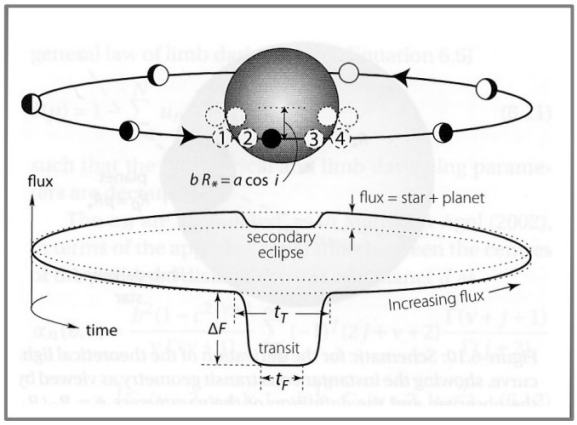


Figure A.2: Image depicting a schematics of transits and occulations. The image is taken from Perryman (2011).

It is easy to see that this method favours the discovery of large exoplanets orbiting small stars. Transits and occultations are characterized by particular shapes on the stellar light curve. The shape of the transit in the light curve depends on several stellar, planetary and orbital parameters and on the geometric configuration of the transit. Transit parameters, such as epoch, period, transit duration, impact parameter $b \approx a\cos(i)/R_\star$, radii ratio and limb darkening coefficients (quantities that describe the fact that the surface brightness of a star is not uniform, resulting in a decrease in intensity towards the edges of the star) are obtained by fitting a model of the light curve to the observed light curve.

The first exoplanetary transit ever observed was performed in 1999 by Charbonneau et al. (2000). One might think that it took quite a long time to observe an exoplanet with this method for the first time. The fact is that, despite its apparent theoretical simplicity, the transit method is faced by several observational and instrumental challenges. The first one is that it requires very stringent geometrical configurations to be performed. A transit can be observed only in a nearly edge-on orbit, such that $a_p\cos(i) \leqslant R_\star + R_p$. It is possible to derive that the probability of a transit is $P_{transit} \approx R_\star/a_p$. In fact, exoplanets are detectable with the transit method only when they have orbital inclinations that are

different from $i = 90°$ only by a few degrees. Furthermore, because of the transit probability, it is easier to find exoplanets in small orbits around large stars. Another challenge when trying to detect exoplanets by searching for their transits is that the magnitude of the effect is rather small. To give some numbers, Earth would produce a flux reduction of the order of $8 \times 10^{-5}$ and the probability to observe such transit would be $\approx 0.0047$. This means that, if every star had an Earth-like planet, we would need to observe about 200 stars to find such planet. Jupiter would produce a reduction in flux of order 0.01, but the probability of observing its transit would be $\approx 0.0009$. If every star had a Jupiter-like planet, we would need to observe 1 100 stars to find one. Another important consideration that we must take into account is that short-period planets are favoured not only because of the transit probability, but also because they transit more frequently. These three aspects tell us three facts:

- we need large surveys in order to deal with the low transit probability;
- we need long term continuous monitoring in order to not miss transit events;
- we need high photometric accuracy in order to deal with the small transit signal.

For these reasons space surveys are the way forward for transit searches: they allow to observe tens if not hundreds of thousands of stars with a photometric accuracy high enough to detect Super-Earths and Earth-sized planets. From ground, because of the limitations imposed by the atmosphere, it is virtually impossible to reach a photometric accuracy good enough to detect planets smaller than gas giants.

Given that the transit method in now a very well established and fruitful detection method, yielding the discovery of most of the currently known exoplanets, the greatest challenge that this technique currently faces is the false-positives problem. There are several astrophysical phenomena that may mimick a transit signal. The most vexing one comes from background eclipsing binaries. An eclipsing binary lurking in background of a star may indeed induce a signal in the stellar light curve which closely resembles that of an exoplanet and whose identification can be pretty difficult. It follows quite naturally that the transit method alone is not enough to confirm the presence of an exoplanet. An exoplanet can be safely confirmed once it has been detected using both the transit method and the radial velocity method. Since space surveys have identified many thousands of candidate exoplanets, it is clear that not all of them can be observed spectroscopically. For this reason, statistical validation has become a common practice. It consists in demonstrating that all possible astrophysical false-positive scenarios are statistically unlikely to have generated a transit signal for a given candidate exoplanet. Now, it must be stated clearly that statistical validation is not confirmation. Proper confirmation comes only from the combination of the transit method and the radial velocity method.

The combination of the radial velocity method and the transit method opens up a fascinating possibility. We know that from radial velocity observations we are able to retrieve the minimum mass of the planetary object, while from the transit signal we can retrieve the radius of the planet as well as its orbital inclination, which must be close to 90° for the planet to be observable in the first place. Knowing the orbital inclination, we can resolve the degeneracy in the minimum mass $M_p \sin(i)$, obtaining the true planetary mass. Now, having both the planetary mass and the planetary radius, it is very straight-forward to estimate the planetary mean density. This is an extremely important parameter, necessary for a first characterization of the exoplanet. One of the key goals of the PLATO mission is indeed the characterization of the mean density of the exoplanets it will discover. This will be done by combining the transit observations from space with successive radial velocity follow-ups from ground-based observatories.

# Appendix B

# Measuring astronomical distances: the trigonometric parallax method

In this appendix we explain the trigonometric parallax method, a technique used to estimate distances of celestial objects within our Galaxy. It follows naturally that it is a method of fundamental importance in the context of astrometric missions, such as Gaia. The physical principle behind this technique is extremely simple and purely geometrical: if we observe an object from two different vantage points, given that we know the distance between the two points and the angular shift, called "parallax", it is easy to extract the distance of the object from trigonometric relations.

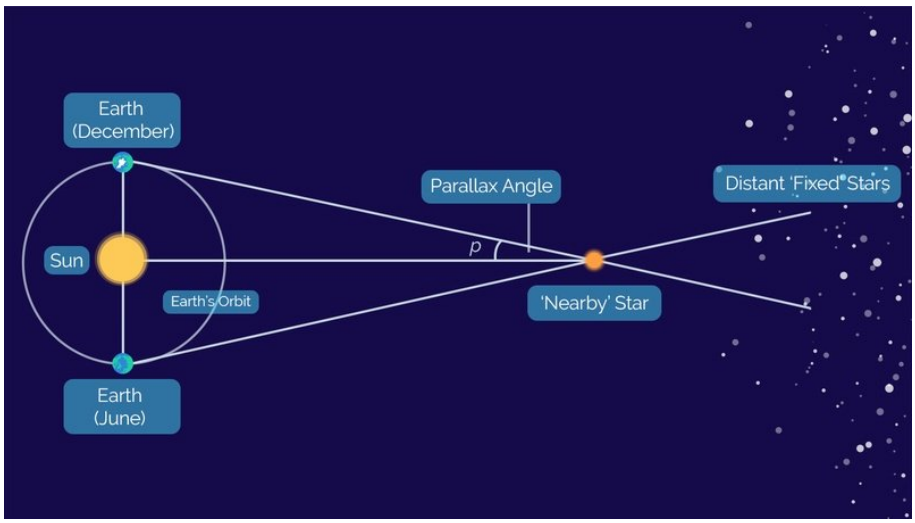


Figure B.1: Image depicting a schematics of the stellar parallax principle. Credits to Alice Hopkinson, LCO.

This simple principle can be applied to measure the distance of nearby stars. It

requires a long baseline, since the celestial objects need to observed with a temporal distance of six months, in order to have a base of the triangle (the Earth-Sun distance) long enough to be able to measure the distances of stars. In fact, the angle subtended by the star is very small: if we took a shorter base of the triangle, such as the Earth's diameter, we would not be able to measure the small angle. The apparent position of the star is measured with respect to a distant background, which is basically unaffected by the parallax due to its enormous distance. The parallax angle is one half of the total angular shift of the star in one year. Parallaxes are measured in arcseconds. The parsec, the fundamental measurement unit for astronomical distances, is defined as the distance of a star that has an annual parallax of 1 arcsec. 1 parsec corresponds to about 3.26 light-years.

It is possible to find a very simple formula that relates the parallax angle and the distance of the celestial object:

$$d \approx \frac{1}{p} \tag{B.1}$$

where d is the distance of the object measure in parsecs and p is the stellar parallax measured in arcseconds.

Now, it is evident that increasing the distance of the object reduces the corresponding parallax. This means that this method is capable of measuring the distances only of nearby objects. Gaia is able to measure the distances of objects at distances at the level of 10 kpc with an accuracy of 20%.

# Appendix C

# Computing the uncertainties on V and T

In this appendix I show the computation of the uncertainties on $V_{LSR}$ and $T_{LSR} = \sqrt{U_{LSR}^2 + W_{LSR}^2}$.

As it is widely known, given a function $F = F(x_1,\ x_2,\ ...,\ x_n)$ of n measurements $x_1 \pm \sigma_1$, $x_2 \pm \sigma_2$, ..., $x_n \pm \sigma_n$, the formula that describes uncertainty propagation is:

$$\sigma_F = \sum_{i=1}^{n} \left( \frac{\partial F}{\partial x_i} \sigma_i \right)^2 \tag{C.1}$$

where $\sigma_F$ is the uncertainty on F.

By expanding Eq. 5.4 I find that:

$$
\begin{cases}
U = -\sin(\alpha)\left(1-\dfrac{V_R}{c}\right)^{-1}\mu_{\alpha*}\dfrac{A_V}{\pi}+ \\
-\sin(\delta)\cos(\alpha)\left(1-\dfrac{V_R}{c}\right)^{-1}\mu_{\delta}\dfrac{A_V}{\pi}+ \\
+\ \cos(\delta)\cos(\alpha)\left(1-\dfrac{V_R}{c}\right)^{-1}V_R \\
V = \cos(\alpha)\left(1-\dfrac{V_R}{c}\right)^{-1}\mu_{\alpha*}\dfrac{A_V}{\pi}+ \\
-\sin(\delta)\sin(\alpha)\left(1-\dfrac{V_R}{c}\right)^{-1}\mu_{\delta}\dfrac{A_V}{\pi}+ \\
+\cos(\delta)\sin(\alpha)\left(1-\dfrac{V_R}{c}\right)^{-1}V_R \\
W = \cos(\delta)\left(1-\dfrac{V_R}{c}\right)^{-1}\mu_{\delta}\dfrac{A_V}{\pi}+ \\
+\sin(\delta)\left(1-\dfrac{V_R}{c}\right)^{-1}V_R
\end{cases}
\tag{C.2}
$$

I can apply Eq. C.1 to the three equations in Eq. C.2.

Let me start with the U component. I have that the partial derivatives of U with respect to the parameters it depends on are:

$$
\begin{cases}
\dfrac{\partial U}{\partial \alpha} = -\cos(\alpha)\left(1-\dfrac{V_R}{c}\right)^{-1}\mu_{\alpha *}\dfrac{A_V}{\pi}+ \\
+\sin(\delta)\sin(\alpha)\left(1-\dfrac{V_R}{c}\right)^{-1}\mu_{\delta}\dfrac{A_V}{\pi}+ \\
-\ \cos(\delta)\sin(\alpha)\left(1-\dfrac{V_R}{c}\right)^{-1}V_R \\
\dfrac{\partial U}{\partial V_R} = -\sin(\alpha)\dfrac{c}{(c-V_R)^2}\mu_{\alpha *}\dfrac{A_V}{\pi}+ \\
-\sin(\delta)\cos(\alpha)\dfrac{c}{(c-V_R)^2}\mu_{\delta}\dfrac{A_V}{\pi}+ \\
+\cos(\delta)\cos(\alpha)\dfrac{c^2}{(c-V_R)^2} \\
\dfrac{\partial U}{\partial \mu_{\alpha}} = -\sin(\alpha)\left(1-\dfrac{V_R}{c}\right)^{-1}\cos(\delta)\dfrac{A_V}{\pi} \\
\dfrac{\partial U}{\partial \pi} = \sin(\alpha)\left(1-\dfrac{V_R}{c}\right)^{-1}\mu_{\alpha *}\dfrac{A_V}{\pi^2}+ \\
+\sin(\delta)\cos(\alpha)\left(1-\dfrac{V_R}{c}\right)^{-1}\mu_{\delta}\dfrac{A_V}{\pi^2} \\
\dfrac{\partial U}{\partial \delta} = \sin(\alpha)\sin(\delta)\left(1-\dfrac{V_R}{c}\right)^{-1}\mu_{\alpha}\dfrac{A_V}{\pi}+ \\
-\cos(\delta)\cos(\alpha)\left(1-\dfrac{V_R}{c}\right)^{-1}\mu_{\delta}\dfrac{A_V}{\pi}+ \\
-\ \sin(\delta)\cos(\alpha)\left(1-\dfrac{V_R}{c}\right)^{-1}V_R \\
\dfrac{\partial U}{\partial \mu_{\delta}} = -\sin(\delta)\cos(\alpha)\left(1-\dfrac{V_R}{c}\right)^{-1}\dfrac{A_V}{\pi}
\end{cases}
\tag{C.3}
$$

Once I have the partial derivatives, it is easy to compute the uncertainty on U:

$$
\begin{aligned}
\sigma_U^2 = \sum_{i=1}^{n}\left(\frac{\partial U}{\partial x_i}\sigma_i\right)^2 = &\left(\frac{\partial U}{\partial \alpha}\sigma_{\alpha}\right)^2 + \left(\frac{\partial U}{\partial V_R}\sigma_{V_R}\right)^2 + \left(\frac{\partial U}{\partial \mu_{\alpha}}\sigma_{\mu_{\alpha}}\right)^2 + \\
&+ \left(\frac{\partial U}{\partial \pi}\sigma_{\pi}\right)^2 + \left(\frac{\partial U}{\partial \delta}\sigma_{\delta}\right)^2 + \left(\frac{\partial U}{\partial \mu_{\delta}}\sigma_{\mu_{\delta}}\right)^2
\end{aligned}
\tag{C.4}
$$

Regarding the V component, the partial derivatives are:

$$
\begin{cases}
\dfrac{\partial V}{\partial \alpha} = -\sin(\alpha)\left(1-\dfrac{V_R}{c}\right)^{-1}\mu_{\alpha*}\dfrac{A_V}{\pi}+ \\
-\sin(\delta)\cos(\alpha)\left(1-\dfrac{V_R}{c}\right)^{-1}\mu_{\delta}\dfrac{A_V}{\pi}+ \\
+\cos(\delta)\cos(\alpha)\left(1-\dfrac{V_R}{c}\right)^{-1}V_R \\
\dfrac{\partial V}{\partial V_R} = \cos(\alpha)\dfrac{c}{(c-V_R)^2}\mu_{\alpha*}\dfrac{A_V}{\pi}+ \\
-\sin(\delta)\sin(\alpha)\dfrac{c}{(c-V_R)^2}\mu_{\delta}\dfrac{A_V}{\pi}+ \\
+\cos(\delta)\sin(\alpha)\dfrac{c^2}{(c-V_R)^2} \\
\dfrac{\partial V}{\partial \mu_\alpha} = \cos(\alpha)\left(1-\dfrac{V_R}{c}\right)^{-1}\cos(\delta)\dfrac{A_V}{\pi} \\
\dfrac{\partial V}{\partial \pi} = -\cos(\alpha)\left(1-\dfrac{V_R}{c}\right)^{-1}\mu_{\alpha*}\dfrac{A_V}{\pi^2}+ \\
+\sin(\delta)\sin(\alpha)\left(1-\dfrac{V_R}{c}\right)^{-1}\mu_{\delta}\dfrac{A_V}{\pi^2} \\
\dfrac{\partial V}{\partial \delta} = -\cos(\alpha)\sin(\delta)\left(1-\dfrac{V_R}{c}\right)^{-1}\mu_{\alpha}\dfrac{A_V}{\pi}+ \\
-\cos(\delta)\sin(\alpha)\left(1-\dfrac{V_R}{c}\right)^{-1}\mu_{\delta}\dfrac{A_V}{\pi}+ \\
-\sin(\delta)\sin(\alpha)\left(1-\dfrac{V_R}{c}\right)^{-1}V_R \\
\dfrac{\partial V}{\partial \mu_\delta} = -\sin(\delta)\sin(\alpha)\left(1-\dfrac{V_R}{c}\right)^{-1}\dfrac{A_V}{\pi}
\end{cases}
\tag{C.5}
$$

The uncertainty on V is:

$$
\begin{aligned}
\sigma_V^2 = \sum_{i=1}^{n}\left(\frac{\partial V}{\partial x_i}\sigma_i\right)^2 = &\left(\frac{\partial V}{\partial \alpha}\sigma_\alpha\right)^2 + \left(\frac{\partial V}{\partial V_R}\sigma_{V_R}\right)^2 + \left(\frac{\partial V}{\partial \mu_\alpha}\sigma_{\mu_\alpha}\right)^2 + \\
&+ \left(\frac{\partial V}{\partial \pi}\sigma_\pi\right)^2 + \left(\frac{\partial V}{\partial \delta}\sigma_\delta\right)^2 + \left(\frac{\partial V}{\partial \mu_\delta}\sigma_{\mu_\delta}\right)^2
\end{aligned}
\tag{C.6}
$$

Finally, the partial derivatives for the W component are:

$$\begin{cases} \dfrac{\partial W}{\partial \delta} = -\sin(\delta)\left(1-\dfrac{V_R}{c}\right)^{-1}\mu_\delta\dfrac{A_V}{\pi}+ \\ +\cos(\delta)\left(1-\dfrac{V_R}{c}\right)^{-1}V_R \\ \dfrac{\partial W}{\partial V_R} = \cos(\delta)\dfrac{c}{(c-V_R)^2}\mu_\delta\dfrac{A_V}{\pi}+ \\ +\sin(\delta)\dfrac{c^2}{(c-V_R)^2} \\ \dfrac{\partial W}{\partial \mu_\delta} = \cos(\delta)\left(1-\dfrac{V_R}{c}\right)^{-1}\dfrac{A_V}{\pi} \\ \dfrac{\partial W}{\partial \pi} = -\cos(\delta)\left(1-\dfrac{V_R}{c}\right)^{-1}\mu_\delta\dfrac{A_V}{\pi^2} \end{cases} \tag{C.7}$$

The total uncertainty on W is then:

$$\sigma_W^2 = \sum_{i=1}^{n}\left(\frac{\partial W}{\partial x_i}\sigma_i\right)^2 = \left(\frac{\partial W}{\partial \delta}\sigma_\delta\right)^2 + \left(\frac{\partial W}{\partial V_R}\sigma_{V_R}\right)^2 + \left(\frac{\partial W}{\partial \pi}\sigma_\pi\right)^2 + \\ + \left(\frac{\partial W}{\partial \mu_\delta}\sigma_{\mu_\delta}\right)^2 \tag{C.8}$$

To obtain the velocities in Galactic coordinates, it is necessary to

pre-multiplicate them by the matrix $A'_G$ shown in Eq. 5.6. For the sake of a simpler notation, I write such matrix as:

$$A'_G = \begin{pmatrix} A & B & C \\ D & E & F \\ G & H & I \end{pmatrix} \tag{C.9}$$

where A, B, ..., I are numerical values.

I can easily find that:

$$\begin{pmatrix} U_G \\ V_G \\ W_G \end{pmatrix} = \begin{pmatrix} AU+BV+CW \\ DU+EV+FW \\ GU+HV+IW \end{pmatrix} \tag{C.10}$$

Let me consider the first row of the matrix. The partial derivatives of $U_G$ with respect to U,V and W are:

$$\begin{cases} \dfrac{\partial U_G}{\partial U} = A \\ \dfrac{\partial U_G}{\partial V} = B \\ \dfrac{\partial U_G}{\partial W} = C \end{cases} \tag{C.11}$$

The total uncertainty on $U_G$ is:

$$\begin{aligned} \sigma^2_{U_G} &= \left(\frac{\partial U_G}{\partial U}\sigma_U\right)^2 + \left(\frac{\partial U_G}{\partial V}\sigma_V\right)^2 + \left(\frac{\partial U_G}{\partial W}\sigma_W\right)^2 \\ &= (A\sigma_U)^2 + (B\sigma_V)^2 + (C\sigma_W)^2 \end{aligned} \tag{C.12}$$

In a similar fashion, the uncertainties on the other two components in Galactic coordinates are:

$$\sigma^2_{V_G} = (D\sigma_U)^2 + (E\sigma_V)^2 + (F\sigma_W)^2 \tag{C.13}$$

and

$$\sigma^2_{W_G} = (G\sigma_U)^2 + (H\sigma_V)^2 + (I\sigma_W)^2 \tag{C.14}$$

Successively, I corrected for the solar motion in the LSR, as explained in Subsection 5.1.2. Considering $U_G$ as an example, we obtained:

$$U_{LSR} = U_G - U_\odot \tag{C.15}$$

The corresponding partial derivatives are:

$$\begin{cases} \dfrac{\partial U_{LSR}}{\partial U_G} = 1 \\ \dfrac{\partial U_{LSR}}{\partial V} = -1 \end{cases} \tag{C.16}$$

The total uncertainty on $U_{LSR}$ is then:

$$\sigma_{U_{LSR}} = \sqrt{\sigma^2_{U_G} + \sigma^2_{U_\odot}} \tag{C.17}$$

Similarly, for the other components I have:

$$\sigma_{V_{LSR}} = \sqrt{\sigma^2_{V_G} + \sigma^2_{V_\odot}} \tag{C.18}$$

and

$$\sigma_{W_{LSR}} = \sqrt{\sigma^2_{W_G} + \sigma^2_{W_\odot}} \tag{C.19}$$

Finally, I need to compute the uncertainty on the Toomre component: $T_{LSR} = \sqrt{U_{LSR}^2 + W_{LSR}^2}$. Let us compute the partial derivatives with respect to $U_{LSR}$ and $W_{LSR}$:

$$\begin{cases} \dfrac{\partial T_{LSR}}{\partial U_{LSR}} &= \dfrac{U_{LSR}}{\sqrt{U_{LSR}^2 + W_{LSR}^2}} \\ \dfrac{\partial T_{LSR}}{\partial W_{LSR}} &= \dfrac{W_{LSR}}{\sqrt{U_{LSR}^2 + W_{LSR}^2}} \end{cases} \tag{C.20}$$

The total uncertainty on $T_{LSR}$ is then:

$$\sigma_{T_{LSR}} = \sqrt{\left(\frac{U_{LSR}\sigma_{U_{LSR}}}{\sqrt{U_{LSR}^2 + W_{LSR}^2}}\right)^2 + \left(\frac{W_{LSR}\sigma_{W_{LSR}}}{\sqrt{U_{LSR}^2 + W_{LSR}^2}}\right)^2} \tag{C.21}$$

$\sigma_{V_{LSR}}$ and $\sigma_{T_{LSR}}$ define the errorbars on the Toomre diagrams shown in Section 5.3.

# Bibliography


[1] Abdurro'uf et al. "The Seventeenth Data Release of the Sloan Digital Sky Surveys: Complete Release of MaNGA, MaStar, and APOGEE-2 Data". In: 259.2, 35 (Apr. 2022), p. 35. DOI: 10.3847/1538-4365/ac4414. arXiv: 2112.02026 [astro-ph.GA].

[2] Taft E. Armandroff. "The Properties of the Disk System of Globular Clusters". In: 97 (Feb. 1989), p. 375. DOI: 10.1086/114988.

[3] Annie Baglin et al. "CoRoT: Description of the Mission and Early Results". In: *Transiting Planets*. Ed. by Frédéric Pont, Dimitar Sasselov, and Matthew J. Holman. Vol. 253. IAU Symposium. Feb. 2009, pp. 71–81. DOI: 10.1017/S1743921308026252.

[4] T. Bensby, S. Feltzing, and I. Lundström. "Elemental abundance trends in the Galactic thin and thick disks as traced by nearby F and G dwarf stars". In: 410 (Nov. 2003), pp. 527–551. DOI: 10.1051/0004-6361:20031213.

[5] T. Bensby, S. Feltzing, and M. S. Oey. "Exploring the Milky Way stellar disk. A detailed elemental abundance study of 714 F and G dwarf stars in the solar neighbourhood". In: 562, A71 (Feb. 2014), A71. DOI: 10.1051/0004-6361/201322631. arXiv: 1309.2631 [astro-ph.GA].

[6] Paolo Bianchini and Alessandra Mastrobuono-Battisti. "A cautionary lesson from Gaia systematics: the mono-metallic globular cluster NGC 5904". In: 527.1 (Jan. 2024), pp. L32–L36. DOI: 10.1093/mnrasl/slad140. arXiv: 2307.15431 [astro-ph.GA].

[7] J. Binney and M. Merrifield. *Galactic Astronomy*. Princeton Series in Astrophysics. Princeton University Press, 1998. ISBN: 9780691025650. URL: https://books.google.it/books?id=arYYRoYjKacC.

[8] Christopher Boettner, Akshara Viswanathan, and Pratika Dayal. "Exoplanets Across Galactic Stellar Populations with PLATO: Estimating Exoplanet Yields Around FGK Stars for the Thin Disk, Thick Disk and Stellar Halo". In: *arXiv e-prints*, arXiv:2407.15917 (July 2024), arXiv:2407.15917. DOI: 10.48550/arXiv.2407.15917. arXiv: 2407.15917 [astro-ph.EP].

[9] William J. Borucki et al. “Kepler Planet-Detection Mission: Introduction and First Results”. In: *Science* 327.5968 (Feb. 2010), p. 977. DOI: 10.1126/science.1185402.

[10] Sven Buder et al. “The GALAH+ survey: Third data release”. In: 506.1 (Sept. 2021), pp. 150–201. DOI: 10.1093/mnras/stab1242. arXiv: 2011.02505 [astro-ph.GA].

[11] David Charbonneau et al. “Detection of Planetary Transits Across a Sun-like Star”. In: 529.1 (Jan. 2000), pp. L45–L48. DOI: 10.1086/312457. arXiv: astro-ph/9911436 [astro-ph].

[12] Alain Corso et al. “Rad-hard properties of the optical glass adopted for the PLATO space telescope refractive components”. In: *Optics Express* 26 (Dec. 2018), p. 33841. DOI: 10.1364/OE.26.033841.

[13] Sarah E. Dodson-Robinson et al. “A Spitzer Infrared Spectrograph Study of Debris Disks Around Planet-host Stars”. In: 141.1, 11 (Jan. 2011), p. 11. DOI: 10.1088/0004-6256/141/1/11. arXiv: 1010.3292 [astro-ph.SR].

[14] 1997 Esa. *VizieR Online Data Catalog: The Hipparcos and Tycho Catalogues (ESA 1997)*. VizieR On-line Data Catalog: I/239. Originally published in: 1997HIP...C.....0E. Feb. 1997.

[15] Gaia Collaboration et al. “The Gaia mission”. In: 595, A1 (Nov. 2016), A1. DOI: 10.1051/0004-6361/201629272. arXiv: 1609.04153 [astro-ph.IM].

[16] Panagiotis Gavras et al. “Gaia Data Release 3. Cross-match of Gaia sources with variable objects from the literature”. In: 674, A22 (June 2023), A22. DOI: 10.1051/0004-6361/202244367. arXiv: 2207.01946 [astro-ph.IM].

[17] G. Gilmore and N. Reid. “New light on faint stars - III. Galactic structure towards the South Pole and the Galactic thick disc.” In: 202 (Mar. 1983), pp. 1025–1047. DOI: 10.1093/mnras/202.4.1025.

[18] Amina Helmi et al. “The merger that led to the formation of the Milky Way’s inner stellar halo and thick disk”. In: 563.7729 (Oct. 2018), pp. 85–88. DOI: 10.1038/s41586-018-0625-x. arXiv: 1806.06038 [astro-ph.GA].

[19] Emily L. Hunt and Sabine Reffert. “Improving the open cluster census. II. An all-sky cluster catalogue with Gaia DR3”. In: 673, A114 (May 2023), A114. DOI: 10.1051/0004-6361/202346285. arXiv: 2303.13424 [astro-ph.GA].

[20] R. Lallement et al. “Three-dimensional maps of interstellar dust in the Local Arm: using Gaia, 2MASS, and APOGEE-DR14”. In: 616, A132 (Aug. 2018), A132. DOI: 10.1051/0004-6361/201832832. arXiv: 1804.06060 [astro-ph.GA].

[21] Diego Lorenzo-Oliveira et al. “The Solar Twin Planet Search. The age-chromospheric activity relation”. In: 619, A73 (Nov. 2018), A73. DOI: 10.1051/0004-6361/201629294. arXiv: 1806.08014 [astro-ph.SR].

[22] Michel Mayor and Didier Queloz. “A Jupiter-mass companion to a solar-type star”. In: 378.6555 (Nov. 1995), pp. 355–359. DOI: 10.1038/378355a0.

[23] M. Montalto et al. “The all-sky PLATO input catalogue”. In: 653, A98 (Sept. 2021), A98. DOI: 10.1051/0004-6361/202140717. arXiv: 2108.13712 [astro-ph.EP].

[24] V. Nascimbeni et al. “The PLATO field selection process. I. Identification and content of the long-pointing fields”. In: 658, A31 (Feb. 2022), A31. DOI: 10.1051/0004-6361/202142256. arXiv: 2110.13924 [astro-ph.EP].

[25] M. A. C. Perryman et al. “GAIA: Composition, formation and evolution of the Galaxy”. In: 369 (Apr. 2001), pp. 339–363. DOI: 10.1051/0004-6361:20010085. arXiv: astro-ph/0101235 [astro-ph].

[26] Michael Perryman. *The Exoplanet Handbook*. 2011.

[27] Roberto Ragazzoni et al. “A one meter class eye for the PLAnetary Transit and Oscillation spacecraft”. In: *Acta Astronautica* 115 (May 2015). DOI: 10.1016/j.actaastro.2015.04.026.

[28] H. Rauer et al. “The PLATO 2.0 mission”. In: *Experimental Astronomy* 38.1-2 (Nov. 2014), pp. 249–330. DOI: 10.1007/s10686-014-9383-4. arXiv: 1310.0696 [astro-ph.EP].

[29] Heike Rauer et al. “The PLATO Mission”. In: *arXiv e-prints*, arXiv:2406.05447 (June 2024), arXiv:2406.05447. DOI: 10.48550/arXiv.2406.05447. arXiv: 2406.05447 [astro-ph.IM].

[30] George R. Ricker et al. “Transiting Exoplanet Survey Satellite (TESS)”. In: *Space Telescopes and Instrumentation 2014: Optical, Infrared, and Millimeter Wave*. Ed. by Jr. Oschmann Jacobus M. et al. Vol. 9143. Society of Photo-Optical Instrumentation Engineers (SPIE) Conference Series. Aug. 2014, 914320, p. 914320. DOI: 10.1117/12.2063489. arXiv: 1406.0151 [astro-ph.EP].

[31] Ralph Schönrich, James Binney, and Walter Dehnen. “Local kinematics and the local standard of rest”. In: 403.4 (Apr. 2010), pp. 1829–1833. DOI: 10.1111/j.1365-2966.2010.16253.x. arXiv: 0912.3693 [astro-ph.GA].

[32] Matthias Steinmetz et al. “The Sixth Data Release of the Radial Velocity Experiment (RAVE). I. Survey Description, Spectra, and Radial Velocities”. In: 160.2, 82 (Aug. 2020), p. 82. DOI: 10.3847/1538-3881/ab9ab9. arXiv: 2002.04377 [astro-ph.SR].

[33] Matthias Steinmetz et al. “The Sixth Data Release of the Radial Velocity Experiment (RAVE). II. Stellar Atmospheric Parameters, Chemical Abundances, and Distances”. In: 160.2, 83 (Aug. 2020), p. 83. DOI: 10.3847/1538-3881/ab9ab8. arXiv: 2002.04512 [astro-ph.SR].

[34] M. B. Taylor. “STILTS - A Package for Command-Line Processing of Tabular Data”. In: *Astronomical Data Analysis Software and Systems XV*. Ed. by C. Gabriel et al. Vol. 351. Astronomical Society of the Pacific Conference Series. July 2006, p. 666.

[35] M. B. Taylor. “TOPCAT & STIL: Starlink Table/VOTable Processing Software”. In: *Astronomical Data Analysis Software and Systems XIV*. Ed. by P. Shopbell, M. Britton, and R. Ebert. Vol. 347. Astronomical Society of the Pacific Conference Series. Dec. 2005, p. 29.

[36] *The Hipparcos mission. Pre-launch status. Volume I: The Hipparcos satellite.* Vol. 1. June 1989.

[37] Kim A. Venn et al. “Stellar Chemical Signatures and Hierarchical Galaxy Formation”. In: 128.3 (Sept. 2004), pp. 1177–1195. DOI: 10.1086/422734. arXiv: astro-ph/0406120 [astro-ph].

[38] C. L. Watson, A. A. Henden, and A. Price. “The International Variable Star Index (VSX)”. In: *Society for Astronomical Sciences Annual Symposium* 25 (May 2006), p. 47.

[39] M. Wenger et al. “The SIMBAD astronomical database. The CDS reference database for astronomical objects”. In: 143 (Apr. 2000), pp. 9–22. DOI: 10.1051/aas:2000332. arXiv: astro-ph/0002110 [astro-ph].